Department of Precision and Microsystems Engineering

Generation of quantum emitters in hBN via strain engineering for biosensing applications

Mireia Flores Cervelló

Report no	: 2023.045
Coach	: Xiliang Yang
Professor	: Dr. Sabina Caneva
Specialisation	: MNE-DMN
Type of report	: Master’s Thesis
Date	: 13 July 2023

Delft University of Technology

Challenge the future

DELFT UNIVERSITY OF TECHNOLOGY

HIGH TECH ENGINEERING THESIS

Generation of quantum emitters in hBN via strain engineering for biosensing applications

---

Authors:
Mireia Flores Cervelló

Supervisors:
Dr. S. Caneva
Xiliang Yang

in partial fulfilment of the requirements for the degree of

Master of Science
in Mechanical Engineering

to be defended publicly on Friday July 28, 2023 at 2:00 PM.

Abstract

This master thesis explores strain-induced quantum emitters in hexagonal boron nitride (hBN) as novel optical nanoprobes for Förster resonance energy transfer (FRET)-based biosensors. These types of emitters could outperform conventionally used fluorophores due to their high brightness, stability in harsh environments, biocompatibility and ease of integration with solid state devices. Ultimately, the aim is to combine optically-active hBN emitters with protein fingerprinting devices, which could impact the field of molecular diagnostics by detecting clinically relevant protein biomarkers.

To date, however, it is unclear which parameters are crucial for the generation of hBN quantum emitters with strain in both CVD grown and exfoliated hBN crystals. To address this gap in the field, this thesis systematically investigates the generation of strain by mechanically exfoliating pristine hBN crystals onto a variety of rigid micro/nanostructures with different aspect ratios, including 5 μm and 10μm microbeads, femtosecond laser-ablated cavities, and CD/Blu-ray micro-nanostructures. We characterised the samples with fluorescence microscopy and atomic force microscopy in order to correlate the optical properties of the hBN with the topography of the substrate. Among the tested structures, samples displayed clear fluorescent emission at the location where the hBN was deposited on the femtosecond laser-ablated cavities with sharp edges. The presence of strain in these regions was verified with Raman spectroscopy, and the spectral properties of the fluorescent regions were determined with photoluminescence spectroscopy. We additionally studied the temporal behavior of the identified emitters and observed effects such as blinking with intensities reduced up to 38% and photobleaching with quantum emitters lifetimes between 6.57 s and 44.17 s.

While there were no clear threshold values of curvature, substrate structure height, and thickness of hBN that led to reproducible localized fluorescence, these findings open up further research opportunities for the use of strain engineering to generate quantum emitters in hBN.

Contents

1 Introduction

The use of technologies such as QR code readers or facial recognition has become essential in our current society [1]. These systems have the ability to identify individuals and the things surrounding them in a matter of seconds. When the size of these objects is reduced to the nanoscale, however, their detection and identification becomes a challenge. This is the case of biomolecules such as proteins, which are chains of amino acids that play an essential role in the functioning of all living organisms [2]. The detection and identification of these biomolecules, such as certain cancerous trace bio-markers or disease-specific proteins are crucial for an accurate and personalised diagnosis and treatment monitoring [3].

At present, mass spectrometry and Edman degradation are the main techniques employed to identify proteins. Protein mass spectrometry involves several steps. The proteins are first broken down into smaller fragments called peptides [4]. These peptides are then separated, fragmented and ionised and captured by mass spectrometers. Finally, computational methods are used to identify the captured mass spectra and identify the proteins. On the other hand, Edman degradation is a chemical process that is carried out in several steps to remove amino acids from the N-terminal end of a peptide or protein [5]. This sequential removal allows for the determination of the amino acid sequence after analysing these amino acids with liquid chromatography or mass spectrometry.

Even if in the recent decades mass spectrometers have become very sophisticated, and therefore have been able to provide more detailed information about these molecules, they are still unable to identify many rare proteins [6]. Furthermore, they are expensive and have a limited dynamic range which makes the detection of proteins that are present at a low copy rate difficult. Finally, some amino acids have a similar mass and charge, which leads to false discovery rates and as a result, the misidentification of proteins [7][8]. Edman degradation also has several limitations: it is very time consuming, unable to process large proteins and complex proteins. Therefore, the realisation of a technique with high sensitivity and high throughput that can analyse biological matter down to the molecular scale still remains a challenge [8][9][10].

An alternative method that has the potential to recognize proteins accurately is fingerprinting. Fingerprinting can identify thousands of unique protein sequences, by only detecting a few types of amino acids out of the 20 possible in a reduced part of the protein [11]. With the use of fluorescence, specific types of amino acids are labelled with different dyes. Then, the sequence of the labelled amino acids is read and referenced against a database of known proteins. To read the fluorescent signals of these fluorescent amino acids, a biosensor that can reach nanometer spatial resolution is needed, which is where Förster resonance energy transfer (FRET) based biosensors excel [10] [12][13].

FRET-based biosensors typically use fluorescent molecules to detect shape changes at the molecular scale (Figure 1). When the labelled amino acids are sufficiently near to these fluorescent molecules, a non-radiative interaction occurs, in which the energy of the molecule is transferred to the amino acid label. Consequently, the signal of a specific amino acid is enhanced, and as a result it is known which amino acid is detected. The number and order of appearance of these detected amino acids forms the protein 'fingerprint'.

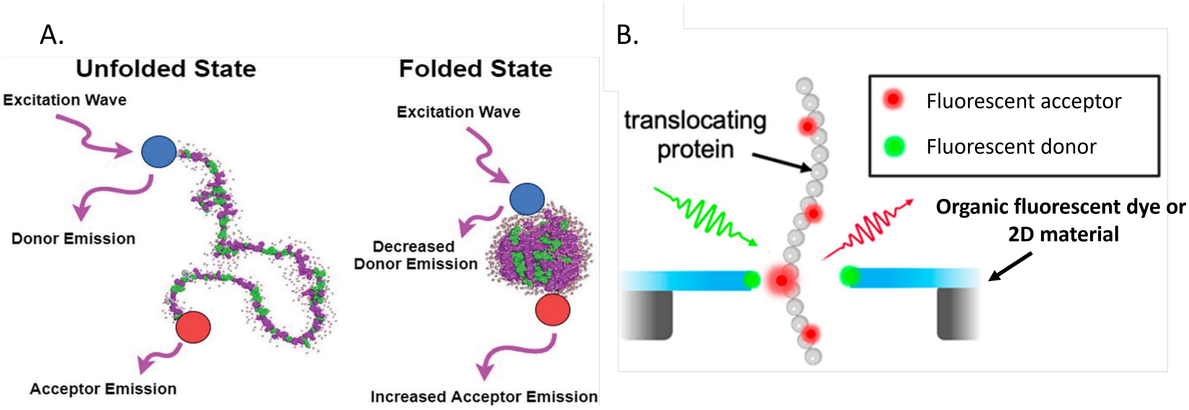

Figure 1: **A.** Conformational change of a protein measured by FRET. Unfolded state of the protein, in which the acceptor signal is not enhanced by the donor vs folded state of the protein, in which due to the proximity between donor and acceptor, the signal of the acceptor is enhanced [14]. **B.** Protein FRET fingerprinting. The protein is identified due to the detection of specific amino acids which are labelled with fluorescent dyes [15].

Clearly, the characteristics of the fluorescent molecules and the labels are key for a practical accomplishment of FRET-based applications [16]. Even though this technology is a promising tool to fingerprint proteins, the current characteristics of the traditional molecules limit their practical application [17]. These typically used molecules, such as organic fluorescent dyes and fluorescent proteins have some major drawbacks that include short fluorescence lifetime, low chemical stability and poor photostability [18].

Therefore, the motivation of this master thesis is to investigate an alternative to the traditional fluorescent molecules used in FRET-based biosensors, and hence outperform conventionally used fluorophores in protein fingerprinting. To achieve this, we will investigate novel types of material that have the ability to host fluorescent optical emitters i.e. two-dimensional (2D) materials [19]. These nanomaterials have proven to have excellent properties for biosensing, solving key problems that traditional emitters have [18]. For instance, 2D materials like hexagonal boron nitride (hBN) exhibit high chemical stability and photostability, good biocompatibility, and, due to its planar nature, can be easily integrated in nanodevices.

2 State-of-the-art

We now introduce the principle of fluorescence and the operation of a single-molecule FRET experiment. Next, an alternative to the conventional fluorophores is presented, focusing on 2D materials. Finally, the different methodologies to produce optical emitters in 2D materials are explained, together with how these emitters are influenced by various inherent and external factors.

2.1 Photoluminescence in nanomaterials

When a material's dimensions are reduced to a few nanometres, electrons within the material become confined in those dimensions. This confinement of electrons make the energy levels of these nanostructures discrete, whereas they are continuous in their bulk form. The quantization of electron energies affects the behaviour of the material, leading to changes in the optical, electrical and mechanical properties of the material [20].

One of the phenomena that can occur in nanomaterials due to the confinement of electrons are characteristic photoluminescence spectra. Photoluminescence is a process in which a luminescent material,for example a material with optically active defects or phosphor, is stimulated usually by visible light, and subsequently emits light of a different wavelength. [21]. The radiative process occurs in three steps: (1) A photon is absorbed, exciting an electron to a higher electronic state (E_1). (2) The electron relaxes to the band edge and (3) A photon is emitted when this electron returns to the ground state (E_0) [22]. The transition between these two electronic states E_0 and E_1 is explained by the Franck-Condon principle, which states that electronic transitions are very rapid compared to the nuclei. Therefore, the nuclei do not have a significant movement, and as a result, the absorption or emission of light occurs between electronic states that correspond to the atoms being in similar positions or having minimal changes in their positions [23]. Since vibrational states are the ones that require the least amount of change in nuclear motion, both absorption and emission lead to molecules that are in a vibrational excited state (Figure 2A).

The fact that in nanomaterials the energy levels are discrete, results in electrons being able to only absorb photons that have an energy equal to the difference between these two electronic states ± vibrational states. In a similar way, the electron can only emit photons with specific energy. Therefore, photoluminescence spectra are composed of an absorption and an emission (fluorescence) spectrum as seen in Figure 2B. In Figure 2A the emission arrow is shorter than the absorption one, meaning it is less energetic, and therefore the wavelength of the emitted photons is longer [23].

Some concepts that are relevant to mention are the zero phonon line (ZPL) and the photon sideband (PSB) (Figure Figure 2). The ZPL describes the most intense and narrow line in the emission spectrum. This corresponds to the transition in which the electron goes from the ground state $\nu'' = 0$ to the excited state $\nu' = 0$ [24]. This means that there is no interaction with phonons (units of vibrational energy). It is considered that the ZPL is the purest form of light emission since the light is not broadened or shifted by the presence of phonons. On the other hand, the phonon sideband (PSB) is a broadened line in the emission spectrum that represents the interaction of the excited electron with phonons. This involvement of phonons can shift the energy of the emission and broaden it.

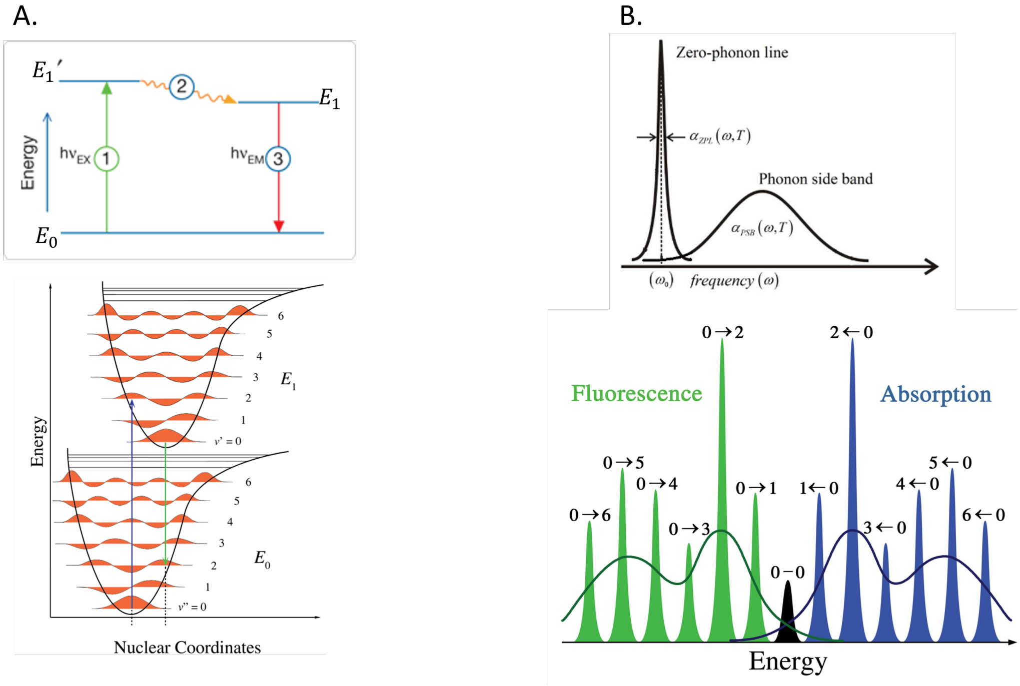

Figure 2: **A.** (Top) Simplified scheme showing the processes of optical absorption and subsequent emission of fluorescence [25]. (Bottom) The energy diagram of a confined electron is represented as a ground state E_0 and an excited state E_1 with discrete vibrational states (ν' and ν''). Between those states, absorption and emission occur. Figure adapted from [26]. **B.** (Top) Simplified scheme of the absorption spectrum of a single molecule showing its ZPL and its corresponding PSB.[27]. (Bottom) Absorption and emission spectrum corresponding to the energy diagram of Figure 2A. The phonon side band in the emission is represented in green, and in the absorption is represented in blue. These two go from $E_1, \nu' = 0$ to $E_0, \nu' > 0$ and from $E_0, \nu' = 0$ to $E_1, \nu' > 0$ respectively. The zero phonon line represented in black and is the transition from $\nu' = 0$ to $\nu'' = 0$ and viceversa [26].

It is also important to mention some of the phenomena that can occur in photoluminescence that are inconvenient in FRET applications, namely photoblinking and photobleaching. Photoblinking is defined as the temporary disappearance of fluorescence, while photobleaching is the permanent loss of fluorescence [28]. The second one can be caused by an external agent or a chemical reaction that changes the structure of the material.

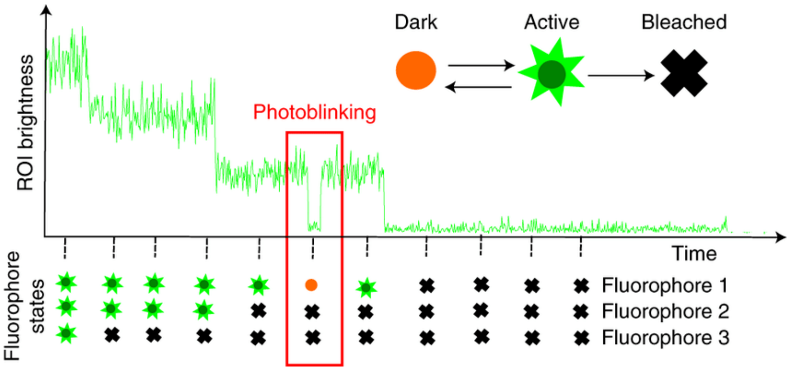

Figure 3: Schematics of photoblinking and photobleaching pehonmena. There are three fluorophores in the Region Of Interest (ROI). Each fluorophore transitions between active, dark and bleached states as indicated by the arrows. The brightness over time for a ROI reflects the states of all three fluorophores. It should be noted that only fluorophores in the active state emit photons [29].

Now that the basic working principles of photoluminescence in nanomaterials have been reviewed, in the following subsection the principles of Förster resonance energy transfer will be explained. With these two concepts, the physical phenomena that occur in FRET-based biosensors that use nanomaterials can be understood.

2.2 Introduction to FRET

Förster or fluorescence resonance energy transfer (FRET) is a photophysical pehomenon in which a fluorescent donor transfers energy to a nearby fluorescent acceptor that is initially in its ground state, through a non-radiative dipole-dipole coupling [30][16]. During this dipole-dipole interaction, the excited donor stimulates the acceptor to an excited state that enhances its luminescence, while the donor reduces its excited lifetime [17]. That means that if an acceptor is present, the donor instead of emitting photons, directly transfers its excited energy to the acceptor [19]. It should be noted that in order for FRET to happen, the emission wavelength of the donor must have some spectral overlap of excitation of the acceptor as seen in Figure 4 [31].

FRET is a near-field physical process, and occurs when the distance between the donor-acceptor pair is within $1-10\ nm$ [30]. FRET is extremely sensitive to this short distance range, and the efficiency of the energy transfer is highly affected when the distance between donor and acceptor changes. The efficiency of FRET is higher as the separation between donor and acceptor becomes shorter. Therefore FRET has the capacity to give us the needed nanoscale resolution to detect each amino acid accurately. This dependence can be seen in Figure 5. The the efficiency of the energy transfer is given by E_{FRET}, where R represents the distance between donor and acceptor and R_0 is the distance at which half of the energy is transferred.

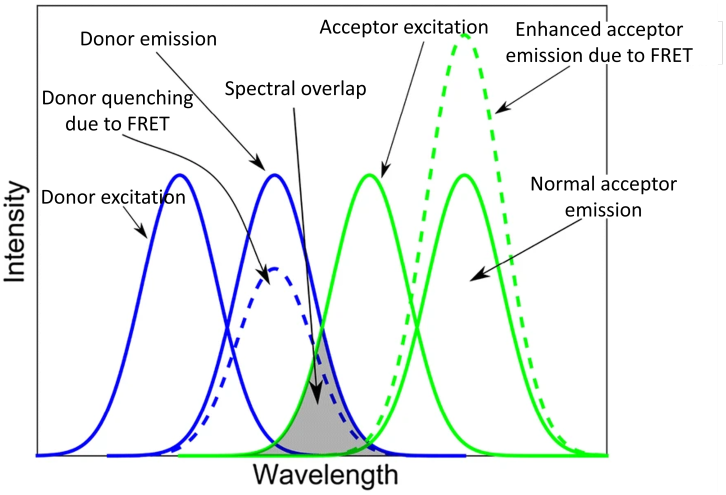

Figure 4: Spectral overlap between emission of the donor and excitation of the acceptor in order for FRET to occur. When FRET occurs, the fluorescence intensities of the donor and acceptor are reduced and enhanced respectively. Figure adapted from [31].

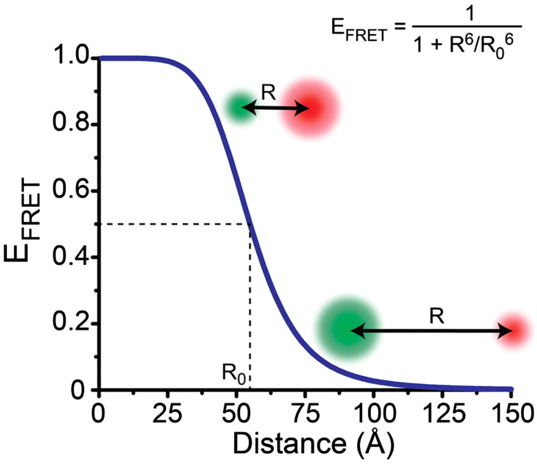

Figure 5: Energy efficiency of FRET process as a function of the separation between donor (green) and acceptor (red) [32].

Both donor and acceptor are typically fluorescent molecules such as fluorescent proteins or dyes, and their characteristics are essential to consider when designing and implementing a FRET experiment [16]. As mentioned in Section 1, these conventionally used molecules tend to have a poor photostability, low quantum efficiency or short fluorescent times, concepts that will be explained in subsection 2.3. These properties are key to making efficient FRET-based biosensors, leading researchers to consider alternatives. In the following section these alternatives are reviewed, including the state-of-the-art of photon sources in nanomaterials, as well as their challenges and prospects.

2.3 Quantum Emitters

Quantum emitters (QEs) generate photons after being optically or electronically excited during their fluorescence lifetime [33]. Apart from being photo-active, in our FRET application we also need QEs that meet additional strict requirements, namely:

1. **Controlled location of the quantum emitters**: As discussed in further sections, being able to control the location of the quantum emitters is challenging. However, it is a fundamental pre-requisite together with the scalability of these QEs to make of FRET an efficient and precise technology for the optical identification of proteins. Therefore, we need a scalable and deterministic process that can control the position and density of QE.

2. **Room temperature performance**: Proteins are very sensitive to temperature changes. They affected by thermal denaturation if they are exposed to temperatures outside the range of the ones from living organisms ($10°C - 60°C$) [34]. If denaturation occurs, proteins lose their structure, become unstable and can have the tendency to aggregate [35][34]. These effects are undesirable when the aim is to identify individual proteins with high accuracy. For this reason, quantum emitters that perform are room temperature are essential.

3. **Reproducibility**: It is important that all QEs that are chosen to be e.g. donors have the same optical properties such as the emission wavelength. This factor is crucial in order to avoid too much or too little spectral overlap between excitation and emission wavelengths of the donor and the acceptor [36].

4. **Photostability**: In order not to misidentify proteins and have a good biosensor performance, it is essential that the quantum emitters are stable in time [37]. Therefore, they should not blink or bleach during the measurement time.

5. **Brightness**: A high brightness, defined as the rate of photons that can be extracted from the system, is important in protein fingerprinting in order to emit a strong signal that can be detected by the EMCCD camera. One of the several factors that helps to quantify the brightness of a

quantum emitter is the quantum yield, defined as the ratio of the photons absorbed to the number of photons emitted [37].

It should be noted that there are other criteria to characterize QEs such as purity, a term which quantifies if only a single photon is emitted at a time or more. Even though this characteristic is more important in other applications such as quantum information, it will be mentioned in the following subsections with respect to specific materials.

As has been briefly mentioned in section 1, there are two types of traditional donor molecules: organic fluorescent dyes and fluorescent proteins. On the one hand, organic fluorescent dyes are a versatile type of donor due to their ease of emission tunability, their small size and low cost [18]. On the other hand, fluorescent proteins are very practical for in-vivo experiments. However, these two already well-known options present drawbacks that reduce the possible effectiveness of FRET-based biosensors. While organic dyes present a poor photobleaching resistance and a low chemical stability, fluorescent proteins possess a broad range of wavelength emission, producing different amounts of overlap with the acceptor [18][38]. Ultimately, these significantly limit the application of FRET-based biosensors.

Even if QEs in nanomaterials are promising candidates to improve the efficiency of the commonly used fluorophores, currently no photon source fulfills all the requirements of our fingerprinting application [37]. The current state-of-art on QEs, shows that the most investigated sources of quantized emission are in solid-state materials, such as quantum dots (QDs) and colour centers in diamond [37][39].

Quantum dots are semiconductor nanocrystals a few nanometres in size, and are characterized by quantum phenomena in their optical and electronic properties. Their dimension leads to confinement of valence and conduction electrons to a narrow spatial region, making their fluorescence emission easily tunable by changing the size of the QD and its composition [40]. Among the most studied QDs for bioimaging are the ones based on indium and cadmium [41]. Even though indium-based quantum dots like InGaAs or InAs are a reference for purity, they are toxic which discards their application for optical biosensors. The same holds true for cadmium based quantum dots.

On the other hand fluorescent point defects in diamond, also known as colour centers, have become an interesting alternative to traditional fluorophores since they are stable at room temperature [42]. At present, the most researched defects in diamond are the nitrogen-vacancy (NV) and the silicon-vacancy (SiV). The first, has a relatively low reproducibility and a quantum efficiency of 70 %. It is also sensitive to local electric fields, contributing to spectral broadening. In contrast, the silicon-vacancy has a high reproducibility, but an extremely low quantum efficiency (3.5 %) [43]. These are also expensive and complex to generate defects on them. However, point defects in diamond are better than quantum dots for biosensing because of their biocompatibility, since graphene quantum dots are usually made from graphene oxide. Graphene oxide presents a cell viability between a 5 % and a 60 %, and therefore a high toxicity [44][45]. Ultimately, the complication that these QEs present motivates the research of other nanomaterial systems [46].

A source of quantized emission that could be promising in the field of FRET biosensing, are defect states in two-dimensional (2D) materials [19]. Despite their novelty, QEs have already been studied in the insulating material hexagonal boron nitride (hBN), and also in semiconducting 2D materials like tungsten diselenide (WSe_2), molybdenum diselenide ($MoSe_2$) and tungsten disulfide (WS_2), also known as transition metal dichalcogenides [37]. Photostability, tunability, excellent optoelectrical properties and high integrability in devices are some of the promising characteristics that these newly emerging QEs possess [47].

In Table 1, traditional dyes are compared to the alternatives presented in the state-of-art in terms of parameters considered relevant for protein fingerprinting, namely quantum efficiency, photostability, reproducibility, biocompatibility and operation temperature. As can be seen, organic fluorescent dyes comply with most the majority of the requirements but, they are limited because of photobleaching and by their quantum efficiency especially in the infrared spectrum. Conversely, QDs and 2D materials possess a better photostability but 2D materials have a limited reproducibility due to more challenging integration of defects. Additionally depending on the material that hosts the QE, their quantum yield changes and it defines whether they are stable at cryogenic or at room temperatures.

Criteria	**Organic Fluorescent Dyes**	**Quantum Dots**	**2D Materials**
Quantum Efficiency	0.05-1.0	0.1-0.8	0.01 (TMDs) - 0.87 (hBN)
Photostability	Low Limited by photobleaching	Moderate Limited by blinking	High
Reproducibility	High	Medium-High	Limited
Biocompatibility	High	Low	TMDs: Low hBN: High
Temperature performance	RT	Cryogenic temperatures, RT	Cryogenic temperatures, RT

Table 1: Comparison of the performance of traditional FRET donors (Organic Fluorescent Dyes) and alternative donors (Quantum dots and 2D materials) [37][48][49][50][51][52][53]. RT stands for Room Temperature.

At this point we have discussed the most relevant properties of quantum emitters for single-molecule FRET measurement of proteins and the optical probe materials used (traditional dyes and the various alternatives that appear in the current state-of-art). The option that shows the most promising properties are 2D materials, specifically hBN, because they possess a high photostability and quantum efficiency, are biocompatible and can work at room temperature. The challenge of reproducibility is yet to be solved. In the following section, the state-of-the-art of optically-active 2D materials will be evaluated.

2.4 2D Materials and Hexagonal Boron Nitride

In section 1, 2D materials are mentioned to be a novel and promising type of materials for FRET based optical biosensors. These are atomically thin, layered materials that possess unique properties, compared to their bulk form [37] [54]. Materials like graphene, hexagonal boron nitride, transition metal dichalcogenides (TMDs) or transition metal oxides (TMOs) display rich optoelectronic properties and robust mechanical properties [55]. Due to the van der Waals bonding between layers, 2D materials are versatile to exfoliate, functionalize and integrate in planar devices, properties which ease their scalable implementation into complex systems (i.e. biosensors) compared to other alternatives material systems [46].

In subsection 2.3, the qualities of the different 2D materials will be analysed, in order to choose the most suitable option to form optical probes for single-molecule FRET (smFRET). In Table 2, the most relevant properties of QEs obtained in diamond and in various hosting 2D materials are summarized. This includes the stable operation temperature (T) of QEs and the reproducibility, which is represented by the range of wavelength emission. The Deybe-Waller factor (DWF) of the emitter represents in a scale from 0 to 1 the amount of photons emitted in the ZPL [56]. The brightness is expressed in units kilo counts per second. The lifetime is the time taken by an excited emitter to return to its ground state, setting the maximum extractable rate of the system [37]. If the lifetime of the donor is too short, the FRET efficiency will be significantly reduced since it may transfer energy to the acceptor before it is properly positioned to receive it. Equally, if the lifetime of the donor is too long, the process may be inefficient due to the limited time of the acceptor to absorb the energy.

Material	T(K)	Range of Wavelength Emission (nm)	Lifetime (ns)	Brightness (kcps)	DWF
NV	RT	630-750	12-22	100	0.03
hBN	RT up to 800K	570-750	1-3	7000	0.82 (at 77K)
WSe_2	<15	720-840	0.3-225	3000	0.6 (at 4K)
WS_2	Up to 10	610-680	1.4	10	-
$MoSe_2$	4	765-770	1	7	-

Table 2: Summary of the photophysical properties of solid-state QEs in NV [42][57][58][43] and 2D materials [52]. RT stands for room temperature.

As can be seen in Table 2, the semiconducting 2D materials (TMDs) work at cryogenic temperatures, and are therefore not suitable to sequence proteins compared to the stability at room temperatures of NV and hBN. Another difference is that both the insulating material and the diamond defect center have a wide emission wavelength range while in the transition metal dichalcogenides (TMDs), i.e. WSe_2, WS_2 and $MoSe_2$ have in general very narrow ranges, which would fulfill the reproducibility requirement. The highest levels of brightness are obtained in hBN and WSe_2. In summary, even if 2D materials present encouraging results compared to the traditional dyes and nanomaterials, there is still no material that fulfills all the requirements for applicable quantum emitters.

A property that is especially important for biosensing applications is the biocompability of the materials, since they may be in direct contact with proteins. Among all, graphene and hexagonal boron nitride have proven to show a relatively good biocompatibility, while TMDs like WSe_2 present a low cell viability (45 % - 52 %) and therefore have a high toxicity [54][49] [45]. Graphene and hBN consist of an analogue honeycomb lattice structure, with only a lattice mismatch of 1.5% [59]. In both graphene and hBN, atoms (three carbon atoms and a boron and three nitrogen atom respectively) are combined in a hybridized sp^2 orbital to form strong σ covalent bonds [60]. Adjacent layers of both materials are bonded with weak van der Waals forces, with an interlayer spacing of 3.33 Å for hBN and 6.355 Å for graphene. Hexagonal boron nitride has a stacking of AA', which means that B atoms of a layer are positioned between N atoms of the neighbour layers and vice-versa [61]. This is illustrated in Figure 6.

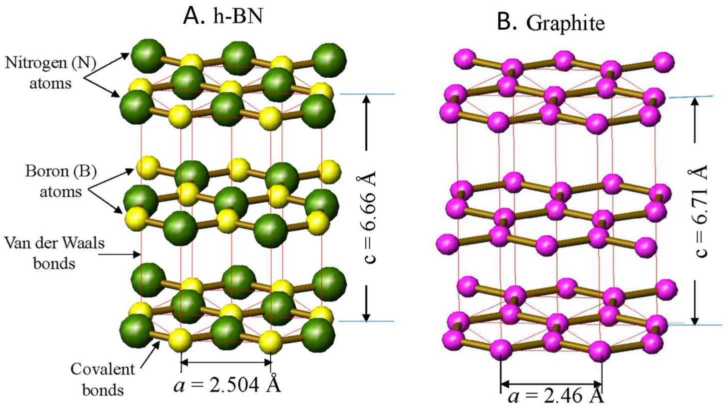

Figure 6: Honeycomb structure, bonds, lattice, interlayer distance and stacking of: **A.** Hexagonal Boron Nitride, **B.** Graphite. Figure adapted from [62].

A key difference between these two materials are their electrical properties. While graphene is a zero-band-gap semiconductor, hexagonal boron nitride has a wide band gap of 5.9 eV [49]. This distinction is relevant for DNA and protein sequencing using FRET. 2D materials with a zero or small band gap (TMDs) are strong quenchers, meaning that they inhibit or suppress the emission of the acceptor, in this case the labelled biomolecule [63][19]. This is not desired since interaction with the biomolecule does not results in a emission of a photon anymore, and therefore cannot be detected. In the case of hBN, it has been shown that it has a low fluorescence quenching, and is therefore a strong candidate for future generations of FRET-based biosensors [64].

Until this point the properties of the most relevant 2D materials for biosensing applications have been reviewed. Among all the options, hexagonal boron nitride appears to be the most suitable for this project because of its biocompatibility, non-quenching property, room temperature performance of their QEs, and their high brightness. In the next subsection, the different ways to produce quantum emitters in these 2D materials will be presented, focusing on hBN.

2.5 Generation of quantum emitters in 2D materials

Since the discovery of quantum emitters in 2D materials, there has been extensive research to understand their origin as well as their deterministic engineering and control of their properties [37]. Due to the large research effort, it has been demonstrated that quantum emitters in TMDs and hBN are caused by atomic defects. However, the type, structure and composition of the defects that host these quantum emitters and their origin are still under discussion [65]. In general, quantum emitters in CVD have been found at random locations, with a tendency to appear at the edges and in wrinkles of the 2D material flake, as well as in regions of high curvature [37][66]. There is evidence that defects are created inherently when flakes are grown [65]. This is undesirable since the control of the location of the defects is essential for photonic devices, leading researchers to develop other techniques to generate quantum emitters deterministically.

Moreover as discussed in subsection 2.3, QEs hosted in 2D materials that operate at room temperatures show variability in their emission wavelength, with ZPL energies distributed over a broad spectral range [65]. Therefore, it is desirable to select a fabrication method that is able to control both the location of the emitters and their emission wavelength. In this subsection, the types of defect as well as the different methodologies to generate quantum emitters in 2D materials will be reviewed. The techniques to produce flakes of 2D materials will be evaluated in subsection 4.2.

As mentioned, optically active defects in materials and their structure-property relation are still under debate. The most well-studied defect and as a result, the most understood is the negatively charged nitrogen-vacancy in diamond. After a decade of fundamental studies, its underlying mechanism is understood, but there are still details in its emission spectrum that are under dispute such as interaction with photons [43]. In the case of the more novel material, hexagonal boron nitride, many types of defects and impurities (carbon or oxygen) have been proposed. The principal candidates are negatively charged boron vacancies (V_B), positively charged nitrogen vacancies (V_N) and anti-site complexes ($V_N X_B$), where the atom X substitutes boron (where $X = C, O, N$), and additionally there is also a vacancy on the nitrogen site [46]. In Figure 7 the different defects are schematically shown:

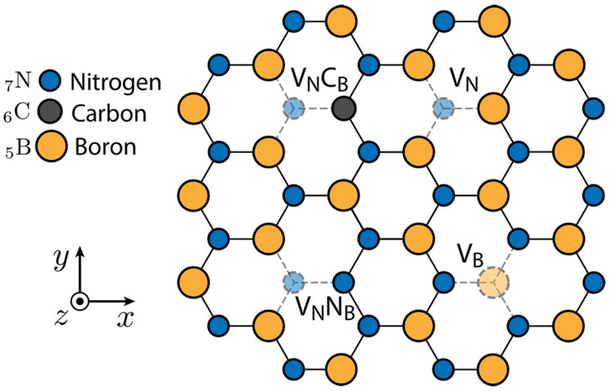

Figure 7: Visual representation of V_N, V_N, V_NC_B and V_NN_B defects in hexagonal boron nitride [67].

In order to generate controlled defect-based quantum emitters in 2D materials, several approaches have already been developed. The methods that are commonly used are electron beam irradiation, ion irradiation, laser ablation, plasma treatment, and focused ion beam (FIB) milling [50][49]. Electron beam irradiation has the capacity to induce defects in the 2D material by bombarding electrons on its surface, producing electron-nucleus or electron-electron collisions during the irradiation [68][69]. Even if the method has shown to generate QEs in controlled locations [70], it presents several drawbacks that are detrimental to final application. In general, irradiation can damage 2D materials with undesired effects like atom displacement, beam heating, charging or radiolysis [71]. Moreover, the irradiation process must be carried under ultra high vacuum since radiation-induced contamination can take place, meaning that complex and expensive set-ups are required [72].The different effects of electron irradiation in 2D materials can be seen in Figure 8.

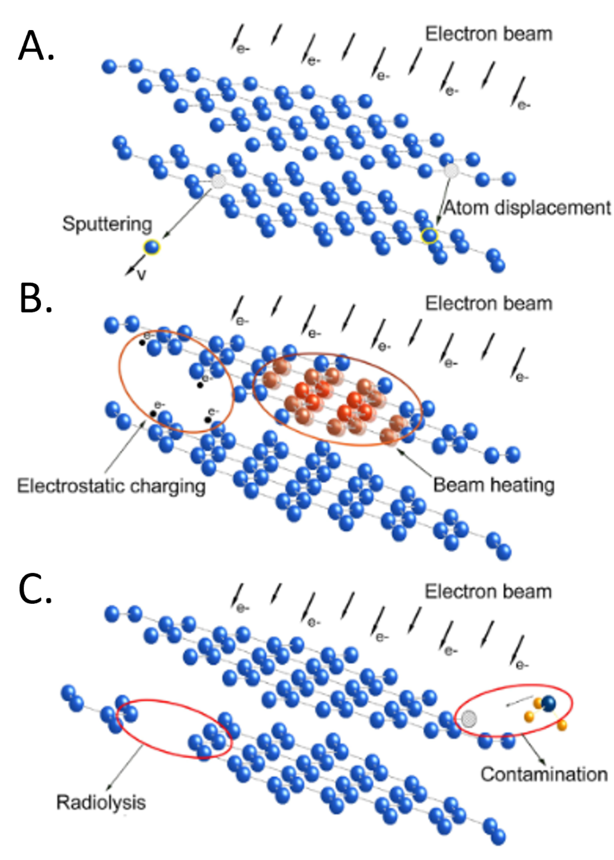

Figure 8: Representation of different damage mechanisms of electron beam irradiation that generate QEs in 2D materials: **A.** Sputtering and atom displacement, **B.** Electrostatic charging and beam heating, **C.** Radiolysis and contamination. Figure adapted from [71].

Analogously to electron irradiation, in ion irradiation a particle with a high mass (usually an positive or negatively charged atom or a molecule), is bombarded on the surface of a target [72]. On the other hand, the use of femtosecond laser ablation has shown to produce defects with a high precision and without need of vacuum and no risk of contamination, a clear advantage to the expensive and complex irradiation-based methods [73][74]. However, the damage to 2D materials generated with laser ablation and ion milling is even more pronounced than with electron beam irradiation. QEs in hBN generated with these two processes, require thermal annealing afterwards in order to partially recover the hBN lattice structure [75][74]. In contrast, electron beam irradiation is a gentler method, and subsequently it does not need thermal annealing.

The effect of plasma treatments such as O_2 plasma etching or Ar plasma etching on hexagonal boron nitride is undesirable, since it has been shown that the generated QEs were not stable, requiring additional processes like thermal annealing to stabilize the emitters [65]. Plasma etching has been applied in different studies which show hBN emitters with a broad range of ZPL wavelengths, ranging from 600 to 800 nm [76]. FIB milling also faces challenges towards the generation of QEs. The high-energy gallium ion implantation required to pattern emitters at precise locations produces changes in the morphology of hBN crystals, leading to damaged amorphous layers, and consequently negatively impacting the ability of the material to host QEs [77] [78]. Ion beam irradiation and redeposition of sputtered material are the main sources of formation of these amorphous layers [78]. Gallium ion implantation also causes fluorescence contamination, which leads to an enhancement of background PL [66][79].

Another approach that has recently gained interest is strain engineering to produce QE. This technique is now widely studied and used to modulate the physical and optical properties of the emitters, by applying elastic strain fields with surface acoustic waves or mechanical deflection [65][80]. By using this approach, shifts in the zero photon lines of hBN QEs of up to 20 nm have been achieved [81][80]. Regarding the generation of QEs, strain engineering approaches to generate quantum emitters in 2D materials by stretching, compression and bending of flexible substrates, and the use of patterned substrates with rigid supports have been experimentally demonstrated. Among these, the use of patterned substrates is more convenient for our end application it keeps the 2D materials in a constant local strained state which is needed for reliable FRET [82]. Some other examples that provide constant local strained states are the use of nanoindentation (Figure 9), gapped golden rods, nanopillars (Figure 10 A and B respectively) or gold nanostars (Figure 11).

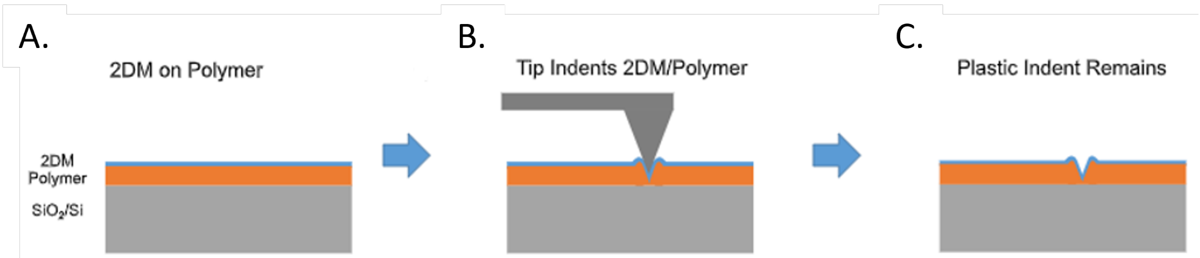

Figure 9: **A.** 2D material transferred onto a polymer which is deposited onto a SiO_2/Si substrate. **B.** Nanoindentation of the 2D material and polymer generated with a tip of an Atomic Force Microscope (AFM). **C.** After the nanoindentation process, the strain caused by the tip remains in both 2D material and polymer. Figure adapted from Rosenberger et al. [83].

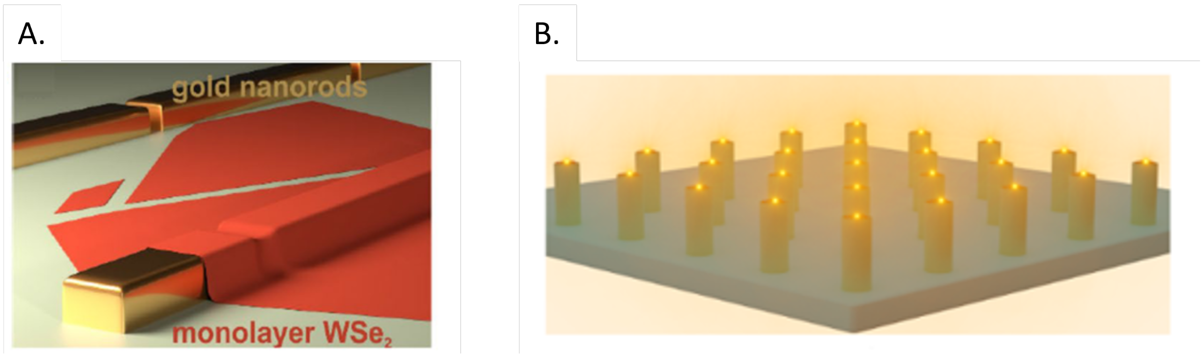

Figure 10: **A.** Monolayer of WSe_2 deposited onto gapped golden rod arrays, leading to strain generation in the 2D material, and therefore the generation of QEs [75]. **B.** Patterned substrate made of nanopillar arrays. The yellow bright spots show the location where the emitters should be generated when an hBN layer is grown on top by CVD[84].

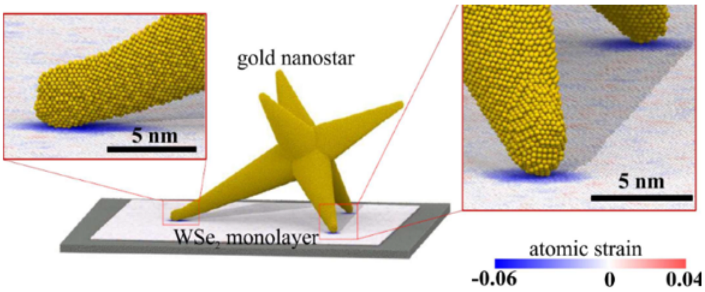

Figure 11: Golden nanostars deposited onto a WSe_2 monolayer. The golden nanostars cause atomic strain in the WSe_2 monolayer with their tips [85].

Strain engineering relies on the fact that the 2D material sheet conforms to the surface topography, creating highly localized strain gradients. Wrinkles or edges which are strained and defective regions respectively also display QEs [86][50]. Overall, the use of strain engineering to generate QEs holds clear advantages compared to the rest of the approaches: the damage caused to the material is low, and no contamination is involved. It is also a more controllable and reproducible method, since beam-shape defocusing and material redeposition in the defect engineering approaches prevent the exact same generation of the defects [87][88]. Moreover, the time that takes for these irradiation-based methods to produce defects are higher, compared to strain engineering methods [89].

Strain engineering thus presents several advantages compared to the alternative methods. However, each technique used to apply strain has different qualities which are important consider, in relation to the aim of the final application. The nanopillar arrays and the gold nano-rod arrays are the most controllable and scalable method, compared to the uncontrollable deposition of nanostars or the low throughput of nanoindentation with AFM tips. If the location accuracy of the QEs is critical, the nano-stars excel on this requirement while the nanopillar arrays and nano-rod arrays have an accuracy in position of 120 nm and 140 nm respectively. In the case of nanoindentation, QEs can be located with an accuracy of 1 μm.

On the other hand, the comparison of the ranges of wavelength emission obtained with each method reveals that the nanopillars and the nanoindentation with AFM are the most reproducible. This conclusion has been reached after observing in the literature that at room temperature, the range of wavelength emission of hBN are 50 nm and 40 nm respectively. In the case of nano-rods and nano-stars, the QEs were hosted in WSe_2 and characterized at 70 K and 10 K respectively. The first method presents a range of wavelength emission of 97 nm, while nano-stars have a range of 11.2 nm. However, the range of wavelength emission of this second method is obtained by only evaluating two QEs, which means that is not a statistical result that can be relied on.

After the evaluation of the state-of-the-art on how to generate QEs, we decided to use strain engineering, since it is the most reproducible and controllable method, and therefore the possibilities to obtain QEs with similar properties are higher. Specifically, we decided to produce strain with micro/nano-structure arrays, because of their scalability, control and reproducibility.

The next step is how to quantify the strain produced on the material with the chosen technique, and to know the necessary strain to create QEs in hBN. This is needed to better understand what happens when strain is generated in a 2D material. Essentially, the external mechanical strain changes the interatomic separation of the atomically thin 2D material and therefore also its properties [90]. When tensile strain is applied, the length per bond increases, with the bonds becoming weaker the further the distance between atoms. In the case of compressive strain, the chemical bond decreases its length and becomes stronger. If the strain exceeds a certain threshold, it can lead to the breaking of bonds, resulting in the creation of a vacancy or defect site which can act as a QE. The natural frequency (ω) of the 2D material is directly proportional to the bond strength between atoms (represented as force constant (k) and their mass is m), see Equation 1, decreasing when tensile strain is applied and increasing in the case of compressive strain [91]. As explained in detail in subsubsection 4.3.4, this shift of vibrational frequency can be detected easily with Raman spectroscopy when the 2D material is strained.

$$\omega = \sqrt{\frac{k}{m}} \tag{1}$$

In the literature, 2D materials appear to be able to deform over 10% before rupture, in comparison with the 1% of possible deformation when they are found in their bulk form [92]. Also, the amount of strain generated with each strain engineering method like flexible substrates and their bending are described analytically. However, in the case of patterned arrays, the local strain caused on the 2D material is inhomogeneous, complicating its analytical description. Empirically, it has been shown that with this method the range of strain achieved in different 2D materials is between 0.5 % and 6.4 % [82][90]. The amount of necessary strain to generate QEs with patterned substrates is still unclear and is still a largely unexplored topic. One value that appears in literature is found for draped WSe_2 on golden nano-rods, where the regions in which defects were generated reached strain percentages of 0.5 % and 0.9 % [75].

2.6 Design of an hBN nanoprobe for biosensing

As discussed in the previous subsection, a promising method to generate QEs in a 2D material is via strain engineering. This section therefore reviews the use of micro/nano-structured arrays in hBN strain engineering and summarizes the most important parameters to consider when designing an optical probe for FRET measurements.

When looking for research that combines micro/nano-structured arrays and hexagonal boron nitride, two main studies deserve mention. In the study of Li et al., the hBN was grown onto a SiO_2 susbtrate with chemical vapour deposition (CVD) [84]. They fabricated truncated cones arrays with diameters of 250, 450, 650 and 950 nm and a height of 650 nm. In the results, the 250 nm show the most intense fluorescence, which decreases with the increasing size of cone diameter, see Figure 12. With the 250 nm diameter, single photon emitters are observed in 80% of the pillars. Also for the 950 nm nanopillars, multiple emitters are seen. The authors only characterise the QEs obtained from the 250 nm at room temperature, where the majority of the wavelengths emission between 550 and 600 nm. Even if the results are promising, the authors of the paper claim that strain engineering has no correlation with the formation of QEs, claiming that the defects are generated because of the nucleation on the pillar sites caused by CVD growth.

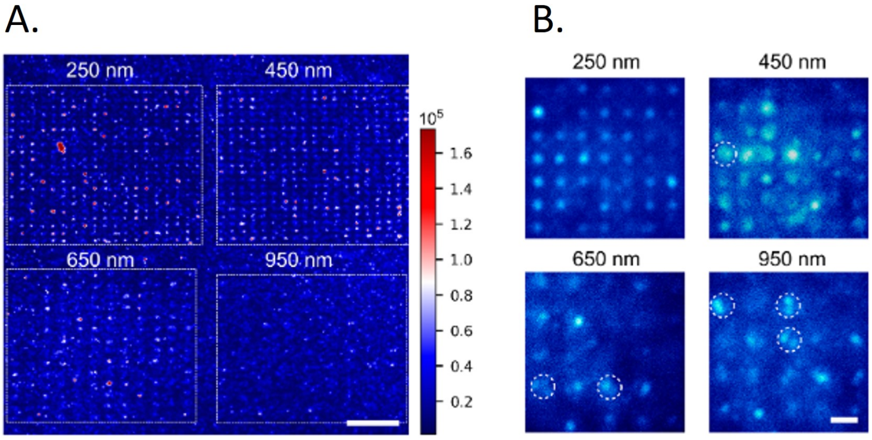

Figure 12: A. Confocal PL intensity maps of hBN QEs located on pillars of 250, 450, 650 and 950 nm of diameter size. **B.** Wide-field images of each hBN QEs located on each pillar array. The white circles show the pillars that host multiple QEs. Scale bar: $2\mu m$. It should be noted that the distance between pillars is $2\mu m$ and $3\mu m$ for the 250 and 450 nm nanopillar arrays and the 650 and 950 nanopillar arrays respectively. Figure adapted from [86].

In contrast, Proscia et al. claim that strain engineering is responsible for the generation and activation of QEs, since the QEs are localized near the edges of nanopillar arrays, and therefore where the local strain reaches a maximum [86]. They also specify that no other technique such as thermal temperature annealing or irradiation is used to activate the defects. Moreover, to further support their hypothesis, they try different geometries of the nanopillars. In this case, they also grow hBN flakes with CVD but these are afterwards transferred to the patterned SiO_2 nanostructures. It is also specified that the flakes are 20 nm thick, and after the transfer some regions are covered by one layer and others two layers of hBN. However, during characterization this thickness difference is not studied. The cylindrical nanopillars had a height between 100-155 nm, and a diameter between $75 - 2\ \mu m$. The characterization results show that there is spectral diffusion, meaning that there is a gradual shift in the energy of the QEs over time. However, neighbouring QEs maintain the overall structure and wavelength emission as seen in Figure 13. It should be noted that heights greater than 155 nm would pierce the hBN.

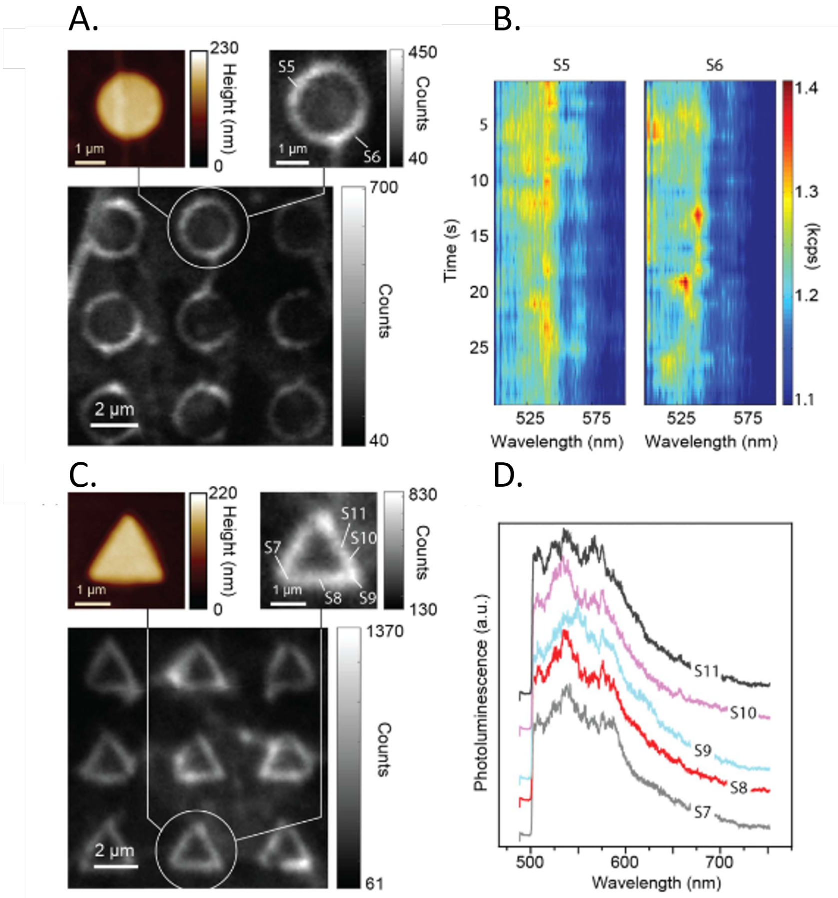

Figure 13: **A.** QE activation and location at the edges of the round shaped nanopillars. **B.** Wavelength emission spectrum as function of time of the QEs S5 and S6 found in picture A. **C.** QE activation and location at the edges of triangular shaped nanopillars. **D.** Integrated emission spectrum of QEs named from S7 to S11 found in image B. The integration time is 10 s. It should be noted that the spectra of each emitter has been displaced vertically for clarity. Figure adapted from [84].

When analysing these research papers, it becomes clear that certain points are not covered: How does the thickness of the hBN flake influence the formation of QEs and how would it influence in strain engineering? How does the shape and dimensions of the nanopillar arrays influence the QEs? What would happen if another substrate material was used? With the contrasting results from literature, it is important to determine if localized strain engineering is sufficient to generate and activate defects, and if so how much strain is needed to generate a QEs. Given these still open questions we decided to further analyse studies that use hBN strain engineering and the use of micro/nanostructures.

Thickness dependence:

Regarding the thickness of the hBN flakes and its effect on the generation of QEs when strained, Tran et al. studied the effect of monolayer and multilayer hBN flakes on the emission properties of the QEs [93]. The defects are generated by CVD growth and activated with argon annealing, resulting in randomly located QEs. In both monolayer and multilayer, the ZPL appears at 623 nm. However, in the multilayer case, the emission lines are much narrower compared to the monolayer QEs, as seen in Figure 14. Furthermore, the QEs hosted in the multilayered hBN are more photostable. On the other hand, Wang et al. studied the interlayer stress transfer of exfoliated hBN [94]. In the study it is claimed that 99% of the stress of hBN layer is transferred to the following layer, compared to the 60% – 80% in graphene. This means that the bonding between hBN layers is stronger than in graphene. Using Raman spectroscopy and assuming that a single layer has a thickness of 0.333 nm, it can be seen that there is a wavelength emission shift rate per percentage of strain of the hBN flake. This shift rate gradually decreases when the number of layers becomes higher as seen in Figure 15.

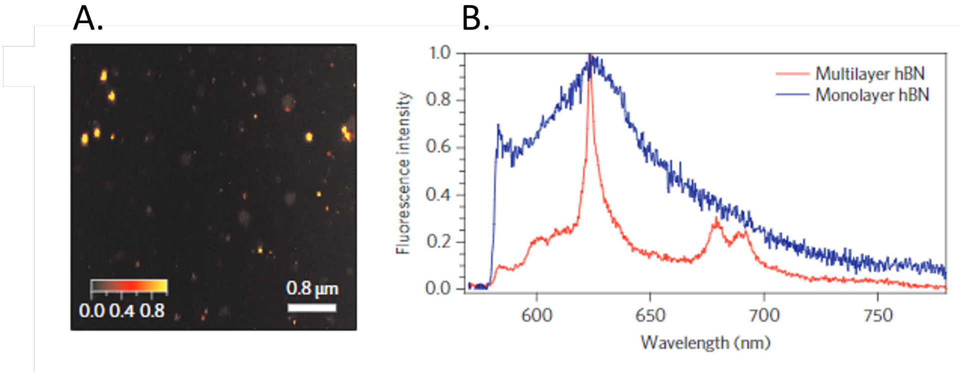

Figure 14: **A.** Confocal map of a multilayered hBN sample. The bright spots correspond to the photoluminescence of the quantum emitters. Wavelength of the excitation laser: 532 nm. **B.** Emission spectra of a QE hosted in the monolayered hBN in blue, and in the multilayered hBN in red. Figure adapted from [93].

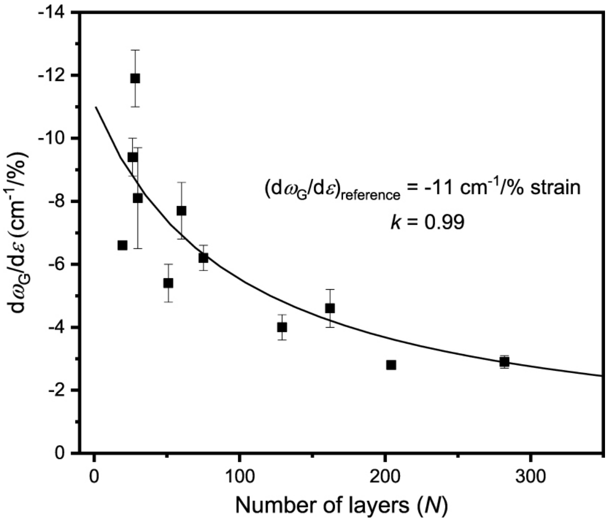

Figure 15: Raman band shift rate per percentage of strain expressed in $cm^{-1}/\%$ of hexagonal boron nitride as a function of the number of layers at an excitation wavelength of 488 nm [94].

Substrate effect:

In the state-of-the-art is has also been reported that the substrate material has a strong influence on the quantum emitter properties. As shown in Figure 13 and in Figure 16 (a), the hBN quantum emitters generated on SiO_2 substrates blink and have noticeable spectral diffusion. In the study carried by Li et al., this behaviour is shown in the emission range between 580 and 700 nm. In the same study as shown in Figure 16 (b), when the hBN flakes are placed on top of alumina, the spectral diffusion and the blinking behaviour is significantly reduced over the entire measurement period of 500 s. Similarly, the same effect is achieved when PDMS is used as substrate material, where the emitter emits energy at a wavelength of ~600 nm, as shown in Figure 17.

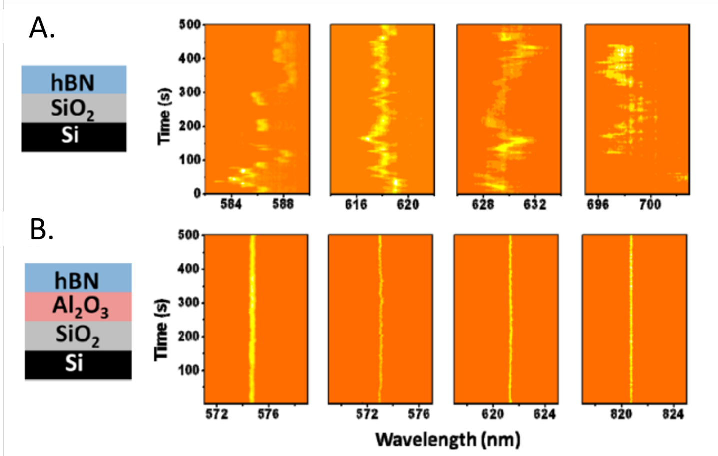

Figure 16: **A.** Spectral emission of hBN QEs when the hBN flake is placed in a SiO_2 substrate. **B.** Spectral emission of hBN QEs when the hBN flake is placed in a Al_2O_3 layer of a thickness of 2 nm. Both spectral emissions are measured for 500 s at an excitation wavelength of 532 nm. Figure adapted from [95].

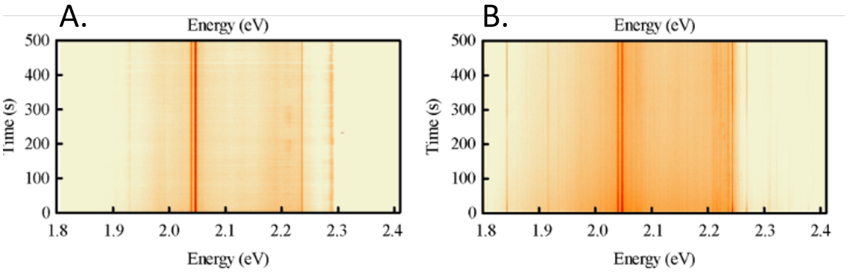

Figure 17: Spectral emission over time of a QE hosted in hBN powder deposited onto PDMS. **A.** the measurement is performed at room temperature (296 K). **B.** Measurement done at cryogenic temperatures (5 K). Figure adapted from [96]. Excitation wavelength of 514.4 nm.

In this project, knowing the effect of the substrate is highly relevant, since transparent substrates are required. The main reason for this necessity is the employment of an inverted epi-fluorescent microscope for the measurement with biomolecules. As shown in Figure 18, the set up of the inverted epi-fluorescent microscope has a light path that is entirely below the sample. The laser excitation and the signal detection go through the same objective placed under the sample. The hBN flake with optical emitters is placed on a transparent substrate which faces the bottom of the flow cell. Biomolecules are flushed inside the flow cell where they can interact with the hBN QEs (Figure 18). The importance of this set up is to keep a similar refractive index with the droplet and the transparent substrate in order to avoid scattering of the light, and therefore obtain high resolution images. In subsubsection 4.3.1, further details on fluorescence microscopy are given.

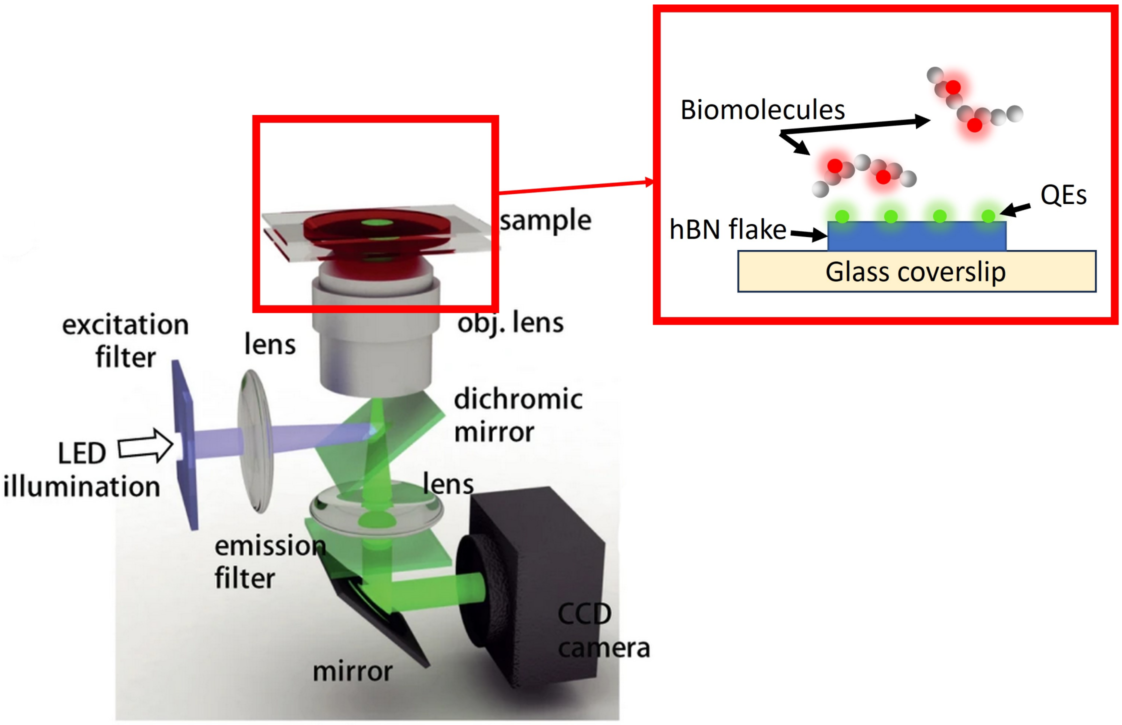

Figure 18: Experimental set up of an inverted epi-fluorescent microscope, where the excitation filter filters the unwanted wavelengths. The remaining filtered excitation light interacts with the specimen, exciting the fluorophores which then emit light at higher wavelength. The light passes through the dichroic mirror, which separates the excitation light (directed towards the observation path) from the emitted fluorescence. Finally, an emission filter transmits only the desired fluorescence wavelengths, which then reach the camera. In the red square a detailed set up of the sample is shown, where the biomolecules interact with the QEs found in hBN, and the 2D material is deposited onto a glass coverslip. Figure adapted from Cho et al. [97].

The requirements of the transparent substrate material are: **(1)** Transmission of light from the excitation of the laser wavelength (523 nm), to the highest light wavelength emission of the hBN defects (750 nm). In other words, transmission of light in the visible and near-infrared (NIR) spectrum. **(2)** Rigidity to ensure the substrate does not buckle during the measurement.

Only a limited number of studies focused on the use transparent materials for the substrate, with PDMS the only option that has been studied. However, to maintain a constant local strained state, a rigid material is needed. Since PDMS is a flexible material, we decide to use rigid materials that may facilitate the manufacturing process. Transparent substrates such as glass has been widely used for various applications involving micro and nanostructures such as microfluidics, due to its unique properties such as transparency, optical clarity and chemical inertness [98]. Nevertheless to generate micro-structures on them is challenging. In other words, their optical manufacturing is not efficient due to their spectrally wide transparency of these materials. An alternative that allows their easy processing with ablation is the use of the femtosecond laser.

3 Research Question

To summarize, the main goal of this master thesis is to investigate whether solid-state nanomaterials based on 2D crystals can be superior alternatives to the traditional optical emitters of FRET-based sensors. The understanding of the photophysical properties of quantum emitters in these nanomaterials would enable an improved performance as probes for protein sequencing. The insights from the state-of-the-art have led to the initial experimental design decisions. These decisions will help to focus the scope of the research and are summarized below:

1. **Choice of a nanomaterial**: In subsection 2.3, the requirements of the QEs have been established according to the characteristics of optical probes for smFRET. Subsequently, the possible alternatives to traditional optical emitters have been presented, with 2D materials displaying the most promising properties. In subsection 2.4, the most common materials used for the production of QEs have been reviewed. From there, we presented literature showing that the reproducible generation of QEs hosted in hBN is challenging. However, this material is biocompatible and does not lead to fluorescence quenching. Furthermore, its QEs are bright, and perform at room temperature, which are a fundamental requirements when working with proteins. Therefore, it has been decided that in this master thesis the nanomaterial that will be used is hBN.
2. **Method for generating QEs**: The methods to produce defects and as a result potential QEs have been reviewed in subsection 2.5. There, we show that strain engineering may be a cleaner procedure compared to other methods. Its use is also beneficial since provides more control and reproducibility of the defects together with high throughput production. Therefore, we decided to focus on the generation of QEs via strain engineering. Specifically, we chose to use micro/nano-structure arrays, since they are the most scalable, controllable and reproducible way to create constant strain in localized areas.
3. **Material of the substrate**: As seen in subsection 2.6, the substrate material should be transparent and rigid. However, the state-of-the-art has typically used SiO_2/Si for the generation of micro/nano-structures. In order to compare our results properly with the literature, we plan to study strain engineering mainly with SiO_2/Si. However, we aim to expand it to borosilicate glass. In addition, to investigate the relationship between strain of hBN and aspect ratio of the structures, we decided to add beads (used as structures) and the micro/nano-structures of a commercial CD and Blu-ray disk to give a variety of profiles.

3.1 Knowledge gap

Despite the novelty of 2D materials, there is already a large amount of information about the properties of the QEs they host. It is also clear that even if QEs have promising properties, the main limitation for protein fingerprinting application is the control of their position, and the wide range of emission. As a result, QEs in 2D materials are being widely studied. However, the generation of hBN QEs via micro/nano-structure arrays not been investigated in great depth.

An evident gap in the knowledge is the lack of information on the effect that micro/nano-structure arrays have on hBN. The two most relevant studies about this topic state contradictory results. While one of them claims that the defects are not correlated with the strain, the other says that the strain has not only generated but also activated the QEs. There is also in general a lack of consistency in the standardization of the experiments. Each research group has a completely different approach e.g. depositing the hBN on the substrate differently, creating different structures with different magnitude of dimensions and shapes. Therefore, it is still not clear if micro/nano-structure arrays can produce defects due to strain, and how the shape and dimensions of these influence the properties of the QEs.

Another knowledge gap is how the thickness of the hBN affects the properties of the QEs if they are generated with strain. As discussed in subsection 2.5, strain has the capacity to modulate the wavelength emission of the QEs. Moreover, QEs generated with CVD have a narrower emission when they are in multilayered hBN than in monolayered hBN, which could be linked to the amount of strain transmitted through multiple layers. However, in the first study the strain is unknown and in the second effect of strain in hBN layers has only been studied without defects. In summary, it is unknown if the number of layers together with the strain will substantially affect the emission of the QEs.

The third knowledge gap is related to the impact on the characteristics of QEs with rigid transparent materials. Since the majority of the studies are done with SiO_2/Si substrates, it is not clear how different types of materials, such as glass or a polymers, influence the photophysical properties of QEs.

3.2 Research questions

After analyzing in detail the state-of-the-art of the field and identifying the gaps in our knowledge, we can now define four main research questions:

1. Can quantum emitters be created with strain engineering?
2. How does the dimensions and shape of the micro/nanostructures influence the formation of quantum emitters?
3. How does the thickness of the hexagonal boron nitride flakes influence the properties of the quantum emitters?
4. How does the material of the substrate influence the properties of the quantum emitters?

An experimental approach performed in parallel to COMSOL modelling has been designed in order to investigate these research questions. In next subsection will outline the steps in which the experiment has been divided, and the methodologies that will be used to accomplish them.

4 Experimental Approach

The experimental approach of this master thesis has been divided in three main steps:

1. **Fabrication of micro/nano-structure arrays:** In this step, the micro/nano-structure arrays are fabricated. As mentioned in section 3, we want to understand how the shape and size of the micro/nano-structures affect the generation of QEs due to strain. Therefore, three different types of structures will be used: **1.** 10 μm polystyrene beads and 5 μm polystyrene red fluorescent bead, gifted from the EWI faculty microfluidics group. These will be deposited on a SiO_2/Si or glass substrate (Figure 19 A). **2.** Arrays of cavities generated with femtosecond laser ablation on a SiO_2 and glass substrate (Figure 19 B). **3.** The third method takes advantage of the structures of the polycarbonate layer of a commercial CD (Figure 19 C), and the silver layer of a Blu-ray disk.

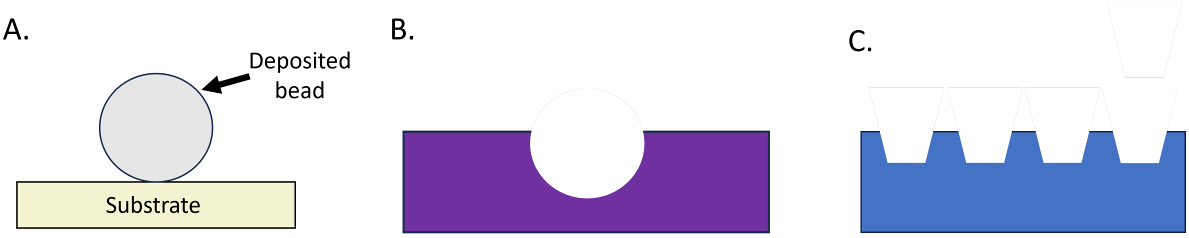

Figure 19: Schematics of the different micro/nanostructures used in this project **A.** Deposited microspheres onto a glass or SiO_2/Si susbtrate. **B.** Ablated cavities in glass or SiO_2/Si with a femtosecond laser. **C.** CDs and Blu-ray micro/nanostructures.

We decided to proceed with these structures since: 1. Beads are inexpensive. 2. Femtosecond laser ablated substrates are easy and fast to manufacture. 3. CDs and Blu-ray discs are inexpensive and highly reproducible. We decided to check the dimensions and shape of the structures in terms of curvatures, and see if the curvature had a direct impact on the generation of QEs in hBN. It was decided not to use nanopillars since these structures might collapse when stamping hBN onto them. The amount of curvature produced by each structure is found in Table 3. These were calculated as following: In the case of the beads, the curvatures were calculated as 1/Radius of the bead. In the rest of structures, the curvatures were calculated with Lorentzian curvature fitting. More information of the procedure can be found in Table 6.2.

Type of structure	Curvature (1/m)
10 μm beads	2×10^5
5 μm beads	4×10^5
Femtosecond laser ablated cavities	$4.45 \times 10^5 \pm 1.26 \times 10^5$
Structures of the CD	$3.9 \times 10^5 \pm 1.87 \times 10^5$
Structures of a Blu-ray	$4.63 \times 10^6 \pm 1.68 \times 10^7$

Table 3: Comparison of the curvatures of the different used structures.

2. **Stamping of hBN on the micro/nano-structure:** Once the micro/nano-structure arrays are obtained, the hBN flakes are stamped on the beads and cavities, by using the stamping setup shown in Figure 25. In the case of the CD and Blu-ray structured arrays, the hBN flakes are directly exfoliated onto the substrate. Both processes are explained in subsection 4.2.
3. **Characterisation of samples:** Once the hBN flakes are stamped/exfoliated on the micro/nano-structure arrays, the presence of QEs is going to be evaluated with fluorescence microscopy. The topography of both the micro/nano-structure and the hBN flake on the micro-nano structure will be characterised with the atomic force microscope (AFM) or optical microscopy. Both techniques

help to understand the dimensions of the structure and how the 2D material is draped on the structure. In order to complement the AFM analysis, the samples are further characterised with scanning electron microscopy (SEM). Strain is afterwards measured with Raman spectroscopy, and QEs are characterised with photoluminescence imaging.

The subsections below describe the methodologies that will be used in each stage of this project.

4.1 Fabrication of micro/nano-structure arrays

4.1.1 Beads deposition on a substrate

At the beginning of the experimental process, different sizes of beads (specifically of 100 nm, 200 nm, 1.5 μm, 5 μm, and 10 μm diameter) were considered. Each size of beads were initially dispensed in a solution with water of unknown concentration. Before depositing them on the silica or glass substrate, the substrate was first put under oxygen plasma during 10 minutes in order to increase its hydrophilicity. In this way, the droplet of water containing the micro/nano-beads could expand all over the surface of the substrate. This high hydrophilicity together with the immediate application of temperature allowed a good separation and distribution of the beads, without excessive clustering, in the case of 5 μm and 10 μm (Figure 20). The smaller beads more easily aggregated together and therefore made it difficult to subsequently stamp hBN flakes on individual beads. For this reason, these bead sizes were discarded from the study.

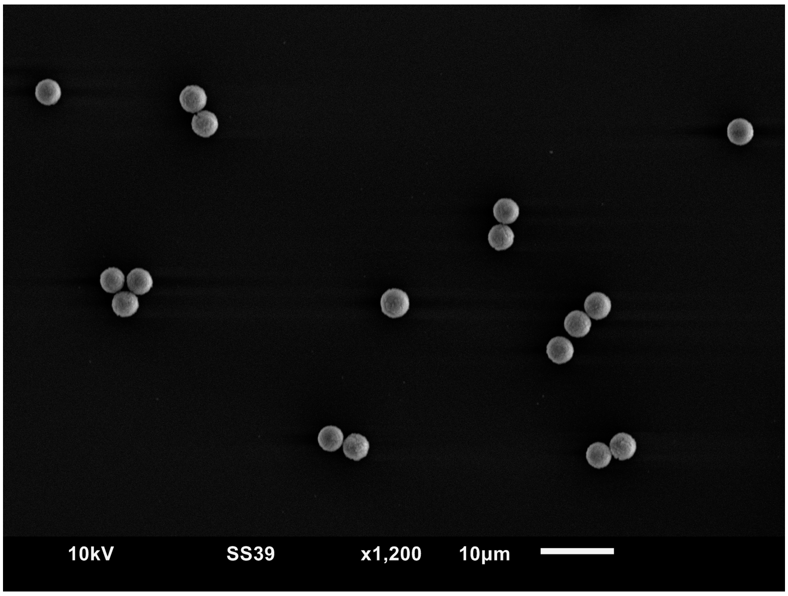

Figure 20: Distribution of 5 μm beads after deposition. Image obtained with SEM.

4.1.2 Fabrication of cavities with femtosecond laser ablation

Compared to the traditional lasers that emit longer pulses or that use continuous waves, the femtosecond laser uses ultrashort pulses of femtosecond duration ($10^{-15}s$) [99]. This feature offers several advantages, for instance it is a non-thermal process since its pulse ends before the electrons thermally excite any ions [100]. Due to the nonlinear absorption mechanism i.e. multi-photon absorption, the femtosecond laser has the capability to pattern a versatile range of materials, including transparent materials such as the borosilicate glass used in this project, that are otherwise difficult to process using traditional lasers [101].

It should be noted that every femtosecond laser machine has a slightly different setup. In Figure 21 a general setup of a femtosecond laser is shown, where (1) corresponds to a femtosecond laser. The beam is collimated and circularly polarized with a wave plate (2), modulated by a beam modulator which acts as a shutter (3), turning on and off the laser when necessary [102]. Next, the diaphragm is in charge of improving the quality of the laser (5), after the laser passes through two mirrors and a polarizer and next it is deflected in the X and Y axis of the sample with the help of a two-axis galvanometer scanner (8) and a focusing lens (9). The sample, which is placed in front of the output of the lens at its working distance, is fixed on the XYZ stage (11). In this project, the manufacturing process will be performed with the setup of the micromachining machine LS-Lab, with a Pharos laser (Light Conversion, Lithuania) of 520 nm of wavelength and a focal lens of 100 mm. The arrays of cavities were fabricated by creating arrays of 3 mm lines, separated by 0.1 mm. The parameters used in the femtosecond laser are found in Table 4.

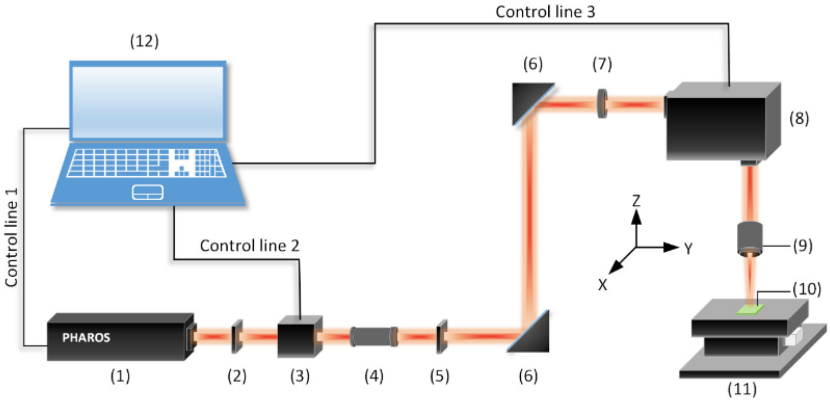

Figure 21: General commercial setup of a femtosecond laser micromachining machine [102]:(1) Fs-laser (2) Wave plate (3) Beam modulator (4) Beam expander (5)Diaphragm (6) Mirror (7) Polarizer (8) Galvanometer scanner (9) Objective (10) Sample (11) XYZ mechanical transitional stage (12) Computer.

Parameter	**Value**
LaserOn Delay	260 μs
LaserOff Delay	260 μs
Jump Delay	300 μs
Mark Delay	300 μs
Jump speed	500 mm/s
Speed	3000 mm/s
Repetitions	1
Sky-writing mode	True
Pulse rate	75018 Hz
Power	SiO_2/Si: 1 %, Glass: 1 % - 10 %

Table 4: Setting of the femtosecond laser for the creation of cavities

As shown in Table 4, the power used for the fabrication of cavities is different for silica and glass substrates. The main reason for this is the sharpness of the features in the arrays, which is important for the reproducibility of the structures. This difference between substrates can be observed in Figure 22, the shapes become more irregular as the power is increased during the fabrication of silica structures. On the other hand, when the power is increased during the fabrication of glass structures, the shape remains reproducible, and only the diameter of the cavities changes. Also we also note that during this experiment (Figure 22 A and B) the lines have to be at least 1 mm long in order to obtain single cavities. Increasing the line length, increases the cavity distance.

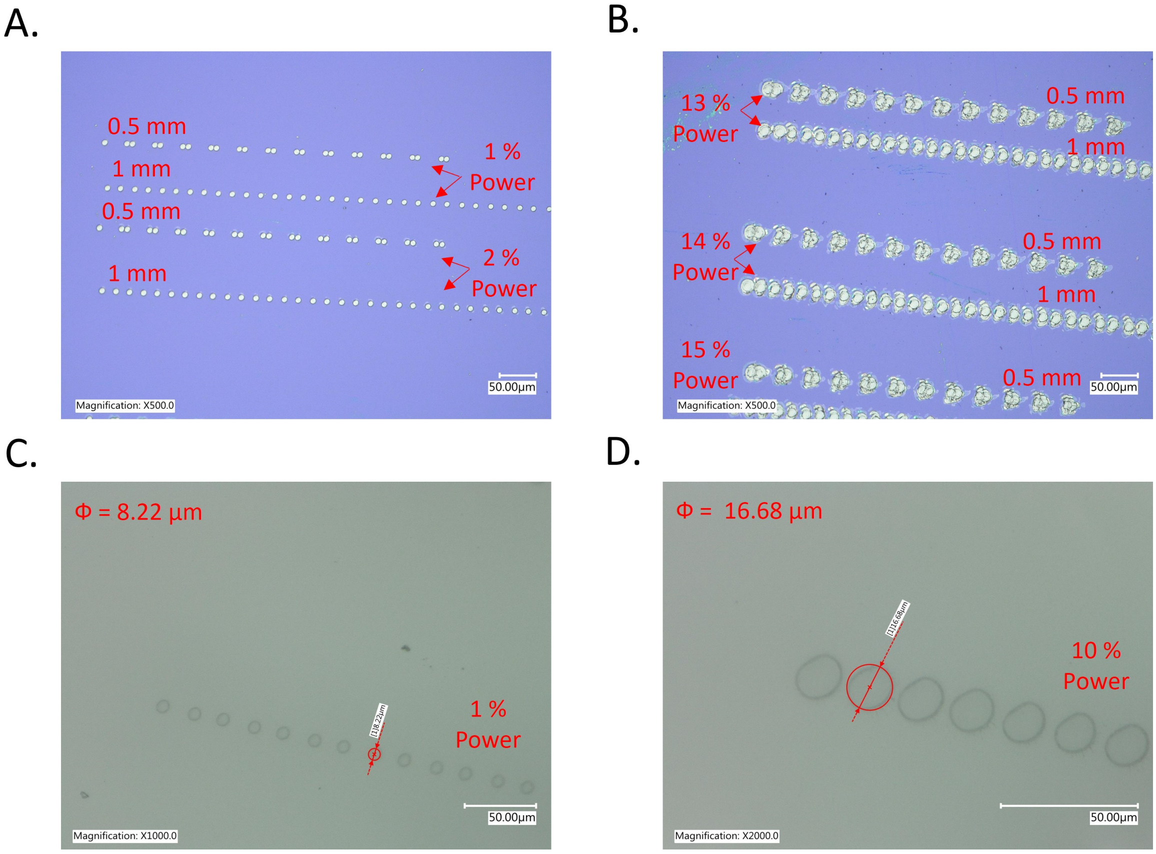

Figure 22: Optical images of the cavities in silica when ablating 0.5 mm and 1 mm lines, the number of repetitions is fixed to 1, and the power is changed to **A.** 1 % and 2 %. **B.** 14 %, 15 % and 16 %. Optical images of the cavities ablated in glass when ablating 1 mm lines, the number of repetitions is fixed to 1, and the power is changed to **C.** 1 %. **D.** 10 %.

4.1.3 Obtainment of CD/Blu-ray structures

CDs and Blu-ray discs store information by using a technology called optical storage. The surface of the CD contains a series of microscopic pits and lands, where changes between these pits and lands represent ones, and no change represents zeros of digital data [103]. The information is read with a laser. When the laser hits a pit, the light is scattered and contrarily, the light is reflected when the laser hits a land. The reflection and scattering of the laser beam are detected by a sensor, which translates this input into digital data. Blu-ray discs use the same principle but have a higher data storage capacity than CDs, since the information is read with a blue laser, increasing dramatically capacities and data transfer rates over CDs and DVDs [104]. Consequently, their pits and lands are smaller and are more tightly packed than those on a CD. Nowadays Blu-ray discs can store up to 128 GB of data, while CDs can store up to 700 megabytes.

In order to from profit the already existent structures of the CD and Blu-ray, the only required step is to separate the silver layer from the polycarbonate layer. The reason why the polycarbonate layer of the CD is used instead of the silver layer, is because the silver layer is adhered to an opaque film, which makes unsuitable for imaging in the inverse fluorescence microscope. The plastic layer of the Blu-ray disk was not used, since it was too thin and fragile, and easily broke. The topography of both structures can be seen in Figure 23, which was taken using tapping mode AFM.

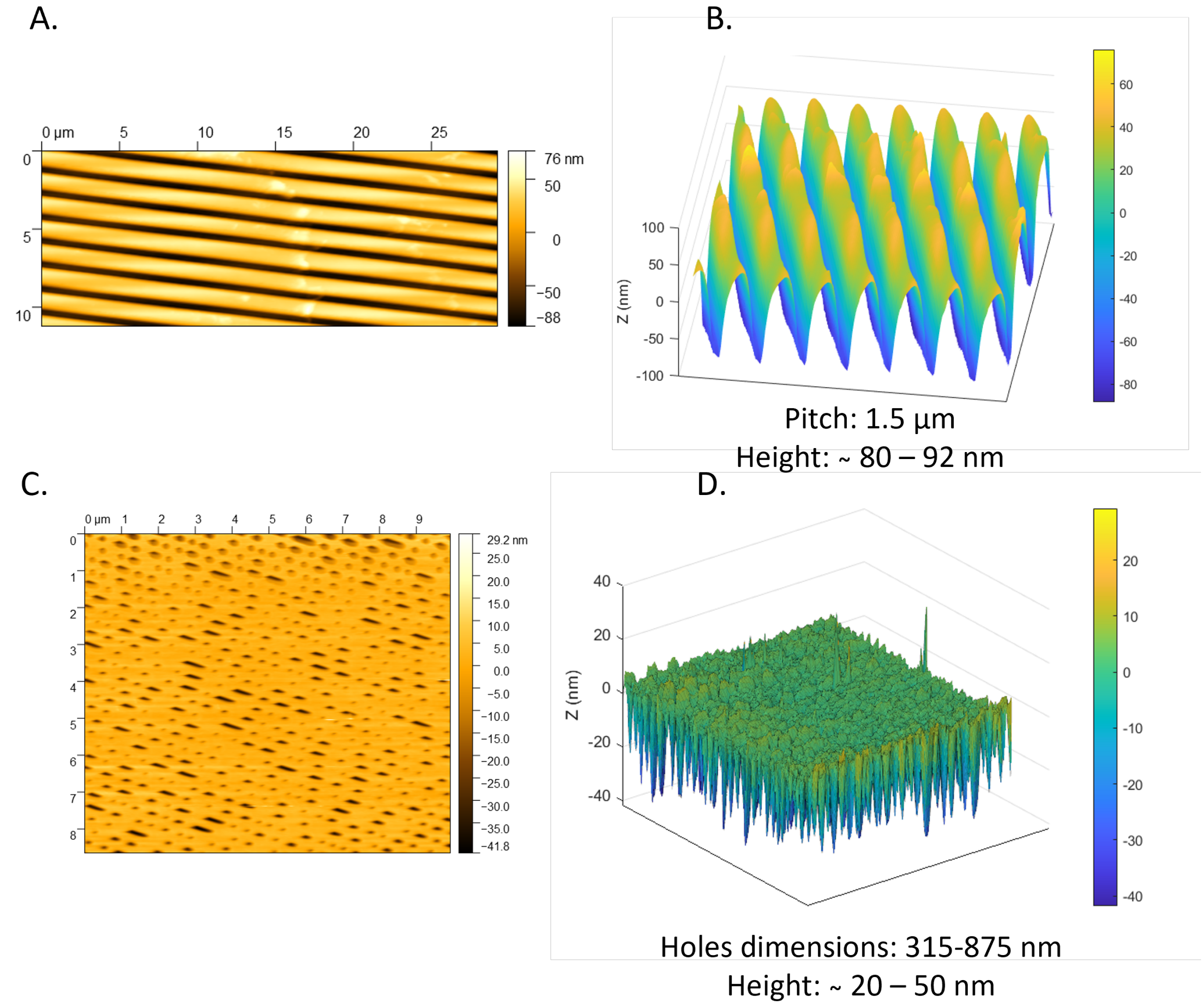

Figure 23: **A.** Topography image of the polycarbonate layer of the CD. **B.** 3D image of the structure of the CD and its approximate dimensions. **C.** Topography image of the silver layer of the Blu-ray used in this project. **D.** 3D image of the structure of the Blu-ray and its approximate dimensions.

4.2 Stamping of hBN on the micro/nano-structure

The hBN stamping process consists of two main steps: **(1)** Obtaining flakes from bulk hBN, **(2)** Stamping a desired region of flakes onto a micro/nano-structured substrate.

The first important step is to obtain high quality hBN flakes while not generating defects during its production process. hBN can be produced by top-down and bottom-up methods, for instance by mechanical exfoliation and chemical vapor deposition (CVD) respectively [105]. Mechanical exfoliation using Scotch tape is a simple and inexpensive method that generates the highest quality 2D materials [106]. Nevertheless, it is not appropriate for large scale of 2D materials and it is challenging to control the number of layers of a flake and its size. On the other hand, CVD is better in terms of scalability. However, defects are inherent in 2D materials grown by CVD, which is not suited for this project [107]. The absence of defects is essential and the high degree of control of the properties (thickness and dimensions) of the layer is not as relevant. For this reason, the flakes of this project will be generated by mechanical exfoliation.

The production of flakes with Scotch tape is as follows. First, the hexagonal boron nitride is deposited on Scotch tape. After, the tape is pulled away, attaching flakes of hBN on the tape. During this process of exfoliation two type of forces come into play: a normal force and a shear force. The first one directly overcomes the van der Waals bond between layers, separating the layers vertically. Meanwhile, the second one, displaces the layers laterally. Simultaneously, the interlayer covalent bonds can break, making the layers smaller [106]. The Scotch tape will be folded and unfolded several times so the flakes of hBN become thinner. To directly transfer these flakes to a substrate, the tape is positioned directly onto the substrate and afterwards is pulled off, leaving behind a several flakes adhered to the substrate. This method will be used only to transfer the hBN flakes onto the CD and Blu-ray surfaces, since the periodicity and density of the micro/nanostructures do not require an accurate control over the position of the flakes.

In the case of cavities and beads, the accuracy of the positioning of the flakes is more important, since the hBN flakes need to centered with respect to the structures. For these arrays, transfer of hBN flakes through deterministic stamping is employed instead. As shown in Figure 24 A (on the left), for the transfer through stamping, the tape full of hBN flakes will be stuck on a piece of solid polydimethyldiloxane (PDMS) (Figure 25 A) and again will be stripped. This will adhere some hBN flakes to the PDMS. It will be checked which flake has the desired dimensions under an optical microscope. The ideal flake for the planned experiments should be thin (maximum thickness of 200 nm), and it should also be large (around 100 μm). With these properties the flake can be easily strained and easy to stamp on patterned surfaces. It is also important that the flake has a surface without many wrinkles, since QEs have a tendency to appear on the edges and wrinkles of the flake, and make it challenging to determine the QEs density due to the patterned substrates. It should be noted that the thickness of the flake can be easily estimated by their color. During the experimental process, the thickness of several flakes were accurately measured with the atomic force microscope.

After identifying the region where the desired flake is located, the flakes of this area will be stamped to the patterned substrate. This will be done with a precision stamping set up with macromanipulators (Figure 25 B), making contact only on the relevant area of the PDMS, and stamping the flakes more selectively. The micro/nano-structured substrate is placed in the stamping setup under the PDMS which contains the flakes (Figure 24 B). The area of the PDMS with the flake of interest is positioned over the desired micro/nano-structure. The glass microscope slide containing the PDMS is gradually lowered until the flake comes into contact with the substrate. The substrate holder is heated to 60 $^{\circ}C$, so the adhesion between the PDMS and the flake is reduced. The contact between surfaces is released by gradually raising the PDMS away from the substrate. Once the PDMS layer is removed, the flake is deposited onto the micro/nano-patterned substrate and the sample is ready to be analysed.

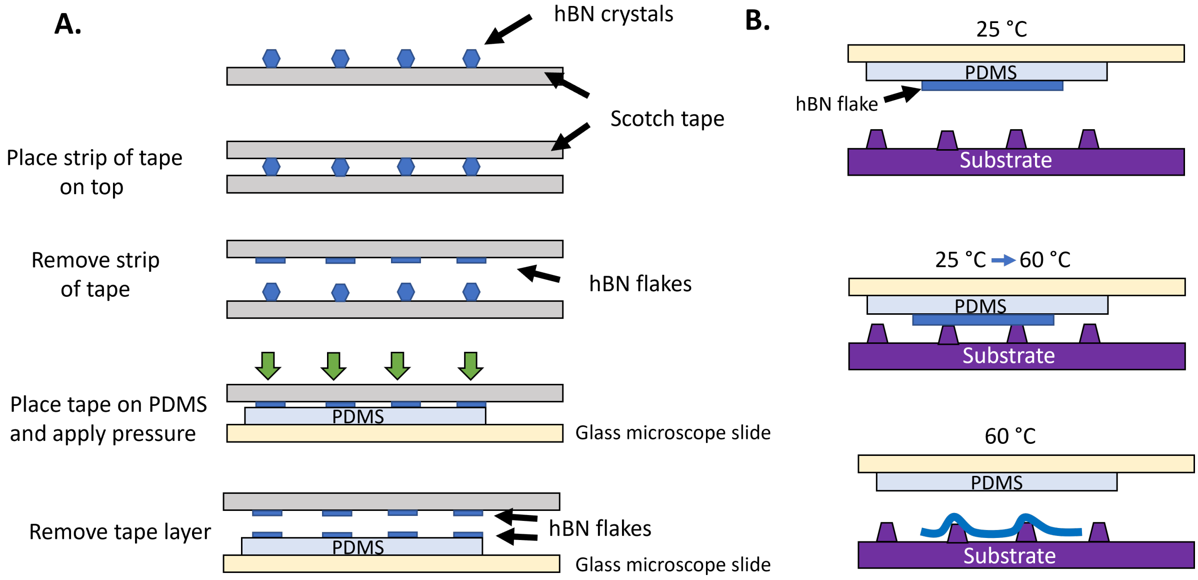

Figure 24: A. Exfoliation of hBN crystals and transfer to PDMS layers. **B.** Stamping of an hBN flake of interest on the micro/nano-structured substrate.

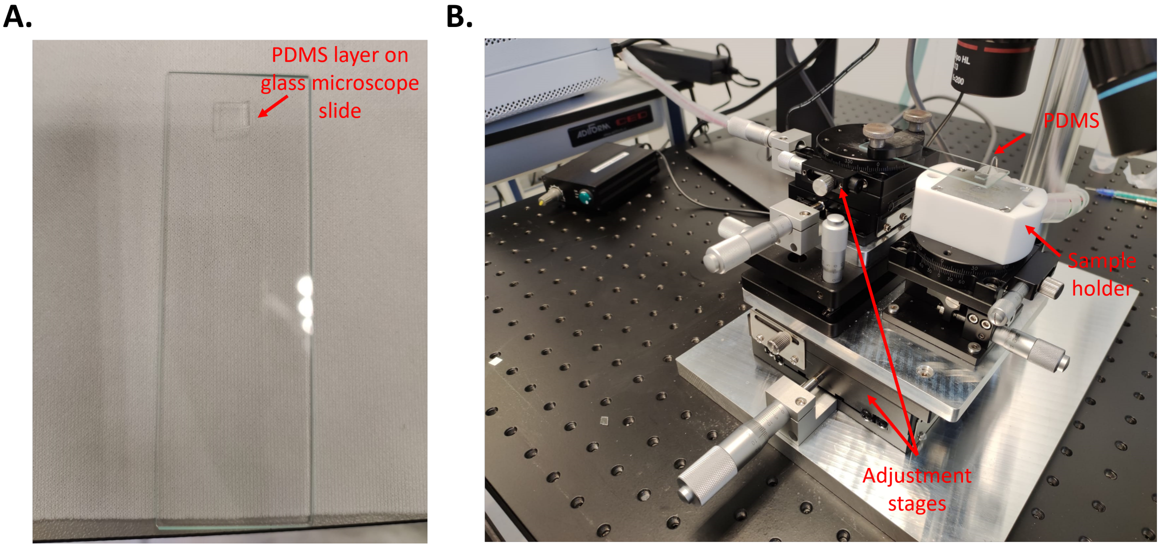

Figure 25: A. PDMS film attached to a glass microscope slide. **B.** Precision stamping setup.

When stamping flakes onto the final substrate, it was found that the flake does not drape onto the micro/nano-structures (cavities and beads), leaving a bubble of air between them. For this reason, we tried to combine this process with the subsequent use of a vacuum chamber and desiccator. The aim is to remove the air in the cavity and help the flake drape onto the shape of the micro/nano-structures and therefore, fully see the effect of the structures on the hBN. However, this step was unsuccessful since after 36 hours of vacuum the air bubbles remained.

4.3 Characterisation of the samples

Once the flake has been deposited onto the micro/nano-structured substrates, the samples can be further characterised. In this subsection, the methodologies and techniques used to characterise the structure and optical properties of the sample are described.

4.3.1 Optical microscopy and Fluorescence imaging

The optical microscope is a type of microscope that magnifies the image of a sample that cannot be perceived with the naked eye by using visible light and a system of lenses [108]. The sample can be analysed in two different ways: with a wide-field imaging exposing the entire sample to the light, or by irradiating a part of the specimen with a fine light beam i.e. confocal microscopy. In this master thesis we use optical microscopy to inspect the state and dimensions of the micro/nano-structures and the flakes, as well as for preparing, transferring and assembling both accurately. Moreover, fluorescence imaging is also required to determine if QEs are present in the sample. Therefore wide-field microscopes will be used for bright field and fluorescence imaging.

In bright field microscopy, white light is condensed and illuminates the sample and produce contrast with it, obtaining a dark image in a bright background as a result [109]. On the other hand, in order to excite solely the QEs, fluorescence imaging uses a light source of a wavelength of interest (LED or laser) as explained in the subsection 2.1. When the fluorescent object is excited, in this case the QE, it absorbs the light and emits a photon of lower energy and consequently at a higher wavelength, which will be detected with a CCD camera system [110]. Unlike the bright field microscope, the contrast is produced by the difference of fluorescence in the specimen. An interesting characteristic, is that both types of microscope can be setup in two different illumination configurations called trans-illumination and epi-illumination [111]. As shown in Figure 26, in the first setup the light is transmitted through the sample and the contrast is generated with the absorption of light in dense areas of the sample. In contrast, with the epi-illumination configuration, the white light that hits the object is reflected off in order to produce contrast.

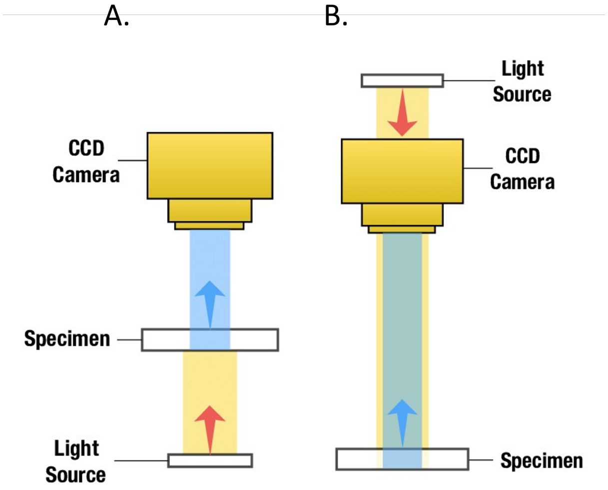

Figure 26: Difference between the microscope configurations: **A.** Trans-illumination. **B.** Epi-illumination. Figure adapted from [111].

In this project, bright field wide-field microscopes will be used, specifically the models Olympus BX60 and VHX-6000. The topography of the samples that cannot be examined with the AFM (due to the limited out of plane range) will be obtained with the model VHX-6000. This is the case for the hBN deposited on top of beads. This optical microscope has a "Depth Composition" option, in which the lowest and highest height point of focus are first manually selected. After that, 200 pictures are automatically taken, with a systematic increasing focus. Then, the information from each picture is automatically extracted by the software of the microscope and a height composition is done.

For fluorescence wide-field microscopy, an inverted epi-fluorescent microscope will be employed, in particular the model Nikon Eclipse Ts2R. The samples in which the substrate is not transparent are placed bottom up, whereas the samples that have a transparent substrate are placed upright. To localise the spots of interest in the sample, white light (trans-illumination) is used. Once the desired flake with its structure are localised, the illumination mode is switched to epi-illumination, and the fluorescence of the sample is examined at 470 nm and 525 nm. During all of this process a water-immersion 60x lens is used.

4.3.2 Scanning Electron Microscopy

A scanning electron microscope, also known as SEM, is an electron microscope that generates images of the specimen by scanning it with a focused beam of electrons [109]. The electrons, which are negatively charged, emitted by the electron source are accelerated towards an anode, which is positively charged. From the anode, these are focused on the sample surface with electromagnetic lenses and then interact with the atoms of the sample, producing signals collected by the electron detector (Figure 27). These signals are caused by two type of electrons: electrons backscattered when interacting with the sample, or low-energy secondary electrons, which first lose energy since they knock out an electron of the sample [23]. The data contains information about the surface topography of the sample and its composition, generating the SEM image. The reason why there is also an X-ray detector (Figure 27), is because the sample can also emit X-rays which can be used for compositional mapping.

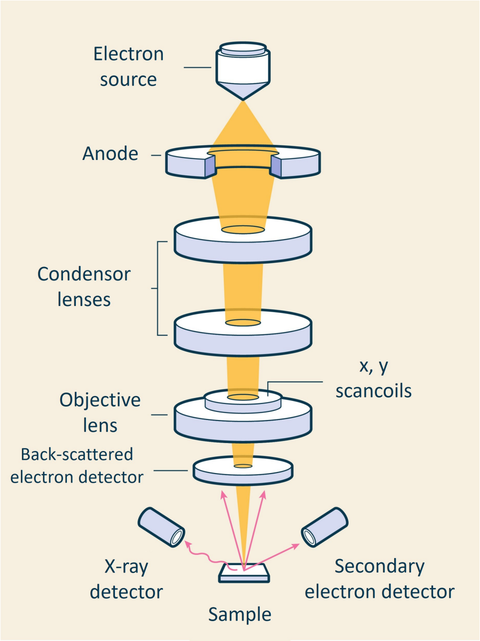

Figure 27: Set up of a typical Scanning Electron Microscope. Figure adapted from [112].

As mentioned, this technique complements the information given by the atomic force microscope, giving a better understanding about the spatial arrangement of the patterned substrates and the deposition of the flake on top of these. The model of SEM that is used in this project is the JEOL 6010LA. The voltage acceleration used in this project varies between 5 kV and 10 kV. Also, the samples are coated with an gold layer during 30 s at 10 mA in order to obtain higher resolution images.

4.3.3 Atomic Force Microscope

Atomic Force Microscopy (AFM) is a technique applied to image and obtain information about the topography of a sample with a nanometer resolution [113]. This is achieved by moving a sharp tip attached to a cantilever close to the surface of the material. The repulsive force between the tip and the surface of the sample elastically deflects the cantilever. This deflection is measured as follows: a laser beam focuses on the cantilever, and is reflected towards a photodetector (Figure 29) [114]. When the cantilever is in its equilibrium position, the reflected laser beam always hits the same position of the position sensitive photodiode. However, when the cantilever bends due to the interaction with the sample surface, the position of the reflected beam shifts on the photodiode. This photodiode converts this change into a corresponding electrical signal [115].

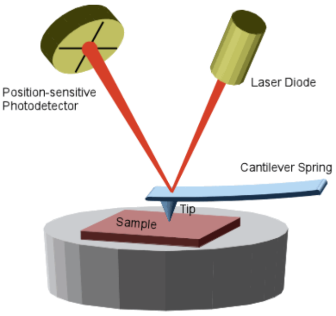

Figure 28: Set up of the atomic force microscope [116].

As seen in Figure 29, there are three possible modes to measure the topography of the surface, based on the interactions between the tip and the surface. In the contact mode, there is a strong repulsive force that bends the beam, since the tip is dragged over the surface of the sample. Even if this probes the sample with a high resolution, it can cause damage to the sample due to penetration of the tip into the object. A less invasive mode is the tapping mode. In this case, the tip oscillates and moves near the surface of the sample at or near its resonance frequency (the AFM feedback loop maintains it constant). Those oscillations lead only to periodic contact of the tip but at the same time the topology is imaged with lower resolution. The non contact mode is the mode with lowest resolution, however, it does not damage the surface of the samples. This is achieved by moving the tip less close to the surface and the image is generated from the force interactions during the scan [117].

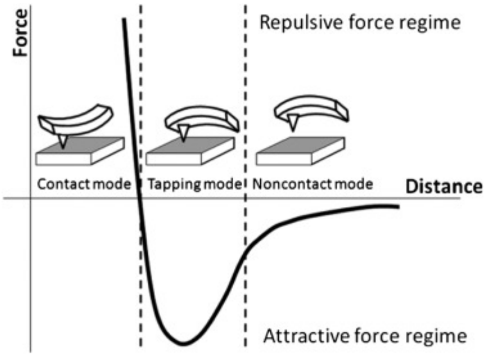

Figure 29: Force versus distance between tip and sample in each AFM mode [117].

In this project, the AFM is used to measure the thickness of the hBN flakes that are stamped on the patterned substrates, as well as establish how well they conform to the substrate features. To avoid the damage of the samples, while having a good resolution we used the tapping mode. The atomic force microscope that has been used in this project is the model Asylum Research Cypher S AFM from Oxford Instruments.

4.3.4 Raman spectroscopy and Strain analysis

Raman spectroscopy is a tool that can determine chemical species by detecting specific interactions of light with the matter and its molecular vibrations [118]. When the light of a laser of wavelength λ_{laser} hits, part of this light is scattered. Most of these photons have their energy unchanged when scattered off ($\lambda_{laser} = \lambda_{scatter}$), a phenomenon called Rayleigh scattering. In this case, an electron absorbs the photon and is temporally excited to a virtual state, since the energy of the photon is not enough to bring the electron to an excited state. When the electron returns to its ground state it emits the photon with the same energy.

The remaining small fraction of photons are scattered inelastically, a phenomenon called Raman scattering. In this type of scattering, photons lose or gain energy due to an exchange of energy with the vibrations of the material. If the photon loses energy, the Raman scattering is called Stokes scattering. For it to happen, the electron that absorbs the photon is found in an initial electronic and vibrational ground state [23]. The photon energy is insufficient to bring the electron to an electronic excited state, which gets excited to a temporary virtual state. When the electron returns to an electronic vibrational ground state, it emits the photon with less energy, and therefore a longer wavelength ($\lambda_{scatter} > \lambda_{laser}$). The phenomena in which the photon gains energy (and therefore is re-emitted at a shorter wavelength) is called anti-Stokes scattering ($\lambda_{laser} > \lambda_{scatter}$). This occurs when the electron that absorbs the photon has an initial electronic ground state and a vibrational excited state. The photon excites the electron to a temporary virtual state, returning back to an electronic and vibrational ground state. This three types of scattering are shown in Figure 30:

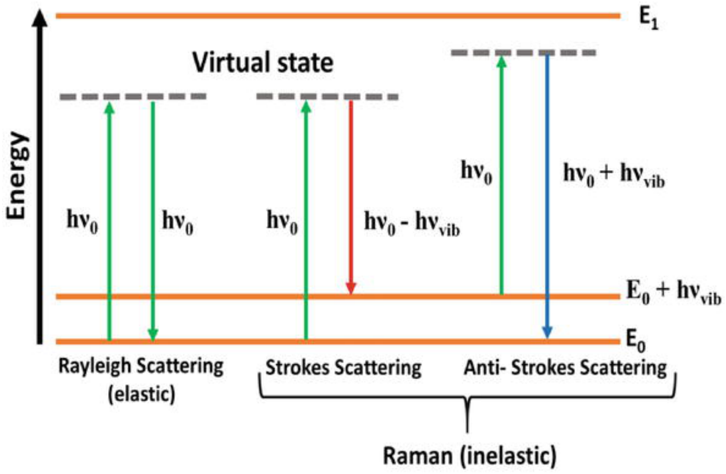

Figure 30: Types of scattering in a molecule excited by a photon which energy $E = h\nu_0$. It should be noted that $\Delta E = h\nu_{vib}$ represents the difference in vibration energy levels [118].

The Raman scattered light contains information about the molecular vibrations (deformability of a bond, i.e. how easily the electrons in the bond are displaced), and by analysing the frequency of the scattered light it is possible to determine the molecular structure and composition of the material [119]. Hexagonal boron nitride presents ultra-low frequency lines at $-52.5\ cm^{-1}$ (anti-Stokes) and $52.5\ cm^{-1}$, and a high frequency line at $1366\ cm^{-1}$. While the first two correspond to the interlayer shear mode (ISM) of hBN, the most intense line located at high frequencies correspond to the in-plane mode (IPM) [120] (Figure 31).

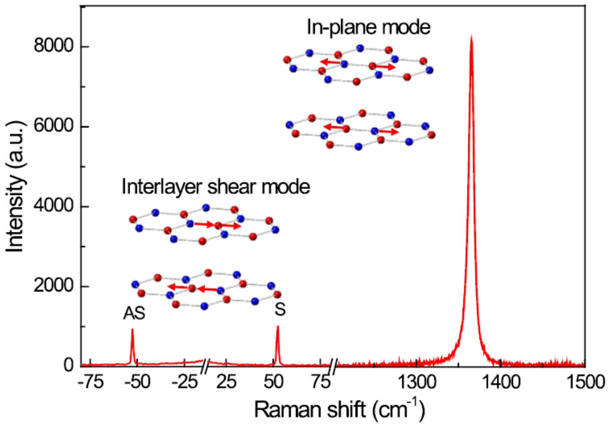

Figure 31: Raman spectrum of bulk hBN [120].

Since we will be working with different thicknesses of hBN, it is also important to know the effect of the thickness on the Raman signature of hBN. The study performed with a $\lambda = 514.5nm$ laser by Gorbachev et al., showed that the intensity of the peak of BN becomes progressively weaker as the number of layers decreases, with the intensity for 3 layers being 10 times higher than for monolayers (Figure 32 A). The hBN Raman shift varies with the numbers of layers as well, approaching its bulk Raman shift as the number of layers increases. In addition, there are variations in the main peak position for mono- and bilayers of BN, while this effect disappears for flakes thicker than 5 layers (Figure 32 B). The authors explain this variation of peak position with appearance of strain in the flake.

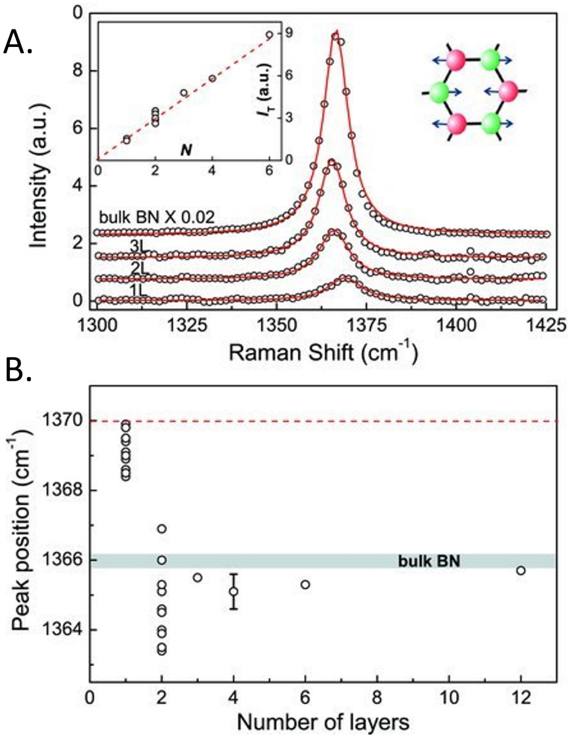

Figure 32: **A.** Raman spectra of atomically thin BN according with number of layers denoted ad L. **B.** Position of the Raman peak for different numbers of layers. In mono- and bilayer samples, the peak position varies by 2 cm^{-1}. The dashed red line corresponds to the predicted Raman shift of the monolayer BN, compared to the bulk BN (gray bar) [121].

During the last years, micro-Raman spectroscopy has become an increasingly popular technique to measure local strain at the microscale level since it provides nondestructive and high spatial resolution measurements [122]. As mentioned in subsection 2.5, the interaction between the incident photons and the molecular vibrations of the compound depends on the shift of the natural frequency of the compound, decreasing with bond stretching (tension) and increasing with compression [123]. Figure 33 shows how the Raman shift is affected when tensile and compressive stress are applied in silica, whose Raman peak is found at 520 cm^{-1}.

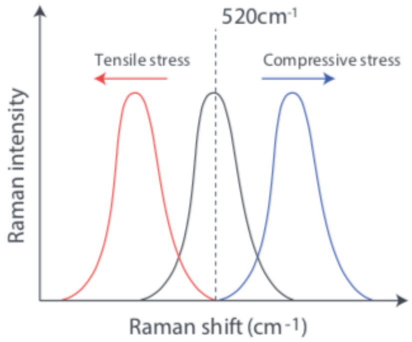

Figure 33: Comparison between the Raman shift of stress free silica (black), silica under tensile stress (red), and silica when compression is applied (blue) [124].

Unfortunately, the effect of strain on the hBN Raman shift has not been systemically studied yet, with only a few Raman studies available in the literature. In the report from Blundo et al., they study the strain on hBN bubbles with Raman spectroscopy at an excitation wavelength of 532 nm. The thickness of the flakes are 55, 10 and 5 nm, reaching with these Raman shifts increments between $24.6 \pm 0.6 cm^{-1}/\%$ and $33.2 \pm 5.2 cm^{-1}/\%$ and strains of 1.9 % [125]. The Raman band shift rate per percentage of strain in this study is dissimilar to the study from Tran et al., explained in subsection 2.6, probably due to a use of a different laser excitation wavelength. Similarly, the optical properties of quantum emitters is also dependant on the applied strain. Mendelson et al. found that after the application of a 3.7 % and 5.55 % of tensile strain to CVD grown hBN, there was a shift of 12.6 nm and 20.8 nm respectively in the emission of two different QE. While in the first case there is a decrease in the broadening of the ZPL once the hBN is strained as seen in Figure 34 (from 21.9 nm to 11.7 nm), the second doubles its peak width after strain application (from 8.1 nm to 16.7 nm). There are no changes in the purity and stability of the quantum emitter after the application of strain.

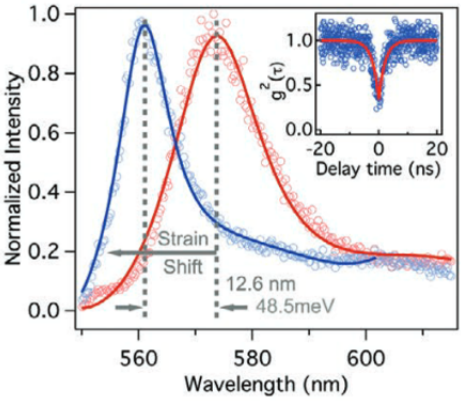

Figure 34: Wavelength emission shift of a QE when a tensile strain of 3.7 % is applied. Its initial wavelength emission is found at $573.40 \pm 0.08 nm$. Inset displays the $g^2(\tau)$ function, confirming the quantum nature of the emission at 0 % strain [80].

If the laser of the Raman spectrometer is powerful enough, it can also perform confocal photoluminescence (PL) measurements [23]. This can excite the quantum emitters of the sample and make them emit PL photons, which are included in the measured Raman spectrum. Therefore, the Raman spectrum contain information of both, Raman and photoluminescence peaks. It should be noted that for photoluminescence measurements, wavelengths units are conventionally used (nm), while Raman measurements are taken in cm^{-1}. The hBN PL peak is found at 553.4 nm, compared to the 1366 cm^{-1} from the Raman measurements.

In this project, we will use Raman spectroscopy to measure the strain of the hBN flakes when they are deposited on the different micro-nanostructures. The specific model used in this thesis is the Renishaw InVia in the Kavli Nanolab Delft, with an Argon ion excitation laser ($\lambda = 514.5\ nm$). The general set up of a micro-Raman spectrometer is the following (Figure 35):

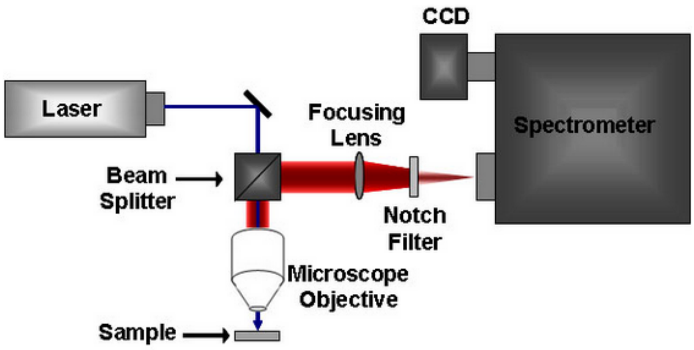

Figure 35: Schematic of a micro-Raman spectrometer. The laser beam illuminates the sample via a microscope objective. The scattered light goes through the beam splitter and a focusing lens, and is redirected and focused on the spectrometer, where the intensity of the light at each wavelength is detected [119].

5 Results and discussion

5.1 Generation of strain with beads

In this experiment, red fluorescent polystyrene beads of 5 μm and 10 μm in diameter were deposited on both silica and glass substrates. Next, the 5 μm beads were put under oxygen plasma for 1 minute at 100% power in order to bleach any possible fluorescence of the beads. Afterwards, hBN flakes were stamped onto the beads, making the samples ready to be analysed.

5.1.1 Optical microscopy

When performing optical microscopy on the flakes draped onto the 5 μm beads (Figure 37), we observe in fluorescence mode that the region where the bead is located together with the hBN flake emits fluorescence (Figure 36). The bead area emits fluorescence at both wavelengths of excitation (470 nm and 525 nm). This could be due to quantum emitters created with strain.

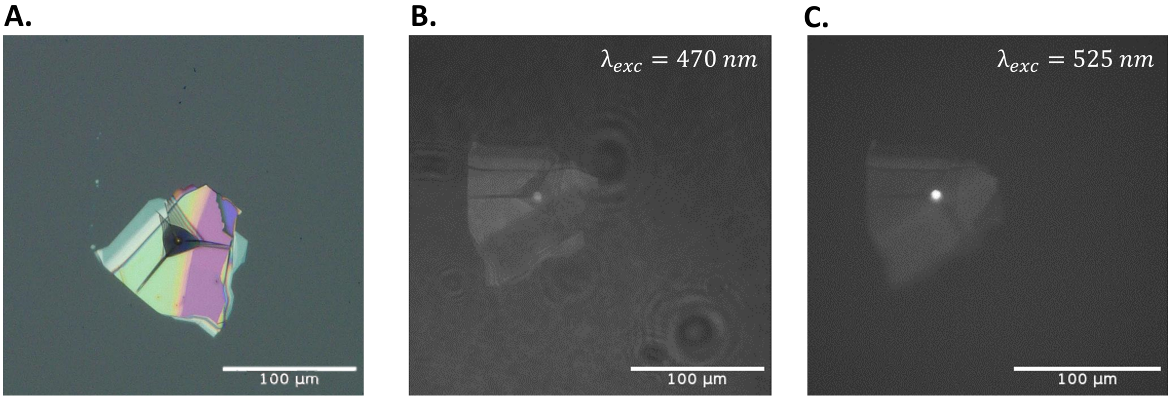

Figure 36: hBN flake (size: 113.70 μm x 114.70 μm) draped on a 5 μm bead deposited on a silica wafer examined with: **A.** Bright-field image. **B.** Fluorescence microscopy taken with the 470 nm filter set with an exposure time of 320 ms and an analog gain of 14. **C.** Fluorescence microscopy taken with the 525 nm filter set with an exposure time of 1 s and an analog gain of 64.

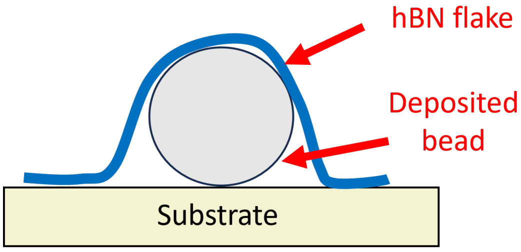

Figure 37: Schematics of the hBN flake deposited onto the bead.

The 5 μm deposited beads are fluorescent at red wavelengths and, in theory, should not fluoresce with green (525 nm) and blue light (470 nm), especially after being treated with oxygen plasma. However, when examining other regions of the SiO_2 substrate, both beads and beads draped by hBN flakes emit fluorescence with equal intensities. This can be observed in Figure 38, where the hBN drapes five different 5 μm beads on the left of the picture, which are as intense as the beads without hBN on the right region of the picture. Therefore, it is improbable that QEs are being generated due to the strain of the hBN when draped on the 5 μm beads.

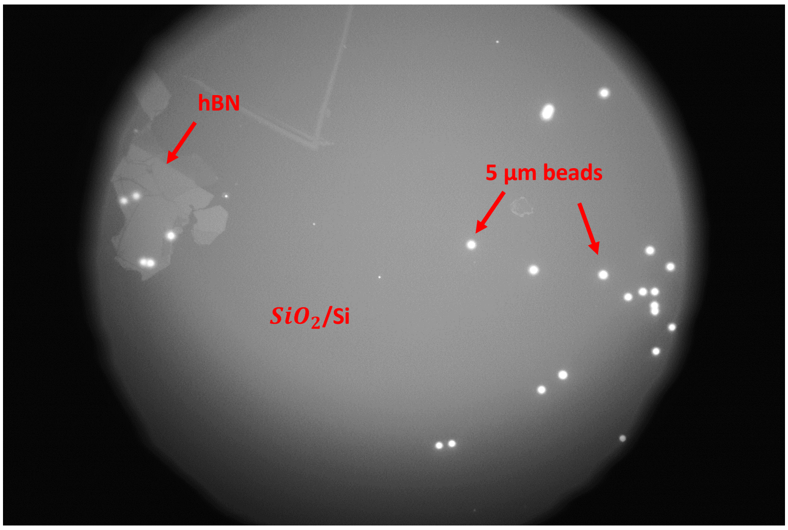

Figure 38: Fluorescence microscopy of an hBN flake draped on five 5 μm beads (left) which are as fluorescent as the beads without hBN (right). The picture was taken with the 525 nm filter set with an exposure time of 1 s and an analog gain of 64.

Similarly, when the 10 μm polystyrene beads were used, the beads appeared to emit fluorescence when excited at both wavelengths. However, in this case we decided to keep investigating one specific sample, seen in Figure 39 A, since the region of the hBN flake in contact with the bead was visibly emitting more fluorescence than the surrounding beads (Figure 39 B and C). This extra emission intensity is interesting to research further because it could suggest that QEs have formed. Specifically the emission was a 17.21 % and 49.39 % higher in both excitation wavelengths (470 nm and 525 nm respectively) (Figure 40). Note that these values were calculated with a pixel brightness measurement in ImageJ.

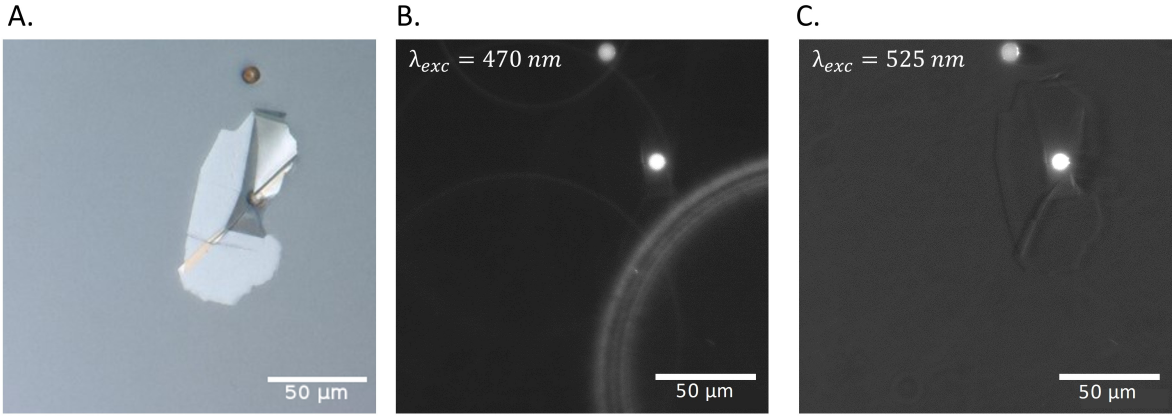

Figure 39: hBN flake (size: 100.61 μm x 34.98 μm) draped on a 10 μm bead deposited on a glass wafer examined with: **A**. Bright-field microscopy. **B.** Fluorescence microscopy taken with the 470 nm filter set with an exposure time of 195 ms and an analog gain of 64. **C.** Fluorescence spectroscopy taken with the 525 nm filter set with an exposure time of 700 ms and an analog gain of 38.

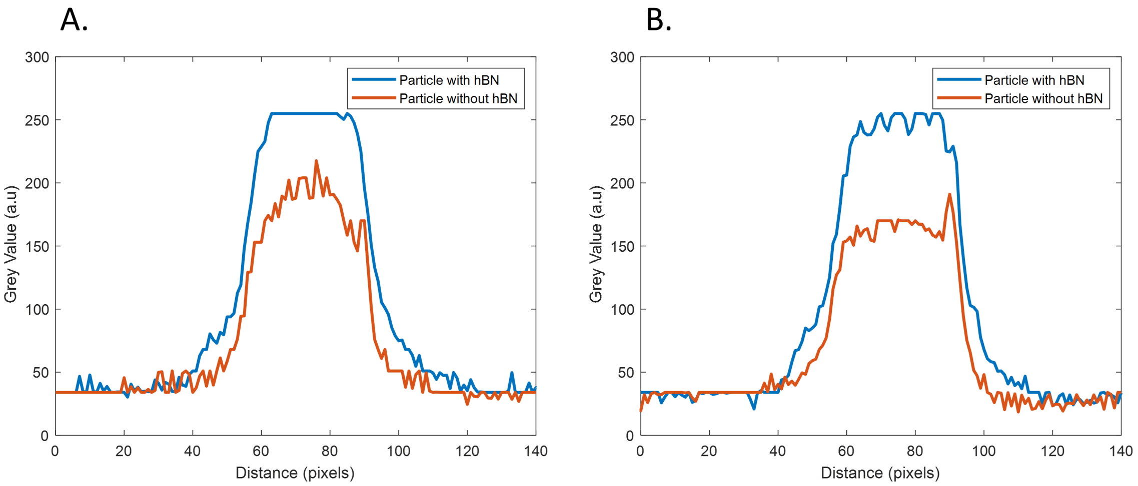

Figure 40: Intensity difference between the $10\mu m$ bead without hBN and the $10\mu m$ with an hBN flake shown in Figure 39 with laser excitation A. at 470 nm and B. at 525 nm.

5.1.2 Photoluminescence imaging and Raman spectroscopy

Photoluminescence (PL) imaging experiments were performed to further investigate the reason for this higher intensity found in the sample illustrated in Figure 39. PL can help us to characterize the nature of this fluorescence. In addition, in order to know if the hBN flake is strained when draped on the $10\mu m$ bead, Raman spectroscopy analysis was done. The simultaneous analysis of both techniques can tell us if the nature of emission are hBN QEs and if they are generated with strain.

For both measurements, the focus point of the Raman spectrometer's microscope lens was on the hBN flake's top surface. In Figure 41 the intensity maps of the scanned area at the typical wavelength and Raman shift of hBN (553.4 nm and 1364.5 cm^{-1} respectively) are shown. It can be observed in both maps that the position of the bead coincides with the region where the hBN intensity is significantly increased. An increase in the intensity of the hBN peak does not necessarily imply the existence of quantum emitters, since as shown in subsection 2.4, these emit photons at a wide range of wavelengths. Nonetheless, the study from Kremarová et al. shows how the QEs of pristine hBN, unmodified or pure hBN that has not been chemically modified or functionalized, emit photons at the same wavelength as pristine hBN increasing only the intensity of the emission peak. Since in this master thesis project we are using pristine hBN, we attribute the emission at 553.4 nm to QE in high quality, unmodified hBN [126].

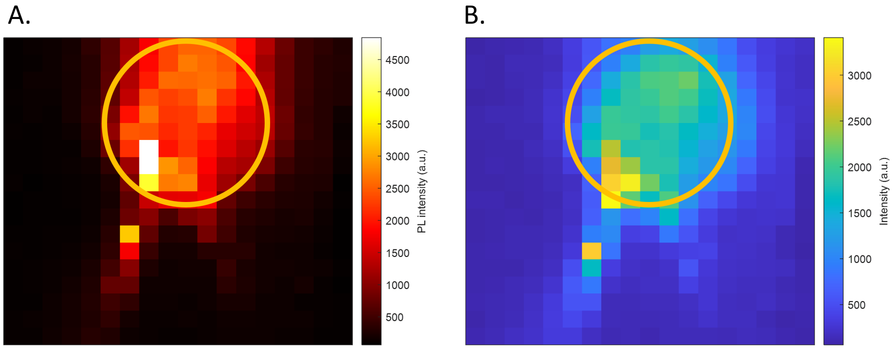

Figure 41: **A.** PL map at 553.4 nm. **B.** Raman spectroscopy map at 1364.5 cm^{-1}. The orange circles on both graphs represent the position of the 10 μm bead.

If two perpendicular lines are traced through the point that has the highest PL intensity and we plot the PL and Raman emission pixel through pixel, Figure 42 is obtained. It should be noted that due to the high the background, the figure has been corrected with a Raman Spectrum Baseline Removal filter. In the figure, we can observe that even if the PL intensity increases significantly in the region where the bead is located, the Raman hBN peaks do not shift, meaning that no appreciable strain is present in the hBN flake due to the bead. Therefore, there is no change on the bond lengths of the hBN and it is unlikely that defects have been able to form. There are also some additional peaks in the horizontal line map, which are probably contamination peaks that have interfered the measurement. The data suggests that either: 1. The bead may also be fluorescent at the same wavelength of the hBN (553.4 nm) and then we are unable to uncouple the signal from hBN and the signal from the bead. 2. The emission of the hBN may be interacting with the bead, resulting in the appearance of the bead's shape at the hBN emission wavelength.

However, a month after obtaining thse first fluorescence microscopy measurements, we decided to repeat the measurements and found that the higher intensity fluorescence emission disappeared (Figure 43). This could be due to a chemical reaction from ambient exposure or an interaction between the hBN flake and the bead surface, leading to changes in the fluorescence properties.

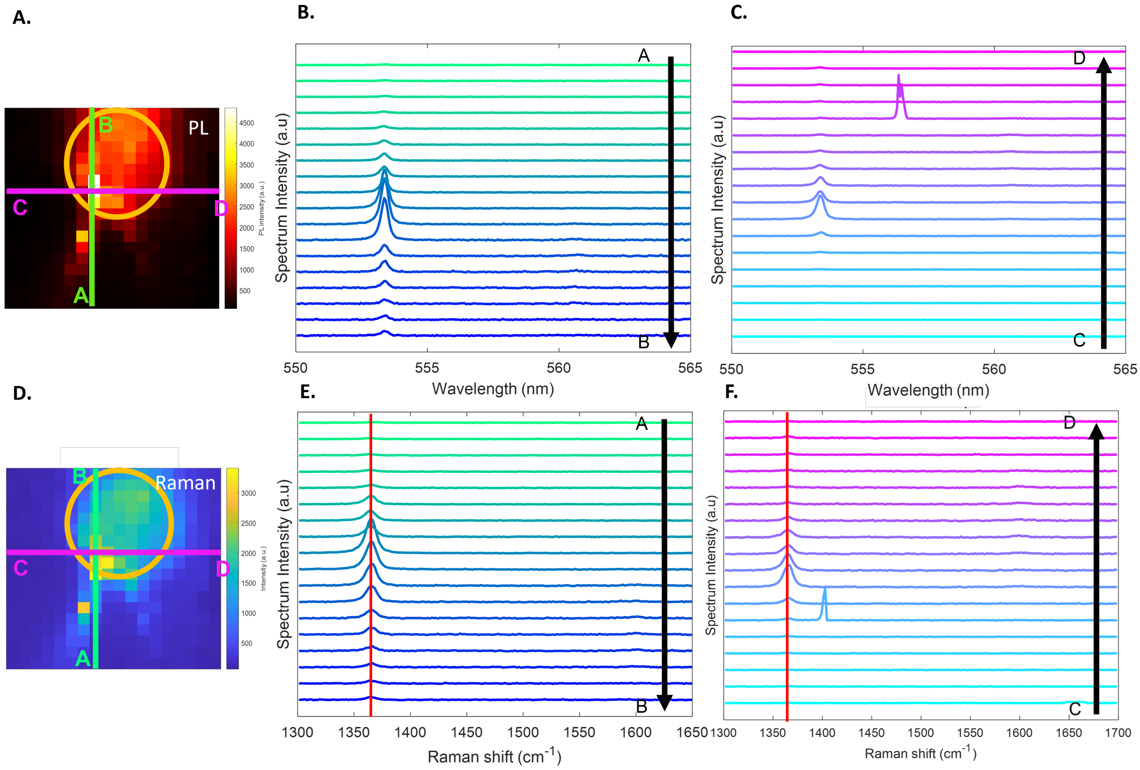

Figure 42: **A.** PL map of the bead region with two perpendicular lines that cross the point with maximum PL intensity **B.** Photoluminescence line maps of the vertical line AB **C.** and of the horizontal line CD (right). **D.** Raman map of the bead region with two perpendicular lines that cross the point with maximum PL intensity **E.** Raman line maps of the vertical line AB **F.** and of the horizontal line CD.

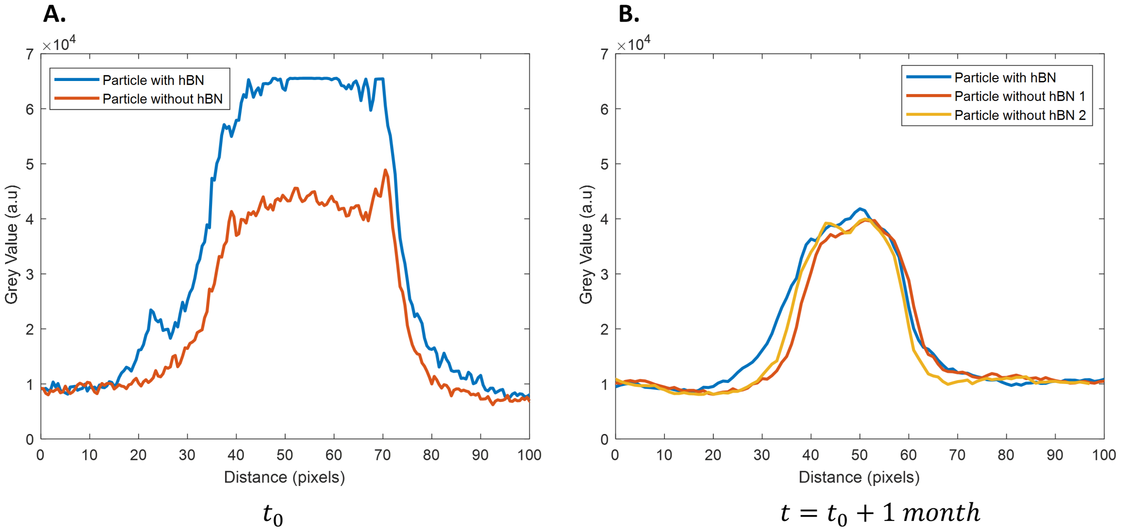

t_0

$t = t_0 + 1\, month$

Figure 43: **A.** Fluorescence emission of the bead with hBN vs bead without hBN at time t_0. **B.** Same measurements repeated after one month.

5.1.3 Topography and strain analysis

In Figure 42 we do not observe a Raman shift graphs indicating that hBN is not strained. One possible explanation is that during the stamping process of the hBN onto the bead, the edges of the flake are not clamped and the bead is not fixed to the substrate making its straining difficult. It can be considered that the hBN flake has been laid on top of the bead without inducing any tension. Therefore, in this case the strain can be considered to be negligible. In addition, in literature 2D materials are typically generated with very localised strains. Therefore, a future suggestion to follow this study is to replace the beads and instead opt for structures with higher aspect ratios and that hBN clamping is considered.

The estimated strain of the hBN flake if it had been clamped to the substrate and the movement of the bead had been restricted can be done FEM analysis. It should be noted that FEA can only do a rough estimation of the strain in this case, since the behaviour of thin 2D materials do not correspond with the continuum equations used by FEA. This method is typically more appropriate for analyzing bulk materials. Being aware of the limitations of this method to determine the strain of our system, the estimated strain is 4.5%. The COMSOL model used to estimate the strain of the hBN flake is found on the .

5.1.4 Summary

We stamped hBN flakes onto 5μm and 10μm polystyrene beads. When performing fluorescence microscopy tests, we realised that the beads of both sizes emitted fluorescence even if they did not have hBN conformed onto them. Also we found an specific bead+hBN sample which emitted a higher fluorescence intensity than the rest. After performing Raman spectroscopy on it, we found that the hBN flake was not strained. It is not clear what caused the fluorescence enhancement, we suspect however, that it might have been a chemical reaction between the hBN flake and the bead surface, changing the fluorescence properties of the bead.

5.2 Generation of strain with femtosecond laser ablated cavities

The generation of cavities with a femtosecond laser was the most reliable method to produce reproducible micro-structures with the smallest features. The diameter used in this thesis is always approximately $\sim 10\ \mu m$. After the ablation in silica and glass substrates, these were sonicated for 5 minutes in acetone and afterwards also 5 minutes in IPA. To further clean the substrates and avoid any possible contaminants, they were cleaned with oxygen plasma for 5 minutes. Next, the hBN flakes were stamped with macromanipulators shown in Figure 25.

5.2.1 First characterisation with optical microscopy

Initially three flakes were stamped on SiO_2/Si. Their fluorescence spectroscopy results show how two out of the three flakes emit fluorescence on the edges of the cavities, as well as on the edges of the flake when excited at a 525 nm wavelength (see Figure 44, Figure 45 and Figure 46). There are two hypotheses that can explain the observed fluorescence: 1. It is possible that there is contamination in the cavities or after the ablation with femtosecond laser some SiO_2/Si may have become fluorescent. 2. The observed emission could potentially be from quantum emitters (QEs) induced by strain. The first case is less likely since the rest of cavities without hBN do not emit fluorescence. In addition, the contamination surrounding the hBN flake possibly comes from the PDMS used to stamp the hBN. However, this contamination is located randomly, which makes it unlikely that it would be located specifically at the edges of two cavities. These results will be complemented with an AFM analysis to determine the cause of this fluorescence emission.

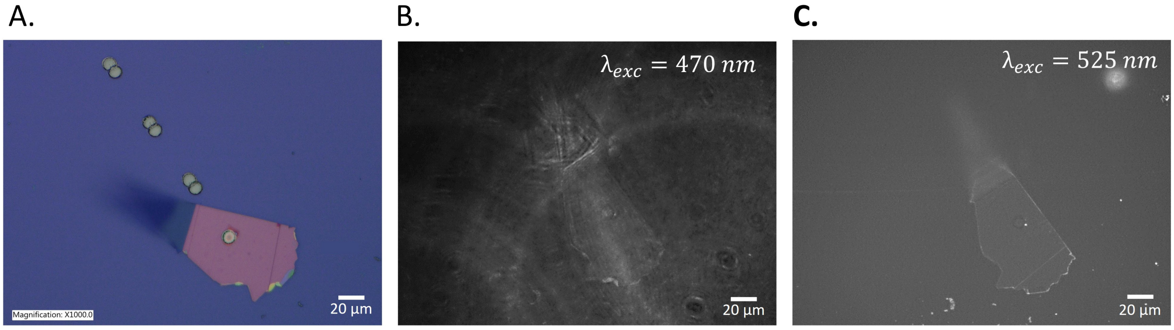

Figure 44: hBN flake (size: 160.87 μm x 53.00 μm) draped on a $\sim$ 10 μm SiO_2/Si cavity ablated with a femtosecond laser (Flake 1): **A**. Bright-field image. **B.** Fluorescence microscopy taken with the 470 nm filter set with an exposure time of 1 s and an analog gain of 17. **C.** Fluorescence microscopy taken with the 525 nm filter set with an exposure time of 4 s and an analog gain of 64.

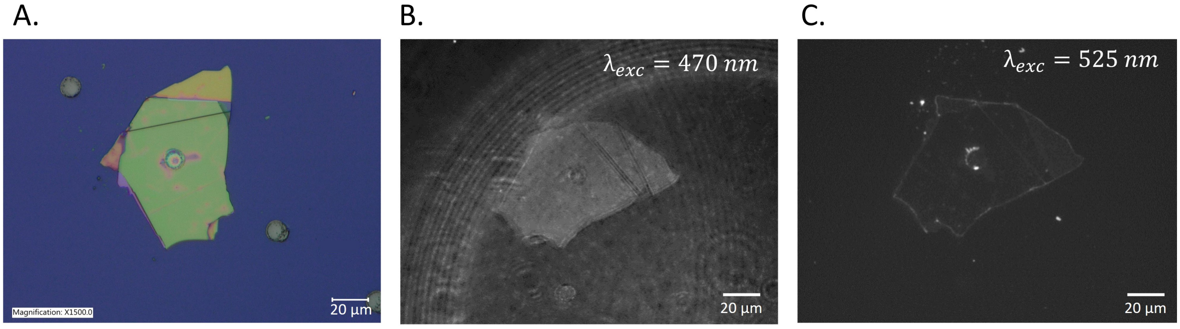

Figure 45: hBN flake (size: 83.02 μm x 68.71 μm) draped on a $\sim$ 10 μm SiO_2/Si cavity ablated with a femtosecond laser (Flake 2): **A**. Bright-field image. **B.** Fluorescence microscopy taken with the 470 nm filter set with an exposure time of 1 s and an analog gain of 20. **C.** Fluorescence microscopy taken with the 525 nm filter set with an exposure time of 3 s and an analog gain of 64.

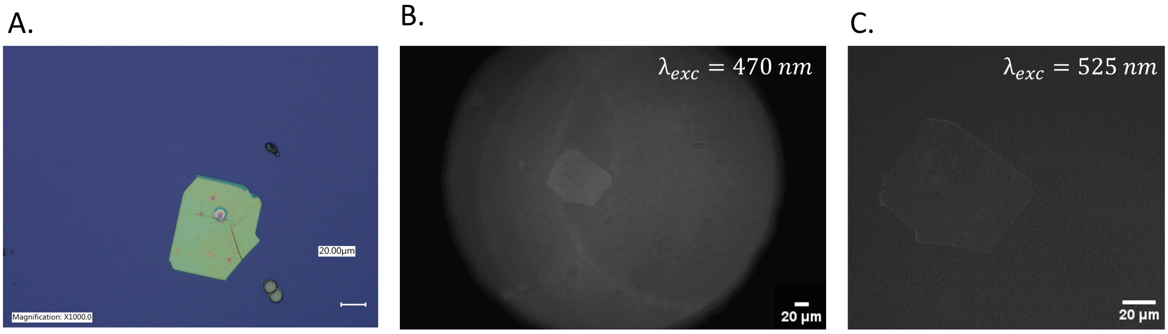

Figure 46: hBN flake (size: 79.99 μm x 70.16 μm) draped on a $\sim$ 10 μm SiO_2/Si cavity ablated with a femtosecond laser (Flake 3): **A**. Bright-field image. **B.** Fluorescence microscopy taken with the 470 nm filter set with an exposure time of 874 ms and an analog gain of 64. **C.** Fluorescence microscopy taken with the 525 nm filter set with an exposure time of 4 s and an analog gain of 64.

In the case of glass cavities, nine flakes of different sizes and thicknesses were stamped onto glass cavities of different diameters (between $\sim$ 8 μm and $\sim$ 17 μm). From these samples, none were fluorescent with green or blue light. Figure Figure 47 illustrates an example of a flake deposited on a glass cavity. These samples will also be analysed with AFM in order to correlate the lack of fluorescence with structural features.

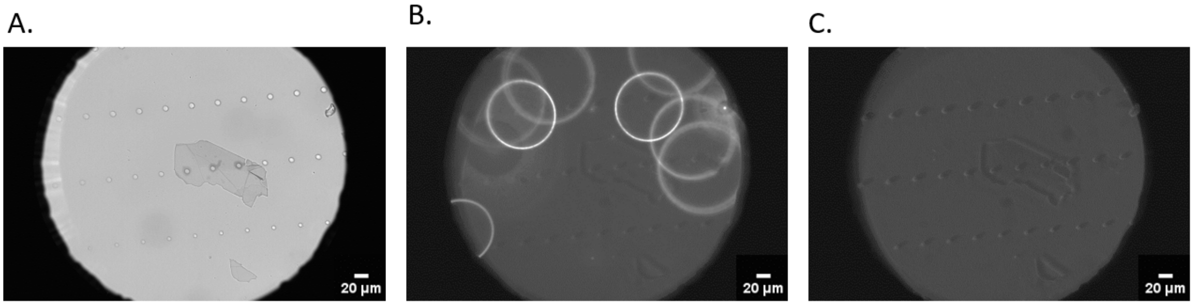

Figure 47: hBN flake (size: 136.88 μm x 53.56 μm) draped on a $\sim$ 8.50 μm glass cavity ablated with a femtosecond laser (Flake 4): **A**. Bright-field image. **B.** Fluorescence spectroscopy taken with the 470 nm filter set with an exposure time of 1 s and an analog gain of 64. **C.** Fluorescence spectroscopy taken with the 525 nm filter set with an exposure time of 1 s and an analog gain of 64.

5.2.2 Topography study

With AFM we were able to accurately determine the thickness of the flakes and how these conformed. The first conclusion that can be drawn is that hBN flakes form a bubble when deposited on both SiO_2/Si and glass substrates. Interestingly, while the flakes that display fluorescence at the edge of the cavities also exhibit noticeable peaks in their topography results (Figure 48 and Figure 49), the ones that lack peaks are not fluorescent (Figure 50 and Figure 51). In the case of Flake 1, the highest peak coincides with the location of the fluorescent emission. In contrast, the highest fluorescent emission in Flake 2 does not coincide with the strained topography of the bubble. However, there is a peak that coincides with the location of fluorescence emission.

In the literature, the formation of bubbles in hBN and the resulting strain generated has been minimally studied. This uniform strain across the bubble can be quantified as $\epsilon = (h/R)^2$, where h is the height of the bubble and R the radius of the bubble [127]. With this analysis, we hypothesize that the strain generated by the bubbles is not sufficient to break molecular bonds and therefore result in fluorescence emission from the hBN. Thus, other factors must be present in order to generate strain profiles that lead to fluorescence.

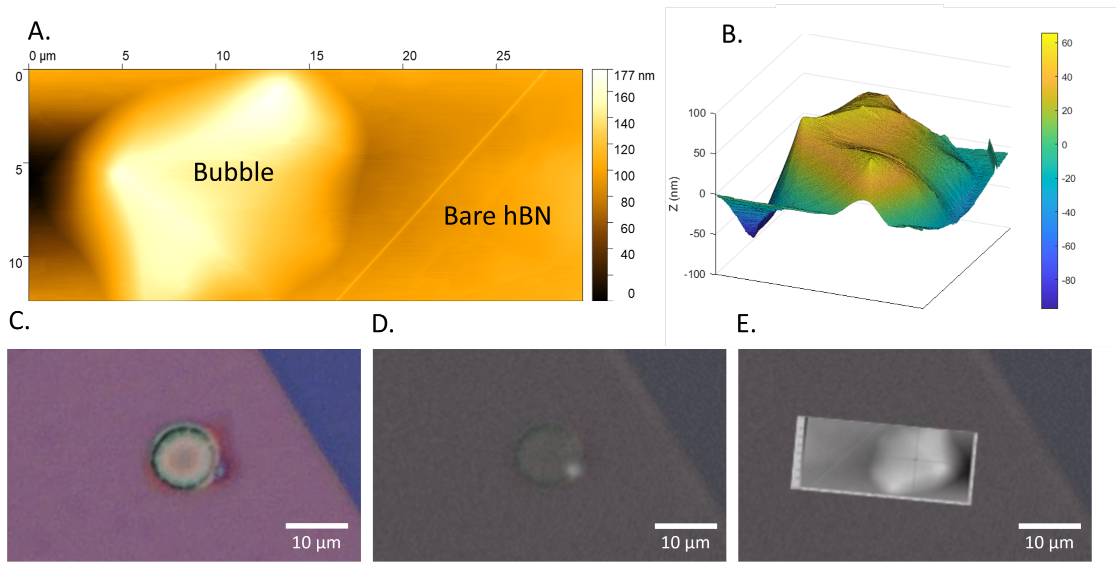

Figure 48: Analysis of Flake 1 (Thickness: 122.56 nm) **A.** 2D topography of the flake deposited onto the SiO_2/Si cavity. **B.** 3D topography of the flake laid creating a bubble onto the SiO_2/Si cavity. Note: two strained peaks appear in the bubble. **C.** Bright-field image of the flake. **D.** Fluorescence image overlapped with the optical image. **E.** 2D topography image overlapped onto fluorescence image. Note that one of the strained peaks correspond with the fluorescence spot in panel D.

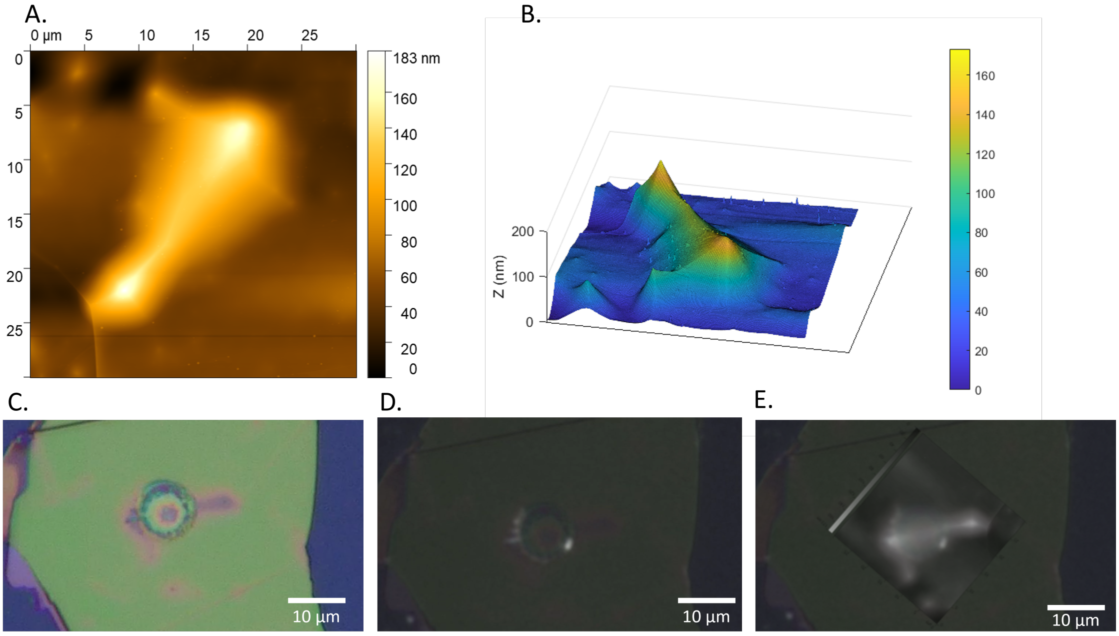

Figure 49: Analysis of Flake 2 (Thickness: 169.63 nm) **A.** 2D topography of the flake deposited onto the SiO_2 cavity. **B.** 3D topography of the flake laid creating a bubble onto the Si_O2 cavity. Note there are three strained peaks in the bubble. **C.** Bright-field image of the flake. **D.** Fluorescence image overlapped with the optical image. **E.** 2D topography image overlapped onto fluorescence image. Note that one of the strained peaks correspond with the fluorescence spot in image D.

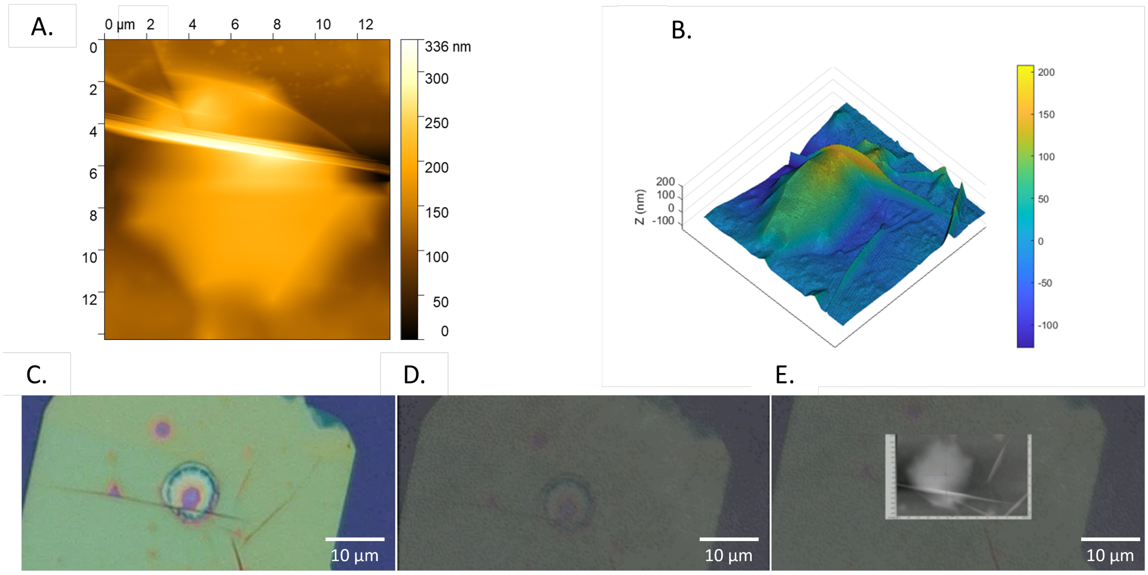

Figure 50: Analysis of Flake 3 (Thickness: 48.6 nm) **A.** 2D topography of the flake deposited onto the SiO_2/Si cavity. **B.** 3D topography of the flake laid creating a bubble onto the SiO_2/Si cavity. Note there are no strained peaks in the bubble. **C.** Bright-field image of the flake. **D.** Fluorescence image overlapped with the optical image. **E.** 2D topography image overlapped onto fluorescence image.

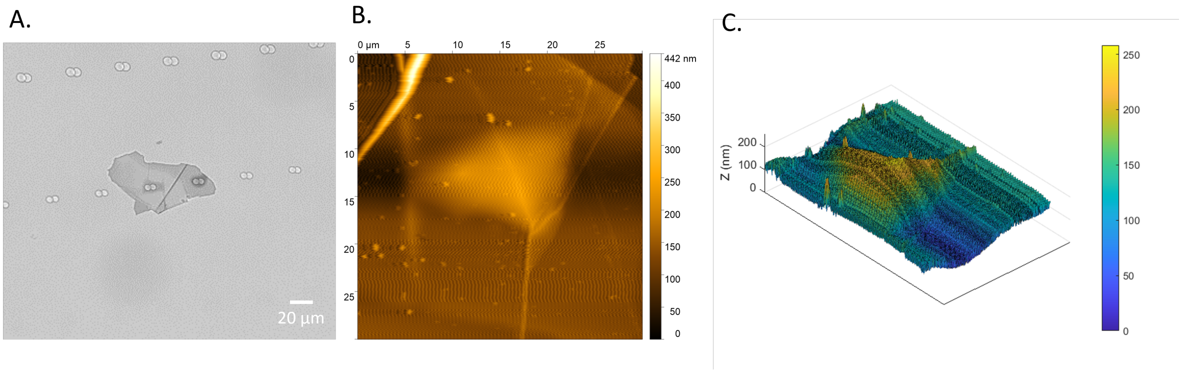

Figure 51: Topography analysis of Flake 5 (Thickness: 44.4 nm) **A.** Optical image of a flake deposited onto glass cavities and non fluorescence emission at 525 nm. **B.** 2D topography of the flake laid creating a bubble onto the glass. Note there are no strained peaks in the bubble. **C.** 3D topography of the flake laid creating a bubble onto the glass cavity.

In order to further analyse what other factors may be influencing the generation of these strain profiles, we decided to study the topography of bare cavities. To do this, we employed the AFM in the case of the SiO_2/Si cavities together with SEM. Only SEM was used for glass cavities because AFM could not accurately detect and scan the surface.

As can be observed in Figure 52 A, on the edges of the SiO_2/Si cavities, as well as in their surroundings, there are material peaks that surpass the height of the plain substrate. These peaks may be created during the ablation of the cavities, generating a recast layer on the edges of the cavity, and moreover depositing material in its surroundings. It is possible that these sharp peaks may touch the hBN flake at certain points and therefore may be the cause of defects of the hBN flakes. In Figure 52 B and C, we observed that inside the cavity there are also protuberances. Aiming to generate more QEs, we tried to remove the hBN bubbles by putting the sample in a vacuum chamber for 36 hours, to make the hBN drape onto the cavity. However, this was unsuccessful. In contrast, the edges of the glass cavities are molten while their centers look very clean (see Figure 53). It is possible that the sharpness of the edges may not be sufficient to produce QEs.

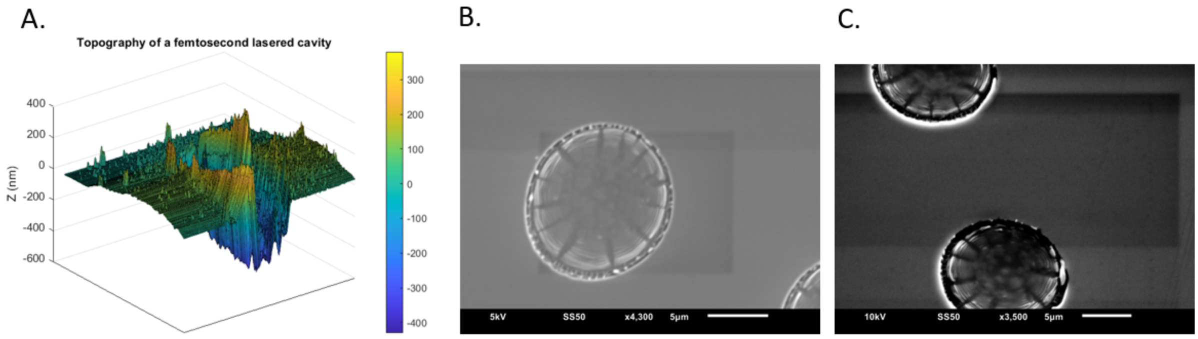

Figure 52: Analysis of SiO_2/Si cavities: **A.** 3D topography of a SiO_2 cavity. SEM of SiO_2 cavities taken: **B.** with plane view **C.** at an angle of 30 °.

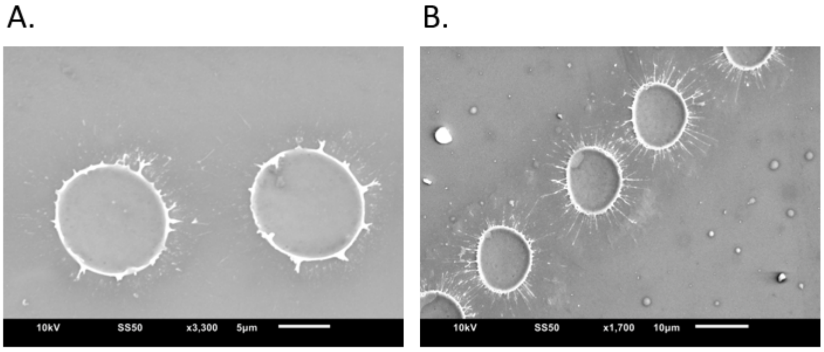

Figure 53: **A** and **B**: Analysis of the topography of glass cavities with SEM imaging.

It is interesting to further study if the geometry of the observed recast layer may be the cause of emission in hBN. To see if the height of this recast layer (deposition material) influences the fluorescence of the hBN, we have generated the following graphs. In these, the fluorescence intensity in the rim of the cavity is compared to its height. As can be seen in Figure 54, the highest peaks (of 80 nm and 102 nm for Flake 1 and 2 respectively) coincide with locations where fluorescence emission occurs. There might be a correlation between height of these peaks and emission of fluorescence, however, the amount of data is too low to give a statistically significant conclusion. The procedure to obtain these plots can be found in Appendix A.

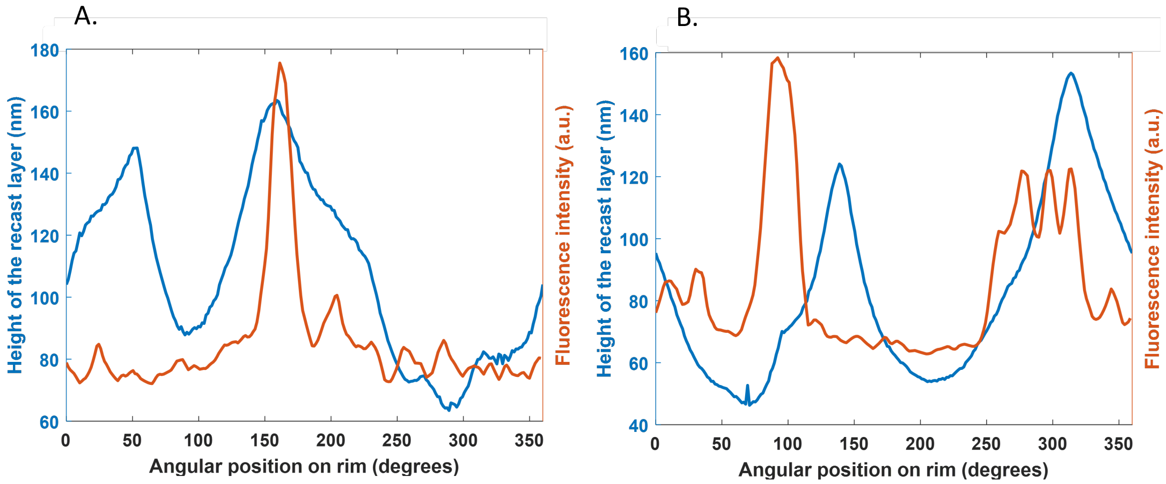

Figure 54: Height of the bubble and fluorescence emission as a function of position along the rim for: **A.** Flake 1 and **B.** Flake 2.

After obtaining these results, more flakes were stamped on SiO_2 substrates to investigate the reproducibility of this method and to verify the correlation between height and fluorescence. Out of the ten new flakes that were stamped, none of them was emitting fluorescence. With this amount of samples (13 in total), there is a wide range of thicknesses of flakes, and substantial variation in the geometry of the recast layer of the cavities. It is reasonable to hypothesize that thinner flakes more easily conform to the shape of these deposited material peaks more easily. For this reason, we wanted to include these factors to our study and see how they may affect the fluorescence of hBN. These have been summarised as: i) thickness of the flake, ii) height of the possible deposition peaks and iii) their curvature (sharpness) and see if there is a correlation between these and fluorescence emission. We hypothesize that a greater height, a sharper curvature, and reduced thickness could facilitate strain generation.

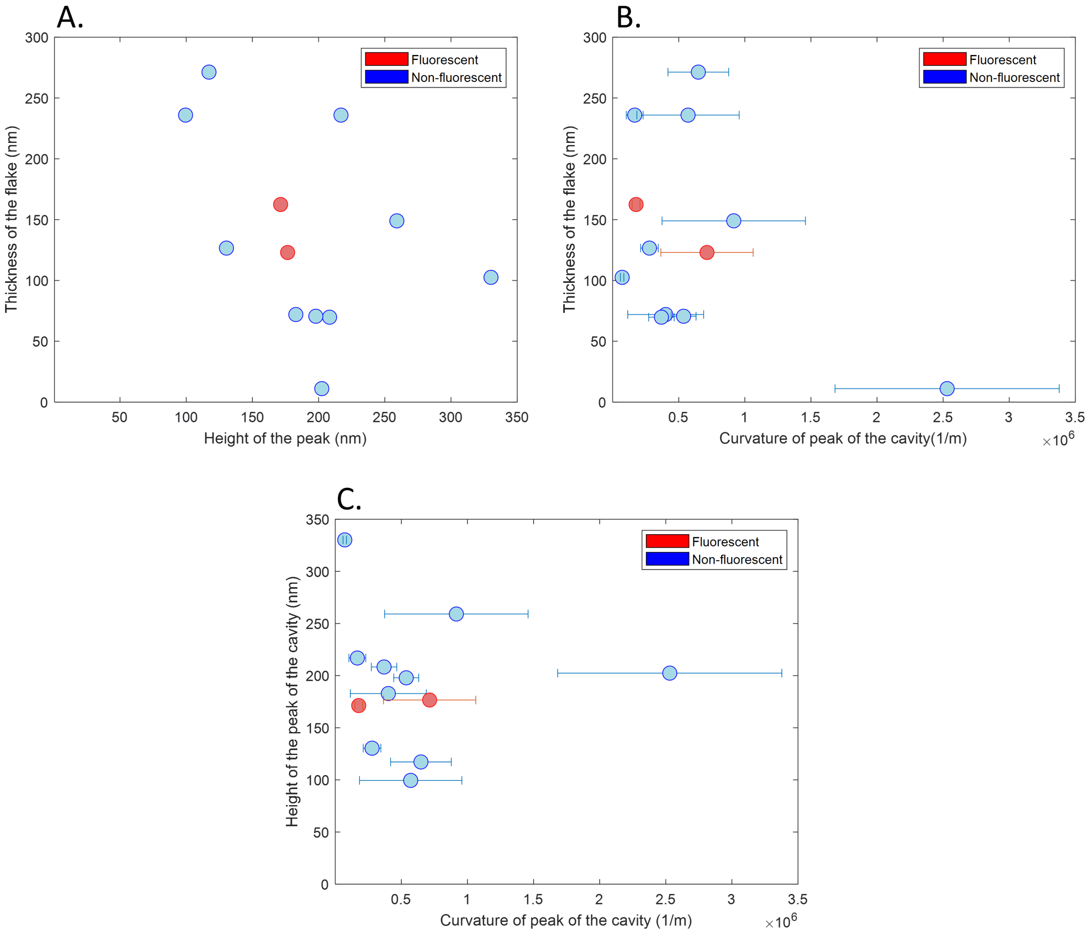

Figure 55: Correlation between: **A.** Thickness of the hBN flake and height of the possible recast layer peak. **B.** Thickness of the flake and curvature of the peak of the recast layer. **C.** Height and curvature of the peak of the recast layer that touches the hBN flake.

As can be observed in Figure 55, none of the three graphs shows any evidence that height and curvature of the recast layer peaks or the thickness of the flake influence the generation of fluorescence in hBN flakes. These factors most likely have an influence on the generation of QEs, however other unknown factors that are difficult to discern with the obtained results should be considered like stamping force or surface adhesion.

5.2.3 Photoluminescence imaging and Raman spectroscopy

To characterize potential QEs and quantify the amount of strain with which they have been generated, we have performed PL and Raman experiments. We decided to focus for this study on the understanding of Flake 1 because of its simplicity (it consists only on a single emission point).

In Figure 56, the location of the potential quantum emitter appears less intense than the center of the cavity and the flat hBN at the edge of the map. These results cast doubt on whether the fluorescent point is a QE or merely contamination. To gain more insight we studied the spot to determine it's temporal photophysical properties.

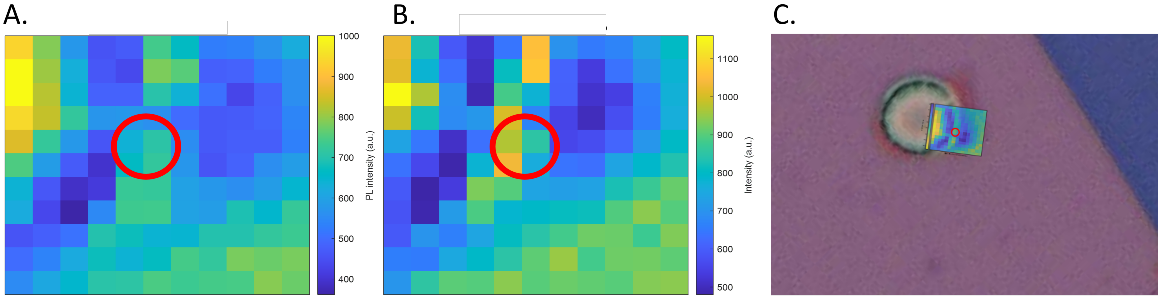

Figure 56: **A.** PL map at 553.4 nm of the region where the QE is located in Flake 1. The red circle represents the location where the QE emits fluorescence. **B.** Raman map at 1364.5 cm^{-1} of the region where the QE is located in Flake 1. The red circle represents the location where the QE emits fluorescence. **C.** Location of the PL map with respect with the optical image of Flake 1.

The strain of the fluorescent spot was also analysed with Raman spectroscopy. A first test was done by analysing the Raman shift of two single spots - one at the fluorescent spot and the other at a location nearby. It should be noted that the intensity of the spots had to be normalised for the sake of comparison. This first test (Figure 57 A) shows how there is a shift to the left of 1.81 cm^{-1} which means that tensile strain is present. As mentioned previously, the literature indicates that there is an 11 cm^{-1} shift per percentage of strain, meaning that in this case the generated strain reaches a 0.17 %.

Afterwards, a Raman line map was taken across the fluorescent spot, starting near the center of the bubble and finishing on the flat hBN (Figure 57 B). The results show that near the center of the bubble and on the flat hBN the Raman shift remains the same as in literature (1364.5 cm^{-1}), while near the rim of the cavity the hBN changes its strain, varying between (1362.65 cm^{-1}) and 1364.5 cm^{-1}). At the highest point of the rim, where a secondary bubble is visually formed and the fluorescent spot seems to appear, the Raman shift corresponds to a 1360.84 cm^{-1}.

The reports that study the correlation between Raman shift and strain are performed at 488 nm and 532 nm. However, this measurement has been performed at 514 nm. The Raman shift is given by the difference between the excitation wavelength and the wavelength of the scattered light. When the excitation wavelength changes, the energy of the incident photons changes as well. As a result, the Raman shift observed in the scattered light will vary with the excitation wavelength. Therefore, with the data available in literature we cannot determine the generated strain with certainty. If we make an approximation of the generated strain by using the results obtained in the 532 nm laser excitation report, a tensile Raman shift of 3.63 cm^{-1} is present, corresponding to a tensile strain between 0.11 % and a 0.15 %. This supports the hypothesis that the fluorescence spot is a QE produced under strain.

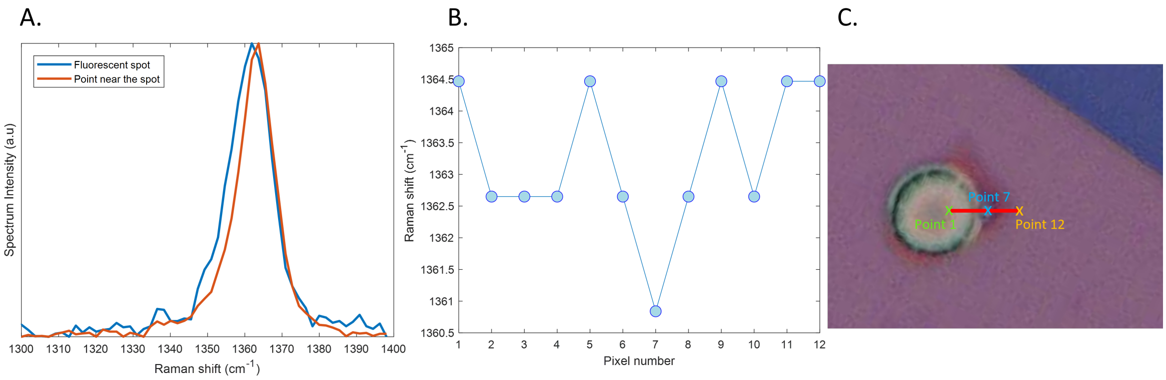

Figure 57: Strain analysis of the fluorescent spot. **A.** first test by analysing two single spots: one at the fluorescent spot (1361.88 cm^{-1}), one at a point surrounding the fluorescent spot (1363.69 cm^{-1}). **C.** A Raman line map was taken across the fluorescent spot (Pixel 1) near the center of the bubble and Pixel 12 the flat hBN. **B.** In the graph it can be seen for each pixel where is the hBN peak located being the minimum Raman shift 1360.84 cm^{-1} and the maximum Raman shift 1364.47 cm^{-1}.

5.2.4 QEs characterization with fluorescence microscopy

As mentioned, the dynamic behaviour of the fluorescent spot were examined in order to obtain further conclusions. In this test, a high resolution epi-fluorescence microscope was used (model Nikon-Ti2). This fluorescence microscope has the capability to examine the samples at a red wavelength (640 nm), green light (532 nm) and blue light (473 nm). The dynamic behaviour test will consist on recording the fluorescence emission of the cavity area for an specific amount of time with each wavelength. Figure 58 B shows the configuration of the flake during the test. It should be noted that at this point of the experimental process, Flake 1 folded on itself as shown in Figure 58 A. The region of the cavity and the fluorescent spot were not affected.

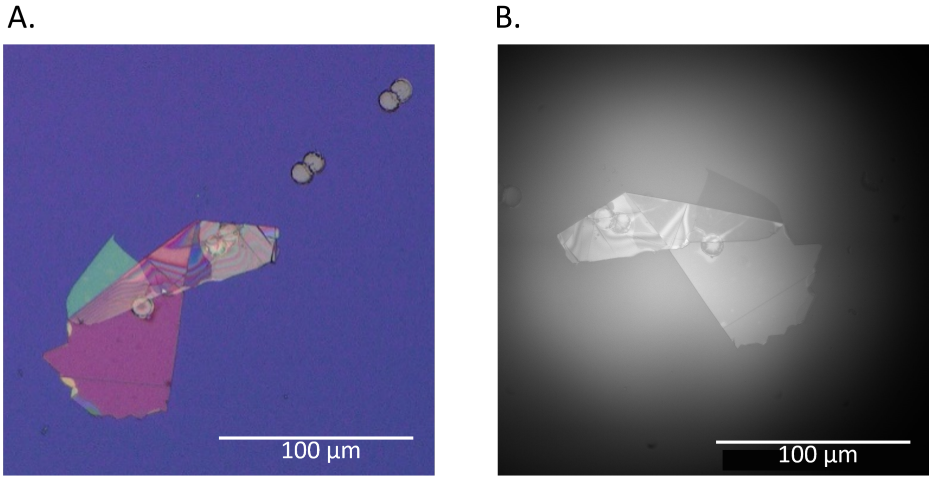

Figure 58: **A.** Optical image of the new state of Flake 1 after folding on itself. **B.** Configuration of Flake 1 during the dynamic behaviour test (White light image with Nikon-Ti2).

640 nm wavelength (Red light)

In Figure 59 B and C three fluorescent spots become visible when the hBN flake is excited with red light. These are likely QEs emitted by hBN instead of contamination, since they only appear in locations where hBN is strained: 2 of them appear at the rim of the cavity, and 1 appears at the wrinkled edge. If the emission was caused by contamination, we would expect to see a larger number of emitting sites dispersed across the entire hBN flake.

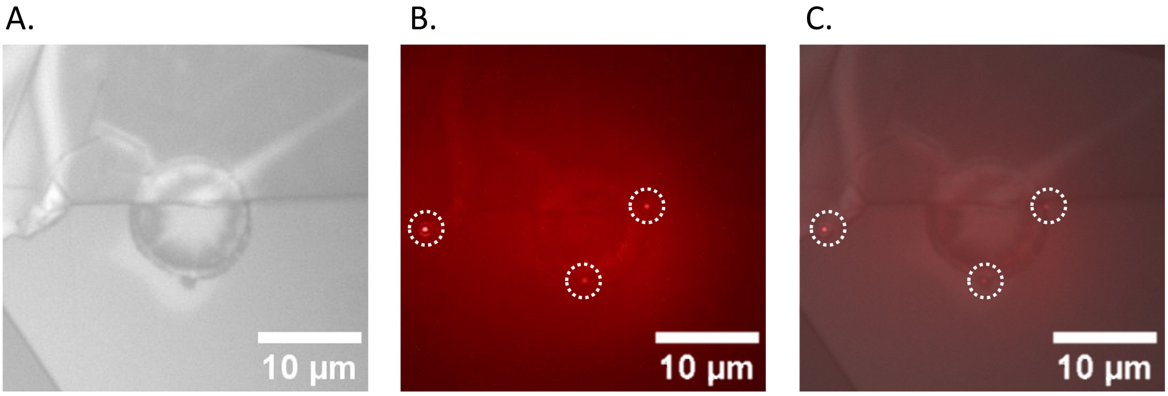

Figure 59: **A.** White light image of the cavity region of Flake 1. **B.** Average red light image of the cavity region of Flake 1. Three fluorescent spots are present. **C.** Overlap between white image and red image. Two out of the three fluorescent spots are found at the rim of the cavity.

The dynamic behaviour of these probable QEs was studied during 30 seconds at a rate of 1 frame per second. We specified three different Regions Of Interest (ROIs) (Figure 59 A) using ImageJ, and quantified their emission frame by frame over those 30 seconds. This quantification has been processed and normalised in MATLAB and finally illustrated as change of intensity of each QE as a function of time. QE2 and QE3 are less bright than QE1 and these have a low rate of change of intensity (between a 2.68 % 9.65 % of change of intensity). On the other side, QE3 is a 30.6 % brighter on average but presents less stability changing its intensity between a 0.65 % and a 38 %. These percentages are determined by calculating the difference of intensity during the minimum and maximum intensity changes. It should be noted that for all experiments the standard deviation of these signals have been compared to the standard deviation of the background signal, in order to verify that the change of signal is due to the blinking of the QE and not because of noise during the measurement. At all times the standard deviation of the QEs is at least 10 times higher than the background signal.

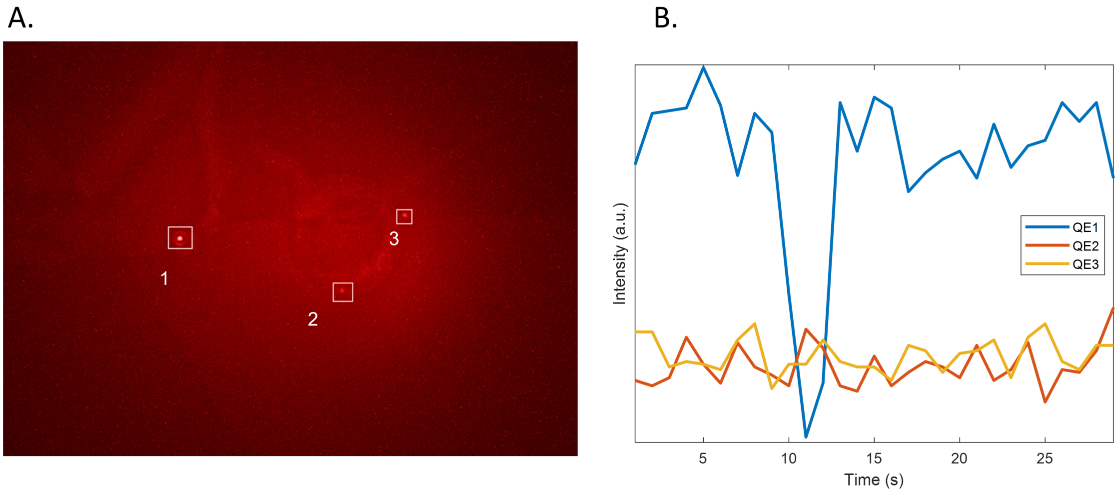

Figure 60: Change of intensity of the three QEs vs time when excited with red light (30 seconds). **A.** Regions Of Interest (ROIs) in which the change of intensity with time has been studied. **B.** Graph that shows the change of intensity of each ROI with time. The intensity on each video frame was obtained with ImageJ and afterwards was normalised in MATLAB.

532 nm wavelength (Green light)

In Figure 61 we can verify further that the fluorescent spots around the edges of the flake and cavities are probably emitted by hBN, since at the left of the flake we can see big fluorescent spots at a very high intensity. Those are most probably contamination, giving a reference on how we should recognise it, specifically as concentrated fluorescent spots of very high brightness.

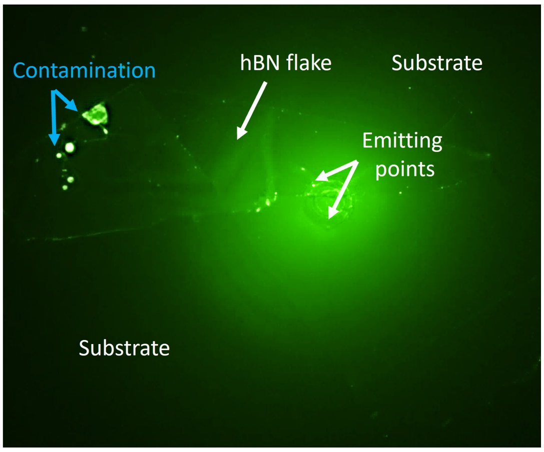

Figure 61: Fluorescent image of Flake 1 when excited with green light (532 nm). Some QEs can be observed at the edges of the flake, and some contamination (maximum intensity spots) can be seen at the folded part of the flake.

When we zoom in on the cavity (Figure 62 A) we can see how there are two fluorescent spots at the rim of the cavity. Interestingly QE4 is a 64.12 % more intense than QE2, but QE2 it is the only one that can be observed under the lower resolution fluorescence microscope (with LED illumination) (Figure 62 B). We hypothesized that this may have occurred due to the folding of the hBN. Nevertheless, we checked afterwards with the first fluorescence microscope, and we could not find QE4. Our hypothesis is that it may be a matter of the poor dynamic range from the other fluorescence microscope. Also, it is important to mention that QE1 has a considerable temporal stability, its intensity ranging between 1.36 % and 11.56 %. QE2 has a negligible intensity, and is clearly visible only for 4 seconds when its intensity rises to 19.59 %. This could be the reason it was not observed during PL mapping test (also performed with green light), because it is latent and emits an intense fluorescent emission once every few minutes, while the acquisition time of the PL test is set to 10 seconds.

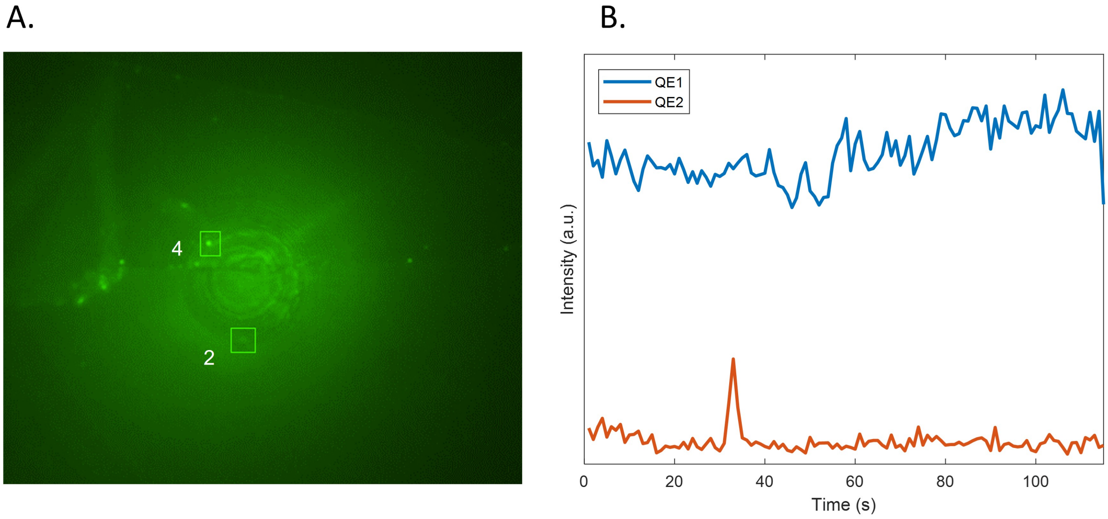

Figure 62: Change of intensity of the two QEs vs time when excited with green light (120 seconds). **A.** Regions Of Interest (ROIs) in which the change of intensity with time has been studied. **B.** Graph that shows the change of intensity of each ROI with time. The intensity on each video frame was obtained with ImageJ and afterwards was normalised in MATLAB.

To determine the time response of QE2, we filmed the fluorescence emission of Flake 1 for another 5 minutes. During this second test QE4 also started showing blinking, appearing only on 3 occasions for a few seconds during those 5 minutes. In the case of QE2, it appears in frame 210, 229, 238 and 251. This was recorded at one frame per second, which means that there are non-emission intervals of 9/9/3 seconds and only emits fluorescence for 1 second in between those intervals. The lack of emission of QE4 in this second test indicates that maybe we have temporally photo-bleached both QEs during the tests. We think that maybe the same is occurring during the PL mapping test, as it is also performed with green light (514 nm). This phenomenon can be seen clearly in Figure 63, where the intensity in both emitters remains low the majority of the time, and emit fluorescence sporadically.

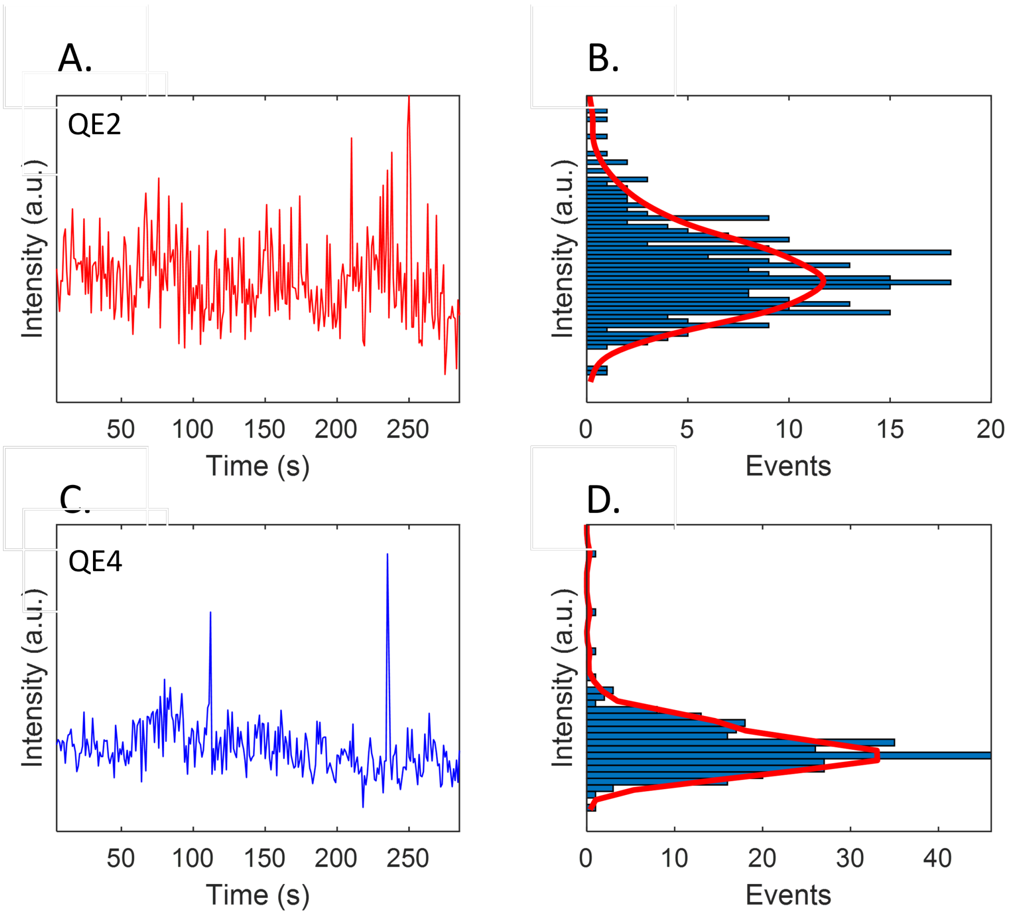

Figure 63: Test of fluorescence emission during 5 minutes at 532 nm. **A.** Change of intensity with time of QE2. **B.** Intensity histogram of the data shown in Figure A. **C.** Change of intensity with time of QE4. **D.** Intensity histogram of the data shown in Figure C.

437 nm wavelength (Blue light)

The excitation of Flake 1 with blue light was overall unstable. During the five minutes test, a large amount of fluorescent spots would emit photons for a second and photo-bleach for the remainder of measurement. This can be seen in Figure 64, where three different frames of the recording (A, B and C) capture the sporadic fluorescent emission spots located within the hBN bubble and its rim. This leads to a new hypothesis: The uniform strain of the bubble may be also sufficient to generate hBN emission, particularly when excited with blue light. This however should be further studied in the future.

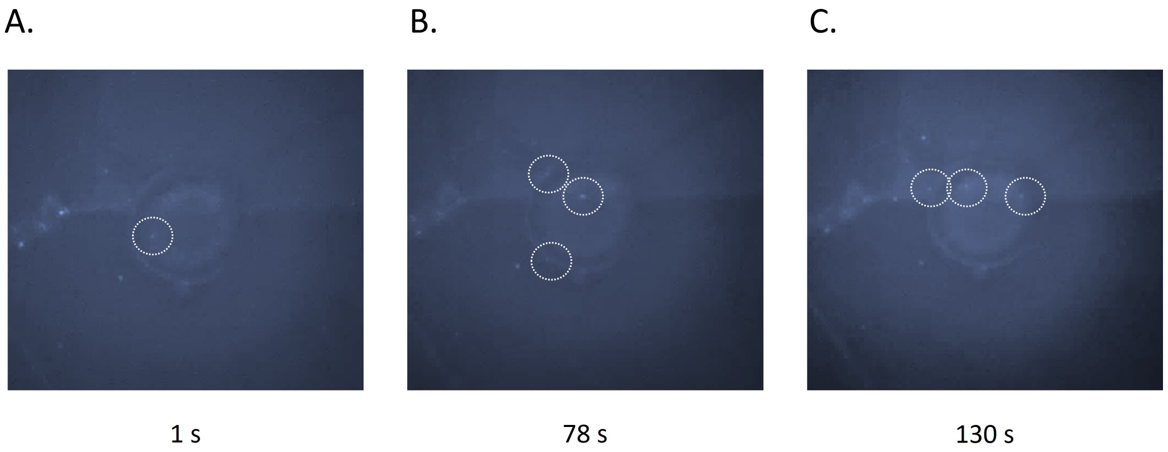

Figure 64: Difference of fluorescent emission location vs time. **A.** QE appearing at the lower-left side inside the hBN bubble. **B.** Two QEs appearing at the rim of the cavity and a third QE located at the edge of the hBN flake. **C.** Two QEs located at the rim of the cavity, and a third QE located at the upper left side region inside the bubble.

The QEs that were further studied as a function of time are shown in Figure 65. This time, the fluorescent spot seen since the beginning of the experimental process (QE2) appears to be more stable compared to illumination under green light. It has a low change of intensity (maximum change corresponds to a 8.58 %), even though it gradually loses intensity over time (specifically a 33.43 %). The second fluorescent emission that has been studied corresponds to a point located outside the cavity region (QE5). This possible QE experiences a greater photoblinking throughout the duration of the study, although its intensity becomes constant after an initial drop of its intensity (73.55%).

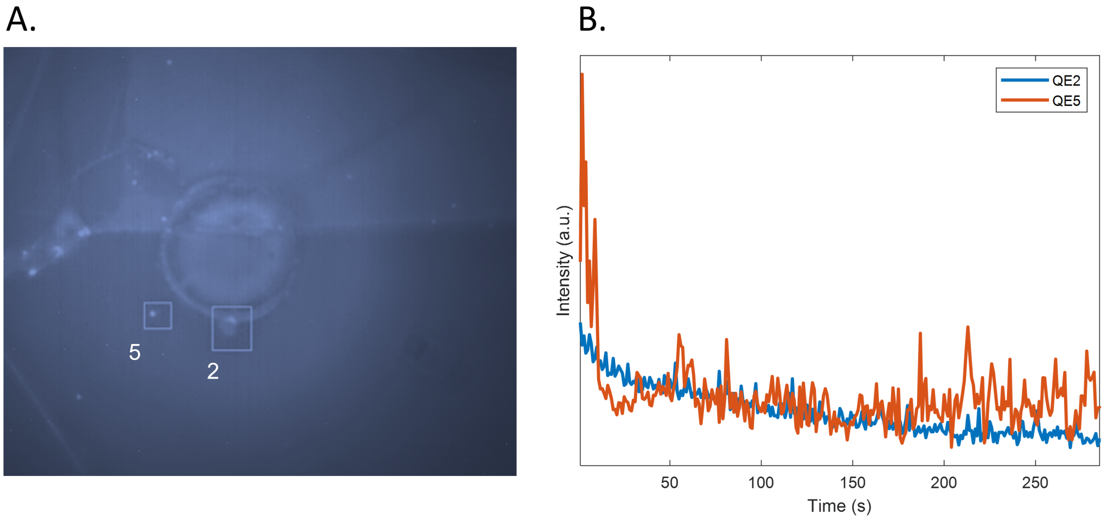

Figure 65: Change of intensity of the two QEs vs time when excited with blue light (300 seconds). **A.** Regions Of Interest (ROIs) in which the change of intensity with time has been studied. **B.** Graph that shows the change of intensity of each ROI with time. The intensity on each video frame was obtained with ImageJ and afterwards was normalised in MATLAB.

We can calculate the fluorescence lifetime of QE2 and QE5, i.e. the average decay time of the excited state of a fluorescence molecule, by fitting the obtained curves with exponential decay equations. The decay of intensity overtime can be expressed with the following exponential decay equation, where I is the intensity at time t, I_0 is the initial intensity, and τ is the lifetime of the fluorescence molecule [128]:

$$I = I_0 e^{\frac{-t}{\tau}} \tag{2}$$

The fitted curves with their equations can be seen in Figure 66. The coefficients of the fitted curves have been obtained with a 95 % of confidence. The fitted curves correspond to the sum of two exponential decay functions with two different fluorescence lifetimes. We only consider the faster decay rate $-1/\tau$ since it is the one that contributes to a drop of the intensity. Therefore, the fluorescence lifetime of QE2 and QE5 is 6.57 s and 44.17 s respectively. These results are different than the ones found in literature (1-3 s). This might be because in the literature the quantum emitters are strictly single photon emitters (SPEs).

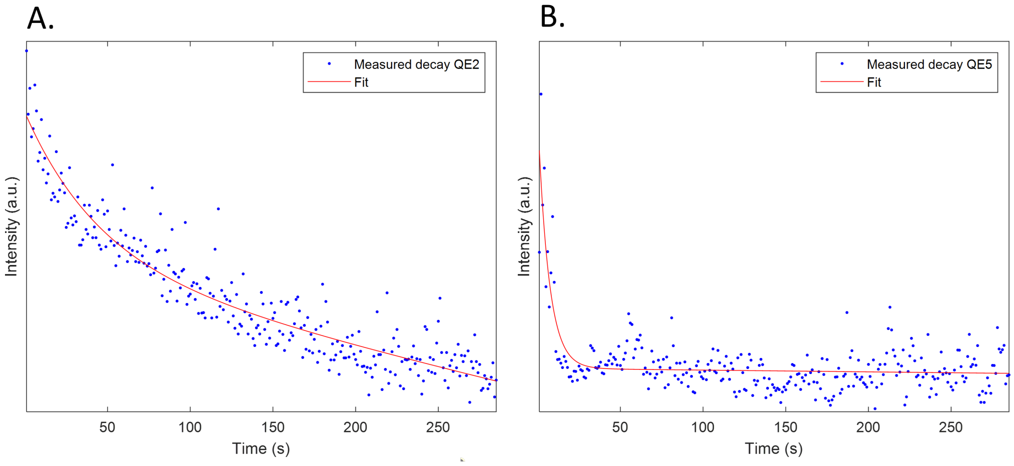

$$I = I_{01} e^{\frac{-t}{\tau_1}} + I_{02} e^{\frac{-t}{\tau_2}}$$

$$I_{01} = 359.1, -\frac{1}{\tau_1} = -0.02264 \frac{1}{s}$$

$$I_{02} = 2868, -\frac{1}{\tau_2} = -3.795x10^{-4} \frac{1}{s}$$

$$I = I_{01} e^{\frac{-t}{\tau_1}} + I_{02} e^{\frac{-t}{\tau_2}}$$

$$I_{01} = 2055, -\frac{1}{\tau_1} = -0.1522 \frac{1}{s}$$

$$I_{02} = 2852, -\frac{1}{\tau_2} = -5.052x10^{-5} \frac{1}{s}$$

Figure 66: Fitted decay curve of the measured intensity decay over time of **A.** QE2 and **B.** QE5.

5.2.5 Summary

After stamping hBN flakes onto SiO_2/Si and glass femtosecond laser ablated cavities, fluorescence emission appeared at the edges of the cavity in 2/3 SiO_2/Si samples, while no emission could be found in glass samples. With a topography study, it was found that the hBN flakes conform into the cavities with the generation of bubbles. Moreover, the fluorescent SiO_2/Si samples presented peaks in these bubbles that coincide with the points of fluorescence emission. By studying the topography of bare cavities, it appeared that these peaks could be caused by the recast layer formed during the femtosecond laser ablation of SiO_2/Si. However, no clear correlation could be extracted between fluorescence emission and the features of the recast layer (height and curvature) and the hBN flake (thickness).

When performing PL and Raman tests in the ROI of Flake 1 at 514 nm, the presence of a Raman shift confirmed that the fluorescent region was strained, even though the PL results did not show an intense emission that indicated the existence of QEs. The cause of these results were explained with fluorescence microscopy, by examining the temporal photophysical properties of the region. In this study, QEs excited with a similar wavelength than the PL and Raman test (532 nm), had sporadic fluorescent emissions being latent most of the time. With other excitation wavelengths however, QEs emitted fluorescence constantly, and we were able to observe photoblinking (red light) and photobleaching (blue light) behaviours. In the case of blue light, several sporadic fluorescent spots appeared within the bubble and its rim.

5.3 Generation of strain with CD and Blu-ray micro/nanostructures

After the direct transfer of hBN flakes via mechanical exfoliation, the samples were ready to be examined.

5.3.1 Optical Microscopy

Figure 67 A and Figure 68 A show that the result of the mechanical exfoliation on the CD is cleaner than in the Blu-ray, where a considerable amount of tape residue is found. The fluorescence images of both the CD and Blu-ray when excited with green and blue light, show that the substrates emit fluorescence (Figure 67 and Figure 68 B, C). Regarding the hBN flakes, these seem to be visually more fluorescent when laid onto the Blu-ray rather than when transferred onto the CD, although this could be caused due to the combination between transparency of the hBN flake and the fluorescence of the Blu-ray disk.

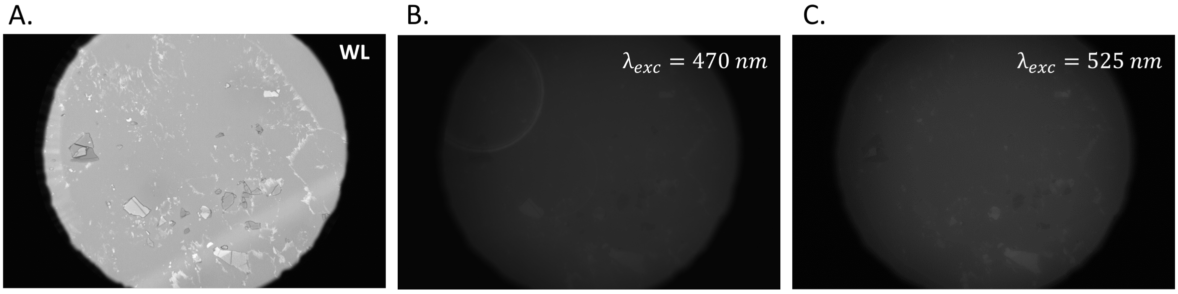

Figure 67: hBN flakes mechanically exfoliated on a Blu-ray disk: **A**. White light image. **B.** Fluorescence microscopy taken with the 470 nm filter set with an exposure time of 119 ms and an analog gain of 19. **C.** Fluorescence microscopy taken with the 525 nm filter set with an exposure time of 1 s and an analog gain of 38.

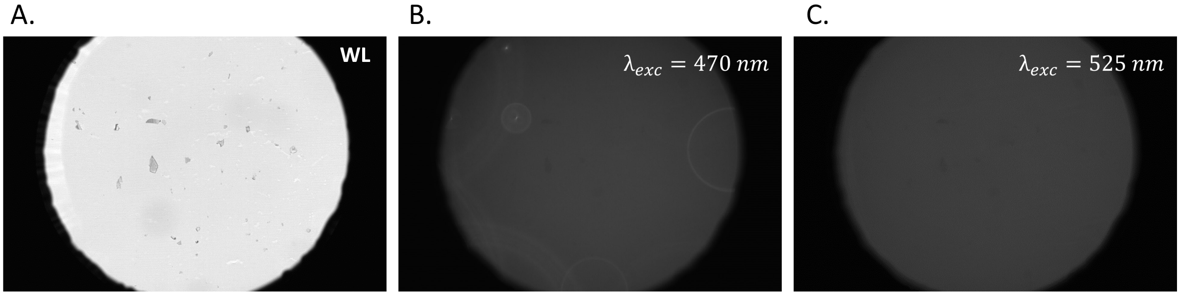

Figure 68: hBN flakes mechanically exfoliated on a CD: **A**. White light image. **B.** Fluorescence microscopy taken with the 470 nm filter set with an exposure time of 119 ms and an analog gain of 19. **C.** Fluorescence microscopy taken with the 525 nm filter set with an exposure time of 1 s and an analog gain of 38.

5.3.2 Topography study

In Figure 69 the AFM images of micro/nanostructures present in a CD are shown. These are between $\sim 80\ nm$ and $\sim 92\ nm$ in height and the pitch is $1.51\ \mu m$. The Blu-ray structures are as periodic as the CD structures, but the Blu-ray disk display a high amount protuberances at its surface (Figure 70). Its structure is formed by holes that range between 20.5 and 50 nm in height. These also have different shapes and sizes, including the tablet shaped holes of a size of $\sim 875\ nm\ x\ 315\ nm$, and the circular shaped holes of $\sim 315\ nm$ of diameter.

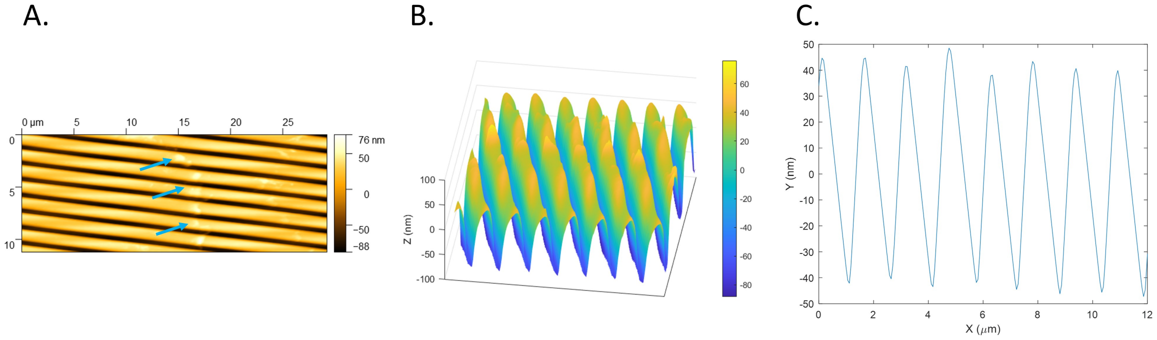

Figure 69: **A.** AFM image of the 2D topography of the polycarbonate layer of a commercial CD. **B.** 3D topography of the polycarbonate layer of a commercial CD. Note that the protuberances in the structure are tape from the mechanical exfoliation (blue arrows). **B.** Height profile of the CD.

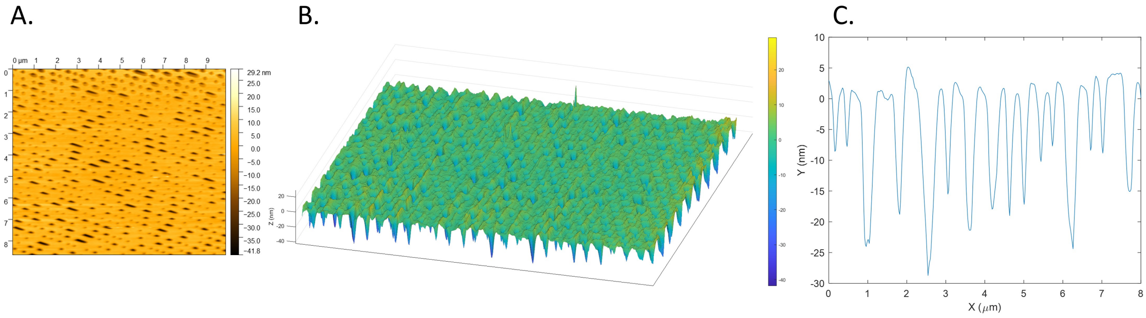

Figure 70: **A.** AFM image of the 2D topography of the silver layer of a Blu-ray disk. **B.** 3D topography of the silver layer of a Blu-ray disk. **C.** Height profile of the Blu-ray.

When hBN flakes are directly transferred to these surfaces, the protuberances of the Blu-ray have the ability to influence the conformity of the hBN flake, independently of its size and thickness. However, this conformation is difficult to perceive in Figure 71 A and B since the tip of the AFM became dirty. This was caused by the glue of the tape, which stuck onto the surface during the mechanical exfoliation process. When the hBN flake becomes thinner, several bubbles are formed due to the protuberances of the surface (Figure 71 C).

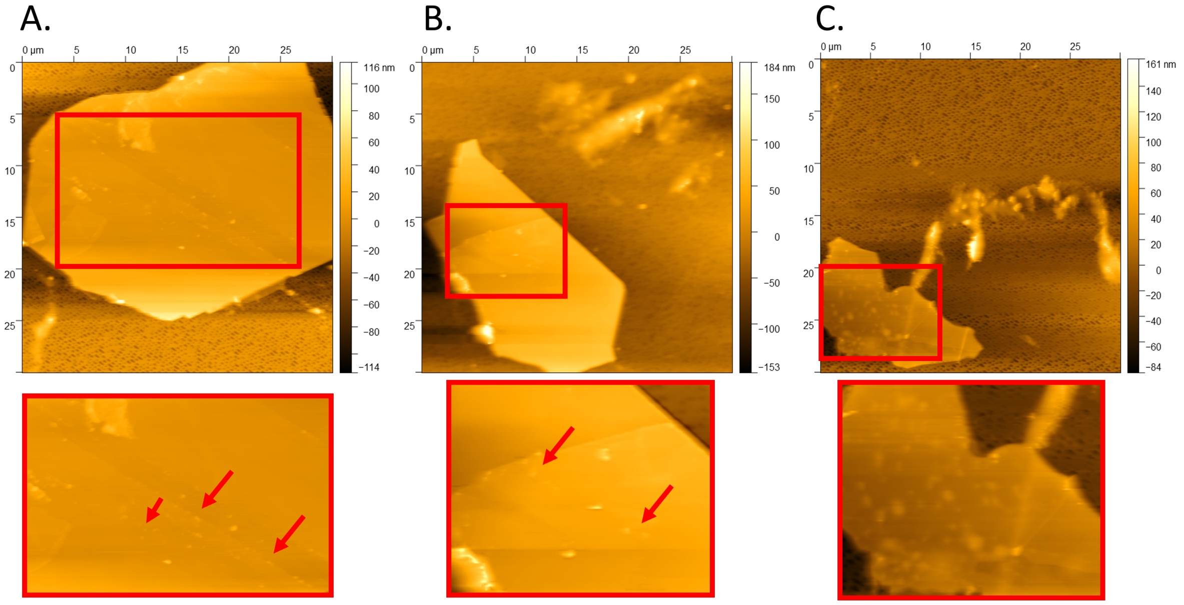

Thickness: 77.5 nm
Size: 31.85 x 22.06 um

Thickness: 114 nm
Size: 25.34 x 11.35 um

Thickness: 51 nm
Size: 17 x 8.05 um

Figure 71: 2D topography of hBN flakes that are exfoliated onto the Blu-ray disk. In all samples, independently from their size and thickness, the structure of the Blu-ray disk influences the topography of the hBN flakes, shown with red arrows.

When the hBN flakes exfoliated onto the CD structures the generated profiles are different. After examining 19 different flakes (Figure 72), we observe how some of them drape around the structures onto the CD while the majority of them is unaffected by the underlying structure.

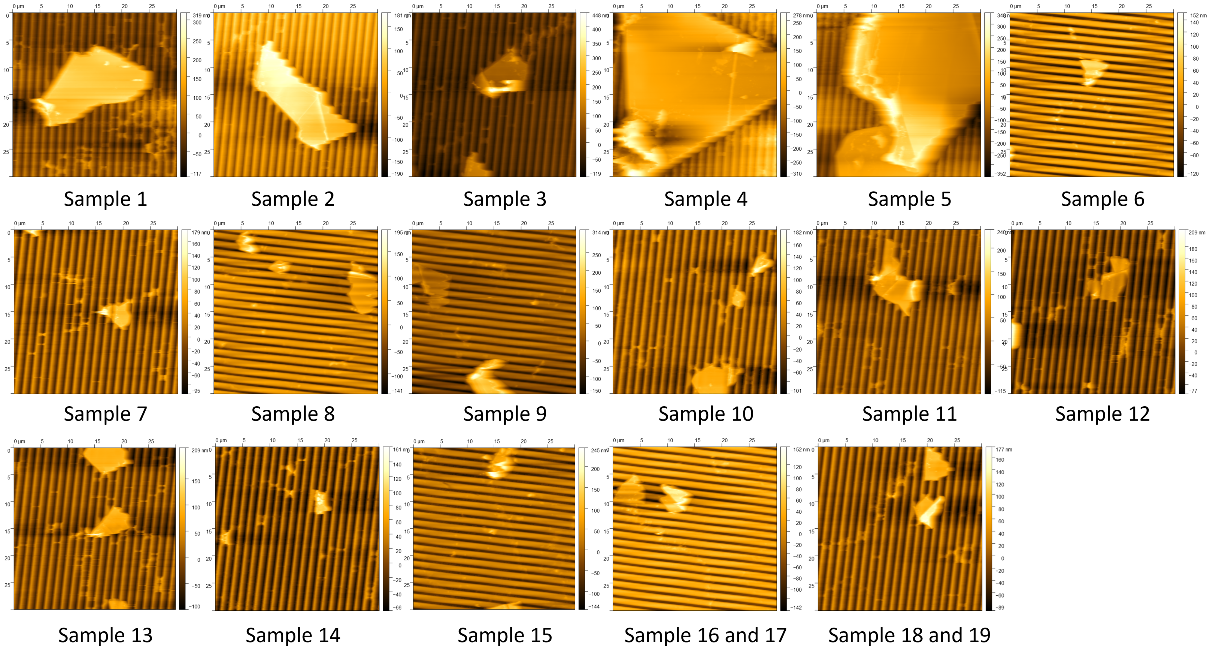
Sample 1
Sample 2
Sample 3
Sample 4
Sample 5
Sample 6
Sample 7
Sample 8
Sample 9
Sample 10
Sample 11
Sample 12
Sample 13
Sample 14
Sample 15
Sample 16 and 17
Sample 18 and 19

Figure 72: AFM topography of samples 1 to 19.

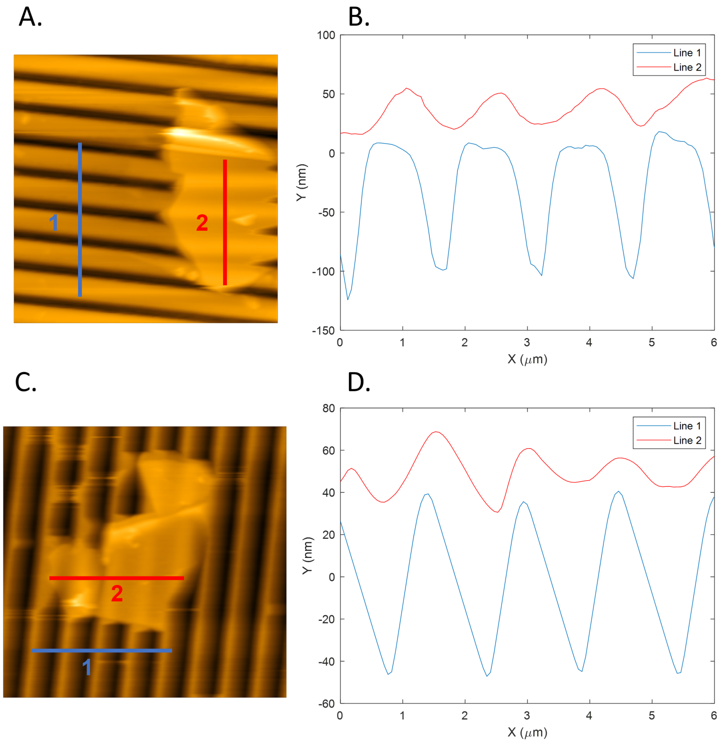

Figure 73: Influence of the CD micro/nano-structures on the hBN flakes. **A.** Lines where the profile has been examined in sample 8. **B.** Profiles of line 1 (CD) and line 2 (CD+hBN) of sample 8. **C.** Lines where the profile has been examined in sample 12. **D.** Profiles of line 1 (CD) and line 2 (CD+hBN) of sample 12.

The size and thickness of all these 19 flakes are summarised in Figure 72. In Figure 73, we can see the influence of the CD micro/nanostructures on some of the influenced samples. By plotting the correlation of these properties and whether the flakes are influenced by the CD structure, it can be concluded that small thin flakes of a maximum surface of $\sim 52.7\ \mu m^2$ and a maximum thickness of $\sim 95\ nm$ can conform to the CD structures. This correlation can be seen in Figure 74.

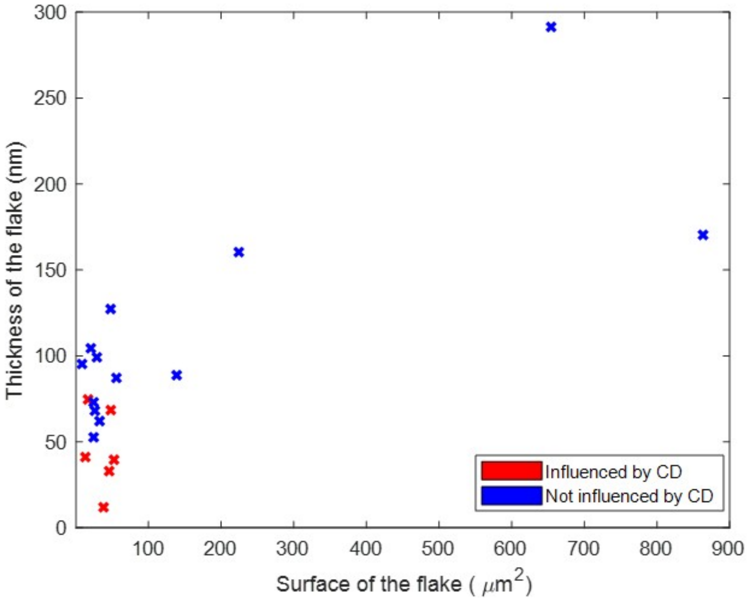

Figure 74: Correlation between influence of the CD structures and thickness of the flake and its size.

5.3.3 Photoluminescence and Raman spectroscopy

The PL test shows that there is no increase of intensity when we approach the region where the hBN flake is influenced by the CD micro/nano-structure Figure 75. Additionally, when performing a Raman line map no Raman shift is present, indicating that the hBN flake is not strained. In the case of the Blu-ray disk, the background emission of the Blu-ray disk has values between 7000 and 13000, while the hBN flake shows at all measured points a peak that is only a 5.7 % more intense compared to the background emission. This high emission from the background compared to the hBN makes difficult to establish a cause-and-effect relationship between the observed intensity change and the presence of quantum emitters. Even if in a future we should choose substrates that do not emit fluorescence at the used wavelengths, the aspect ratio of the surface protuberances of the Blu-ray disk are probably not sufficient to produce the threshold strain.

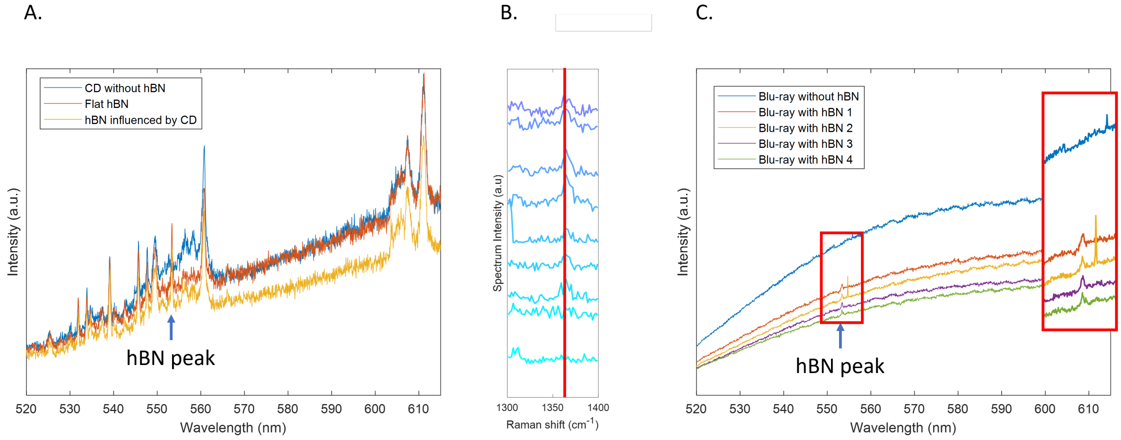

Figure 75: **A.** PL of the bare CD (blue), flat hBN mechanically exfoliated onto the CD (red) and the hBN flake conformed onto the CD (yellow). **B.** Raman line map of a hBN flake conformed into the CD. The red line helps to visualise that no Raman shift is present. **C.** PL of bare Blu-ray disk (blue) and four different points of an hBN flake mechanically exfoliated onto the Blu-ray disk (red, yellow, purple and green).

5.3.4 Summary

Overall, we have observed that CDs and Blu-ray disks present the most periodic arrays compared to the rest of structures used in this project. Even if the hBN flakes conform onto these structures, specially thin and small flakes in the case of CDs, we have checked with PL and Raman spectroscopy that these structures have not been able to strain the hBN flakes and therefore produce quantum emitters.

6 Conclusions and Outlook

6.1 Conclusions

This master's thesis explores the potential of strain-induced quantum emitters in pristine hBN. To achieve this, we systematically generated strain by stamping pristine flakes onto various rigid micro/nano-structures with different aspect ratios. Specifically these structures are $5\mu m$ and $10\mu m$ polystyrene beads, femtosecond laser ablated cavities and CD and Blu-ray structures. The polystyrene beads appeared to emit fluorescence with and without hBN flakes stamped onto them. Interestingly, a bead+hBN sample emitted a higher intensity fluorescence than the surrounding beads without hBN. When we performed PL and Raman spectroscopy tests, we were not certain which component emitted the fluorescence and could not detect strain in the hBN flake. However, if the hBN flake would have been clamped, the hBN flake could have reached strains up to ~ 4.5 % according to FEM. Posterior fluorescence microscopy measurements suggested that a chemical interaction between the hBN flake and the bead may have occurred.

In the case of hBN flakes exfoliated in CDs and Blu-ray structures, we found that in general, thin and small flakes conform onto these structures. However, the PL and Raman spectroscopy results suggested that the aspect ratio of both structures may not be enough in order to generate strain. Additionally, we observed that silver substrates should be avoided in future studies since the hBN emission is only a 5.7 % higher than the substrate, challenging the interpretation of the results.

We could observe fluorescence emission in 2/3 of the samples where the hBN is conformed onto SiO_2/Si cavities. The position of these fluorescent spots coincide with the location of peaks at the rim of the cavity, meaning that these may be caused by the recast layer generated with the ablation. However, no specific threshold values for curvature, substrate structure height, and hBN thickness leading to reproducible localized fluorescence were identified. The Raman results performed with green light, revealed the existence of strain in a fluorescent region, even if it did not show intense emission during PL. With a dynamic fluorescence study, we could check that if QEs were excited with green light, these tend to become latent. However, with red and blue light we observed photoblinking and photobleaching phenomena respectively. We were able to quantify an intensity reduction of 38 % and fluorescence lifetimes between 6.57 and 44.17 seconds.

From the four initial research questions, we have been able to answer two of the questions: 1. Can quantum emitters be created with strain engineering? and 2. How does the dimensions and shape of the micro/nanostructures influence the formation of quantum emitters? Overall, in this thesis we have shown that quantum emitters can be induced with strain engineering. Moreover we have shown that from all the structures, only the ones with an aspect ratio (width/height) between 6.7 to 11 have been able to generate quantum emitters, while the ones with an aspect ratio of 1 (beads), 13.5-18 (CDs) and 40 (Bu-ray disks) were unable. These numbers give a first indicative value of which may be the optimum aspect ratio to generate strain-induced quantum emitters in pristine. Even if we have not been able to see a conclusive correlation between curvature and generation of quantum emitters, curvature may be a more important value than aspect ratio. This statement needs to be proven with further studies. However, a first indicative value of which may be the optimum curvature is around $\sim 4.45x10^5$.

In conclusion, these findings present valuable insights and serve as baseline for further research in utilizing strain engineering to generate quantum emitters in hBN. Through further work, it is thought that the mechanisms to generate strain-induced quantum emitters can be understood and used for future protein sequencing applications.

6.2 Future work

These findings open up further research opportunities for the use of strain engineering to generate quantum emitters in pristine. However, some challenges that have been faced during this thesis could be solved in a future, such as determining which structure and flake properties are the cause of strain, how the material of the substrate influence the properties of QEs or quantifying the amount of strain precisely.

To achieve these objectives, further experiments could involve:

- A parametric study in which different factors such as thickness of the flake, curvature of the substrate, height or stamping force are evaluated systematically and see their effect in strain generation.
- Measure experimentally with Raman spectroscopy the correlation between strain and Raman shift of hBN at 514 nm. This could be done with a MEMS device that can control accurately the strain applied on the hBN flake.
- Once the generation of strain and QEs is understood, the effect of different material substrates in hBN QEs can be quantified with PL studies and fluorescence microscopy.

Appendices

A Estimation of curvatures with Lorentzian fitting

The Lorentzian curvature of the different structures used in thesis is done as it follows: First we open with Gwyddion one AFM result and draw two perpendicular lines at the location of interest (Figure 76 A). Next, we analyse the height profiles of these lines and choose to keep the one that has the sharpest peak (in the case of Figure 76 B we keep the black line). Finally with the help of Gwyddion we fit the curve of our peak to the equation that reproduces the best our curve, in our case is the Lorentzian equation (Figure 76 C). The necessary parameters of the equation together with their errors will appear on the screen of the software once the curve is fit to the equation.

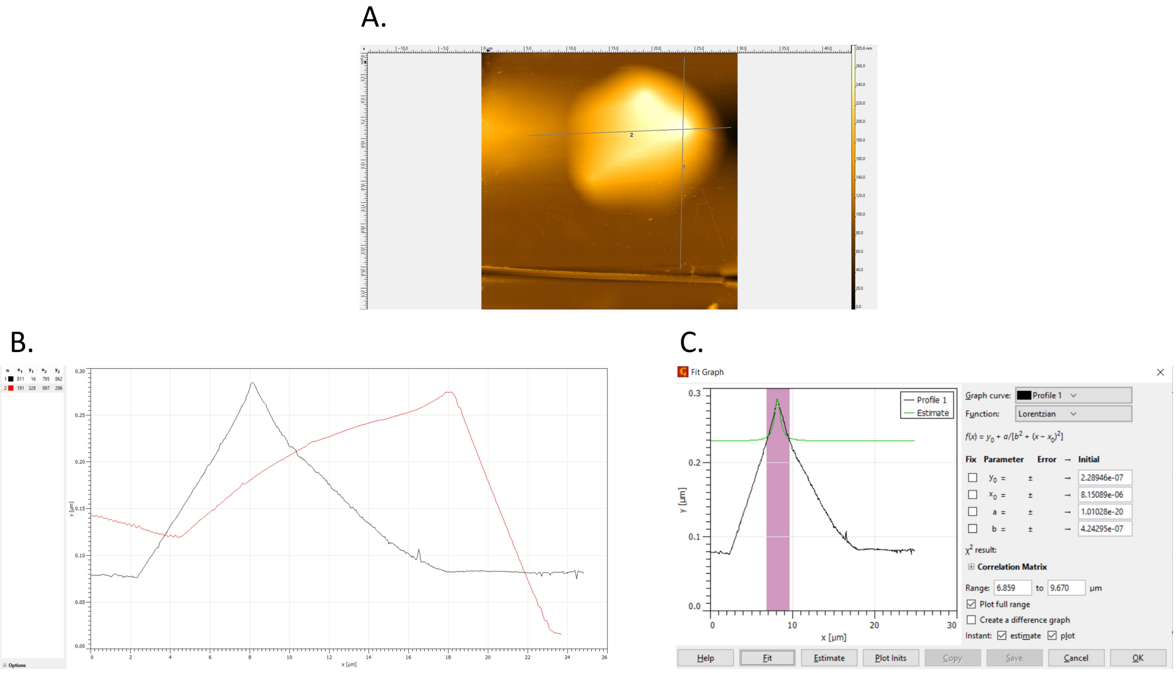

Graph curve: Profile 1

Function: Lorentzian

$f(x) = y_0 + a/[b^2 + (x - x_0)^2]$

Fix	Parameter	Error	→	Initial
☐	y_0 =	±	→	2.28946e-07
☐	x_0 =	±	→	8.15089e-06
☐	a =	±	→	1.01028e-20
☐	b =	±	→	4.24295e-07

χ^2 result:

⊞ Correlation Matrix

Range: 6.859 to 9.670 μm

☑ Plot full range

☐ Create a difference graph

Instant: ☑ estimate ☑ plot

Figure 76: Estimation of the curvature of a peak found in a hBN bubble. **A.** First two perpendicular line are created with Gwyddion at the peak. **B.** The height profiles of both lines are represented, and the one that presents the sharpest peak is analysed. **C.** With the help of Gwyddion the curve of the peak is approximated to a Lorentzian curve.

With the obtainment of these parameters and their errors we can estimate the value of the curvature of the location of interest. The Lorentzian equation has the following expression:

$$f(x) = y_0 + \frac{a}{b^2 + (x - x_0)^2} \tag{3}$$

The curvature can be estimated with the following equation:

$$\kappa = \frac{|y''|}{(1 + (y')^2)^{\frac{2}{3}}} \tag{4}$$

The curvature (κ) is evaluated at the maximum the slope is zero, therefore $y' = 0$. The equation of the curvature can be reduced to:

$$\kappa = |y''| = \frac{-2a(b^2 - 3(x - x_0)^2)}{b^2 + (x - x_0)^2)^3} \tag{5}$$

Since the curvature is evaluated at $x = x_0$, the equation can be simplified as:

$$\kappa = \frac{-2a(b^2)}{(b^2)^3} = \frac{-2a}{b^4} \tag{6}$$

The uncertainty of the estimated curvature can be expressed as it follows, being s_a and s_b the errors of parameters a and b:

$$s_\kappa = \sqrt{(\frac{\partial \kappa}{\partial a})^2 s_a^2 + (\frac{\partial \kappa}{\partial b})^2 s_b^2} = \sqrt{(\frac{-2}{b^4})^2 s_a^2 + (\frac{8a}{b^5})^2 s_b^2} \tag{7}$$

B FEM Simulation

We used FEM in order to estimate the strain of the hBN flake when interacts with a $10\mu m$ bead. For it a first model was created, where a block of 10 μm was displaced 1 μm onto the hBN. The strain generated on the hBN with this model is 0.257% (Figure 77). If the displacement of the block was increased to 10 μm, the hBN would break.

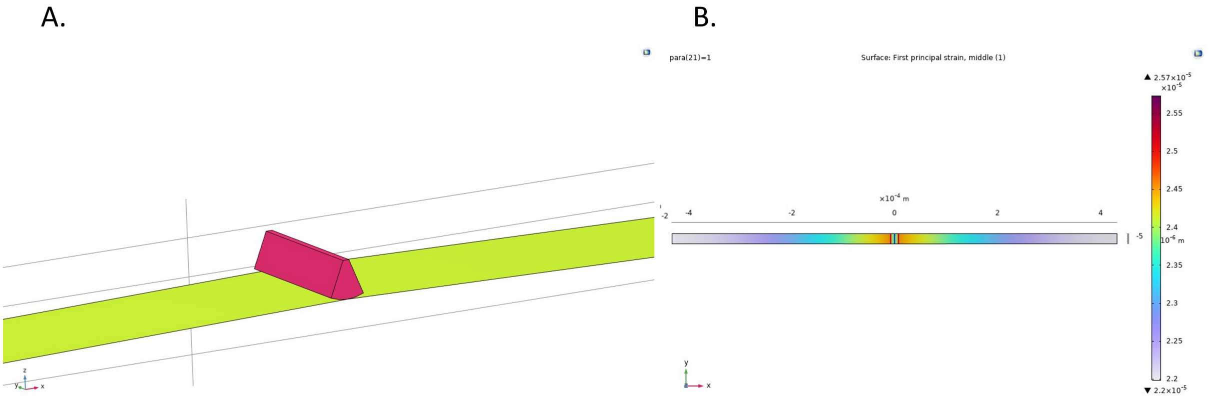

Figure 77: A. First model used to estimate the strain generated on the hBN flake when interacting with a 10 *mum* block. B. Strain distribution on the hBN flake when the block is displaced 1 μm onto the hBN flake. The maximum amount of strain (0.257 %) is found where the displacement is applied.

For this reason, a more simple second model was created. This 2D simulation consist of a circle with fixed edge that represents the hBN flake Figure 78. A point displacement of 10 μm is applied at the center of the circle. With this second model, the maximum strain has a value of 4.5 %.

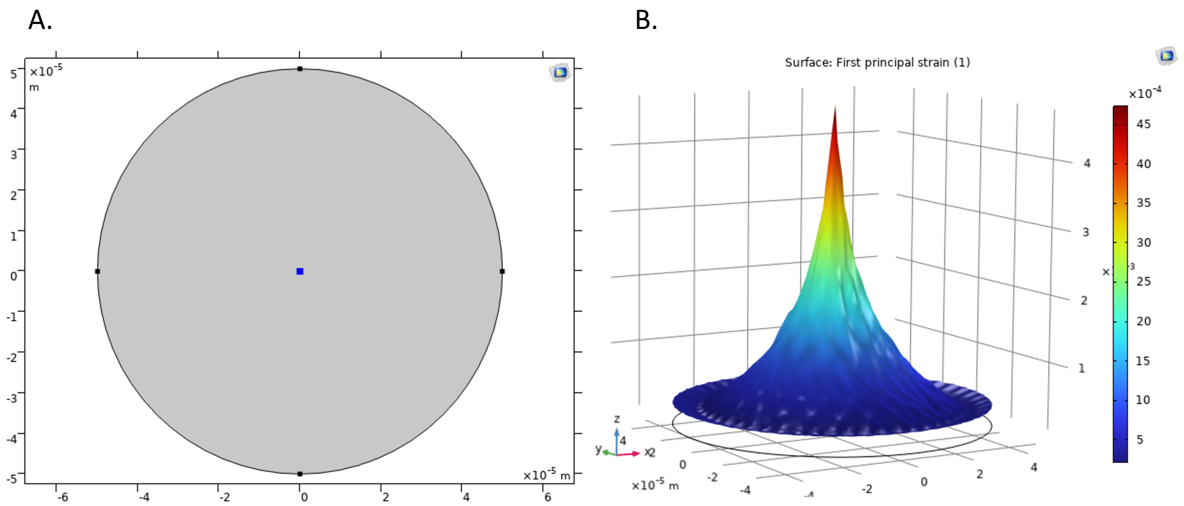

Figure 78: **A.** Second model used to estimate the strain generated on the hBN flake when interacting with a 10 mum point displacement. **B.** Strain distribution on the hBN flake when a displacement of 10 μm interacts with the hBN flake. The maximum amount of strain (4.5 %) is found where the displacement is applied.

The properties used for the simulation of hBN are the following:

Structure	**Thickness (nm)**	**Young's modulus (GPa)**	**Tensile strength (GPa)**	**Poisson ratio**
Planar hexagonal	0.42	665	21	0.2176

Table 5: Summary of the mechanical properties of hBN [91].

References

[1] Noelia Ferruz and Birte Höcker. "Dreaming ideal protein structures". In: *Nat Biotechnol* 40 (2022), pp. 171–172. DOI: 10.1038/s41587-021-01196-9. URL: https://doi.org/10.1038/s41587-021-01196-9.

[2] *Medical Biochemistry*. Tech. rep. 2017.

[3] Jerker Widengren et al. "Single-molecule detection and identification of multiple species by multiparameter fluorescence detection". In: *Analytical Chemistry* 78.6 (Mar. 2006), pp. 2039–2050. ISSN: 00032700. DOI: 10.1021/ac0522759.

[4] Penghao Wang and Susan R. Wilson. "Mass spectrometry-based protein identification by integrating de novo sequencing with database searching". In: *BMC Bioinformatics* 14.Suppl 2 (2013), S24. ISSN: 14712105. DOI: 10.1186/1471-2105-14-S2-S24. URL: /pmc/articles/PMC3549845/%20/pmc/articles/PMC3549845/?report=abstract%20https://www.ncbi.nlm.nih.gov/pmc/articles/PMC3549845/.

[5] Khalid Z. Masoodi, Sameena Maqbool Lone, and Rovidha Saba Rasool. "Dansyl-Edman method of peptide sequencing". In: *Advanced Methods in Molecular Biology and Biotechnology* (Jan. 2021), pp. 89–92. DOI: 10.1016/B978-0-12-824449-4.00016-5.

[6] Meni Wanunu. "Back and forth with nanopore peptide sequencing". In: *Nature Biotechnology* 40.2 (Feb. 2022), pp. 172–173. ISSN: 1087-0156. DOI: 10.1038/s41587-021-01205-x.

[7] Zheng-Li Hu et al. "NanoporeE lectrochemistry Biological Nanopore Approach for Single-Molecule Protein Sequencing". In: *Epub* 60.27 (2021), pp. 14738–14749. DOI: 10.1002/anie.202013462. URL: https://doi.org/10.1002/anie.202013462..

[8] Mazdak Afshar Bakshloo et al. "Nanopore-Based Protein Identification". In: *Cite This: J. Am. Chem. Soc* 2022 (2716). DOI: 10.1021/jacs.1c11758. URL: https://doi.org/10.1021/jacs.1c11758.

[9] Pierre Bon and Laurent Cognet. *On Some Current Challenges in High-Resolution Optical Bioimaging*. Aug. 2022. DOI: 10.1021/acsphotonics.2c00606.

[10] Takahito Ohshiro and Masateru Taniguchi. *Review of the use of nanodevices to detect single molecules*. Oct. 2022. DOI: 10.1016/j.ab.2022.114645.

[11] Yao Yao et al. "Single-molecule protein sequencing through fingerprinting: Computational assessment". In: *Physical Biology* 12.5 (Aug. 2015). ISSN: 14783975. DOI: 10.1088/1478-3975/12/5/055003.

[12] Michael Kandziolka et al. "Silicon nanopillars as a platform for enhanced fluorescence analysis". In: *Analytical Chemistry* 85.19 (Oct. 2013), pp. 9031–9038. ISSN: 00032700. DOI: 10.1021/ac401500y.

[13] Lydia Skolrood et al. "Single-molecule and particle detection on true portable microscopy platforms". In: *Sensors and Actuators Reports* 4 (Nov. 2022). ISSN: 26660539. DOI: 10.1016/j.snr.2021.100063.

[14] Amrita Kaur, Pardeep Kaur, and Sahil Ahuja. "Förster resonance energy transfer (FRET) and applications thereof (Anal. Methods (2020) 12 (55325550) DOI: 10.1039/D0AY01961E)". In: *Analytical Methods* 13.5 (Feb. 2021), p. 730. ISSN: 17599679. DOI: 10.1039/D1AY90011K.

[15] Dong Hoon Shin, Xiliang Yang, and Sabina Caneva. "Single-Molecule Protein Fingerprinting with Photonic Hexagonal Boron Nitride Nanopores". In: *Accounts of Materials Research* 2023 (Apr. 2023), p. 310. ISSN: 2643-6728. DOI: 10.1021/ACCOUNTSMR.3C00016. URL: https://pubs.acs.org/doi/full/10.1021/accountsmr.3c00016.

[16] Richard Nelz et al. "Near-Field Energy Transfer between a Luminescent 2D Material and Color Centers in Diamond". In: *Advanced Quantum Technologies* 3.2 (Feb. 2020). ISSN: 25119044. DOI: 10.1002/qute.201900088.

[17] Mahsa Imani et al. *Recent advances in FRET-Based biosensors for biomedical applications*. Oct. 2021. DOI: 10.1016/j.ab.2021.114323.

[18] Feng Tian et al. *Graphene and graphene-like two-denominational materials based fluorescence resonance energy transfer (FRET) assays for biological applications*. Mar. 2017. DOI: 10.1016/j.bios.2016.06.046.

[19] Jie Zhou et al. *Two-dimensional nanomaterials for Förster resonance energy transfer-based sensing applications.* July 2020. DOI: 10.1515/nanoph-2020-0065.

[20] Gopal Ramalingam et al. “Quantum Confinement Effect of 2D Nanomaterials”. In: *Quantum Dots - Fundamental and Applications.* IntechOpen, June 2020. DOI: 10.5772/intechopen.90140.

[21] Wenjing Jie et al. “Review 1701296 (1 of 35)”. In: (2018). DOI: 10.1002/adom.201701296. URL: https://doi.org/10.1002/adom.201701296..

[22] Chase A. Munson et al. “Laser-based detection methods of explosives”. In: *Counterterrorist Detection Techniques of Explosives* (2007), pp. 279–321. DOI: 10.1016/B978-044452204-7/50029-8.

[23] Amber H M Vervloet. *Fabricating quantum emitters in hexagonal boron nitride for protein fingerprinting.* Tech. rep. 2022.

[24] A Hughes and A E Hughes. “ZERO-PHONON TRANSITIONS AND VIBRATIONAL STRUCTURE”. In: *Journal de Physique Colloques* 28.C4 (1967). DOI: 10.1051/jphyscol:1967408{\"{i}}. URL: https://hal.archives-ouvertes.fr/jpa-00213295.

[25] C. Hidrovo and D. Hart. “DUAL EMISSION LASER INDUCED FLUORESCENCE TECHNIQUE (DELIF) FOR OIL FILM THICKNESS AND TEMPERATURE MEASUREMENT”. In: (2000).

[26] *FranckCondon principle - Wikipedia.* URL: https://en.wikipedia.org/wiki/Franck%E2%80%93Condon_principle.

[27] Pedro Navarro Pérez. “Stable single molecules for quantum optics and all-optical switches Issue”. In: (2014). URL: http://hdl.handle.net/1887/29975.

[28] J Miguel Sanches and Isabel Rodrigues. “Photobleaching/Photoblinking Differential Equation Model for Fluorescence Microscopy Imaging”. In: (1927). DOI: 10.1017/S143192761300189X. URL: https://doi.org/10.1017/S143192761300189X.

[29] J Shepard et al. “Diffraction-Limited Molecular Cluster Quantification with Bayesian Nonparametrics”. In: (2021). DOI: 10.1101/2020.09.28.317057. URL: https://doi.org/10.1101/2020.09.28.317057.

[30] Rajesh Babu Sekar and Ammasi Periasamy. *Fluorescence resonance energy transfer (FRET) microscopy imaging of live cell protein localizations.* 2003. DOI: 10.1083/jcb.200210140.

[31] Georg Urstöger et al. “Evaluating the degree of molecular contact between cellulose fiber surfaces using FRET microscopy”. In: *Cellulose* 26.12 (Aug. 2019), pp. 7037–7050. ISSN: 1572882X. DOI: 10.1007/s10570-019-02575-x.

[32] Aileen M Eagleton. *Genetically Engineered Peptides for Light Harvesting and Folding Genetically Engineered Peptides for Light Harvesting and Folding Kinetics Studies Kinetics Studies.* Tech. rep. 2018. URL: https://scholarsarchive.library.albany.edu/honorscollege_chem.

[33] Stefan Kück. “Single photon sources for absolute radiometry A review about the current state of the art”. In: *Measurement: Sensors.* Vol. 18. Elsevier Ltd, Dec. 2021. DOI: 10.1016/j.measen.2021.100219.

[34] Robert Yan et al. “The cold denaturation of IscU highlights structurefunction dualism in marginally stable proteins”. In: *Communications Chemistry* 1.1 (Dec. 2018). ISSN: 23993669. DOI: 10.1038/s42004-018-0015-1.

[35] Masihuz Zaman et al. *Nanoparticles in relation to peptide and protein aggregation.* Feb. 2014. DOI: 10.2147/IJN.S54171.

[36] Evan Meyer-Scott, Christine Silberhorn, and Alan Migdall. “Single-photon sources: Approaching the ideal through multiplexing”. In: *Review of Scientific Instruments* 91.4 (Apr. 2020), p. 041101. ISSN: 0034-6748. DOI: 10.1063/5.0003320.

[37] Shaimaa I. Azzam, Kamyar Parto, and Galan Moody. “Prospects and challenges of quantum emitters in 2D materials”. In: *Applied Physics Letters* 118.24 (June 2021). ISSN: 00036951. DOI: 10.1063/5.0054116.

[38] F. Wang and X. Liu. “Rare-Earth Doped Upconversion Nanophosphors”. In: *Comprehensive Nanoscience and Nanotechnology* 1-5 (Jan. 2011), pp. 359–384. DOI: 10.1016/B978-0-12-812295-2.00146-X.

[39] Steffen Michaelis de Vasconcellos et al. *Single-Photon Emitters in Layered Van der Waals Materials*. Apr. 2022. DOI: 10.1002/pssb.202100566.

[40] Mônica A. Cotta. *Quantum Dots and Their Applications: What Lies Ahead?* June 2020. DOI: 10.1021/acsanm.0c01386.

[41] Nhi Le, Min Zhang, and Kyoungtae Kim. *Quantum Dots and Their Interaction with Biological Systems*. Sept. 2022. DOI: 10.3390/ijms231810763.

[42] Igor Aharonovich, Dirk Englund, and Milos Toth. *Solid-state single-photon emitters*. Oct. 2016. DOI: 10.1038/nphoton.2016.186.

[43] A. Sajid, Michael J. Ford, and Jeffrey R. Reimers. *Single-photon emitters in hexagonal boron nitride: a review of progress*. Apr. 2020. DOI: 10.1088/1361-6633/ab6310.

[44] Rani Rahat et al. "Graphene quantum dots: application in biomedical science". In: *Graphene Quantum Dots: Biomedical and Environmental Sustainability Applications* (Jan. 2023), pp. 101–111. DOI: 10.1016/B978-0-323-85721-5.00002-9.

[45] Elaine Lay Khim Chng and Martin Pumera. "Toxicity of graphene related materials and transition metal dichalcogenides". In: *RSC Advances* 5.4 (Dec. 2014), pp. 3074–3080. ISSN: 2046-2069. DOI: 10.1039/C4RA12624F. URL: https://pubs.rsc.org/en/content/articlehtml/2015/ra/c4ra12624f%20https://pubs.rsc.org/en/content/articlelanding/2015/ra/c4ra12624f.

[46] Xiaolong Liu and Mark C. Hersam. *2D materials for quantum information science*. Oct. 2019. DOI: 10.1038/s41578-019-0136-x.

[47] Wei Liu et al. "An ultrastable and robust single-photon emitter in hexagonal boron nitride". In: *Physica E: Low-Dimensional Systems and Nanostructures* 124 (Oct. 2020). ISSN: 13869477. DOI: 10.1016/j.physe.2020.114251.

[48] Ute Resch-Genger et al. *Quantum dots versus organic dyes as fluorescent labels*. 2008. DOI: 10.1038/nmeth.1248.

[49] Jeewan C. Ranasinghe et al. "Engineered 2D materials for optical bioimaging and path toward therapy and tissue engineering". In: *Journal of Materials Research* 37.10 (May 2022), pp. 1689–1713. ISSN: 20445326. DOI: 10.1557/s43578-022-00591-5.

[50] Chitraleema Chakraborty, Nick Vamivakas, and Dirk Englund. *Advances in quantum light emission from 2D materials*. 2019. DOI: 10.1515/nanoph-2019-0140.

[51] Bernd Sontheimer et al. "Direct measurement of quantum efficiency of single-photon emitters in hexagonal boron nitride". In: *Optica, Vol. 6, Issue 8, pp. 1084-1088* 6.8 (Aug. 2019), pp. 1084–1088. ISSN: 2334-2536. DOI: 10.1364/OPTICA.6.001084. URL: https://opg.optica.org/viewmedia.cfm?uri=optica-6-8-1084&seq=0&html=true%20https://opg.optica.org/abstract.cfm?uri=optica-6-8-1084%20https://opg.optica.org/optica/abstract.cfm?uri=optica-6-8-1084.

[52] Madhura Ghosh Dastidar et al. *Quantum emitters and detectors based on 2D van der Waals materials*. Mar. 2022. DOI: 10.1039/d1nr08193d.

[53] Hélène Ollivier et al. "Reproducibility of High-Performance Quantum Dot Single-Photon Sources". In: *ACS Photonics* 7.4 (Apr. 2020), pp. 1050–1059. ISSN: 23304022. DOI: 10.1021/ACSPHOTONICS.9B01805. URL: https://pubs.acs.org/doi/abs/10.1021/acsphotonics.9b01805.

[54] Adam Bolotsky et al. "Two-Dimensional Materials in Biosensing and Healthcare: From in Vitro Diagnostics to Optogenetics and beyond". In: *ACS Nano* 13.9 (May 2019), pp. 9781–9810. ISSN: 1936086X. DOI: 10.1021/acsnano.9b03632.

[55] Pratik V. Shinde and Manoj Kumar Singh. "Synthesis, characterization, and properties of graphene analogs of 2D material". In: *Fundamentals and Sensing Applications of 2D Materials*. Elsevier, Jan. 2019, pp. 91–143. ISBN: 9780081025772. DOI: 10.1016/B978-0-08-102577-2.00004-X.

[56] A. Sajid, Michael J. Ford, and Jeffrey R. Reimers. *Single-photon emitters in hexagonal boron nitride: a review of progress*. Apr. 2020. DOI: 10.1088/1361-6633/ab6310.

[57] Katja Beha et al. "Diamond nanophotonics". In: *Beilstein Journal of Nanotechnology* 3.1 (2012), pp. 895–908. ISSN: 21904286. DOI: 10.3762/bjnano.3.100.

[58] Anton I. Zeleneev et al. "On studying the optical properties of NV/SiV color centers in ultrasmall nanodiamonds". In: *AIP Conference Proceedings*. Vol. 2241. American Institute of Physics Inc., June 2020. ISBN: 9780735420007. DOI: 10.1063/5.0012326.

[59] Tianchao Niu and Ang Li. *From two-dimensional materials to heterostructures.* 2015. DOI: 10.1016/j.progsurf.2014.11.001.

[60] Jingang Wang, Fengcai Ma, and Mengtao Sun. *Graphene, hexagonal boron nitride, and their heterostructures: properties and applications.* 2017. DOI: 10.1039/c7ra00260b.

[61] Hyo Ju Park, Gyeong Hee Ryu, and Zonghoon Lee. "Hole Defects on Two-Dimensional Materials Formed by Electron Beam Irradiation: Toward Nanopore Devices". In: *Applied Microscopy* 45.3 (Sept. 2015), pp. 107–114. ISSN: 2287-5123. DOI: 10.9729/am.2015.45.3.107.

[62] A. Maity et al. *Hexagonal boron nitride: Epitaxial growth and device applications.* Mar. 2021. DOI: 10.1016/j.pquantelec.2020.100302.

[63] Xinzhe Xiao et al. *Photoluminescence and Fluorescence Quenching of Graphene Oxide: A Review.* July 2022. DOI: 10.3390/nano12142444.

[64] Elsa M. Materon et al. "Electrochemical sensors based on metal oxide-boron nitride nanocomposites in the detection of biomolecules and toxic chemicals". In: *Metal Oxides in Nanocomposite-Based Electrochemical Sensors for Toxic Chemicals.* Elsevier, Jan. 2021, pp. 293–311. ISBN: 9780128207277. DOI: 10.1016/B978-0-12-820727-7.00004-5.

[65] Yijing Huang et al. "Engineering of single-photon emitters in hexagonal boron nitride [Invited]". In: *Chinese Optics Letters* 20.3 (2022), p. 032701. ISSN: 1671-7694. DOI: 10.3788/col202220.032701.

[66] Joshua Ziegler et al. "Deterministic Quantum Emitter Formation in Hexagonal Boron Nitride via Controlled Edge Creation". In: *Nano Letters* 19.3 (Mar. 2019), pp. 2121–2127. ISSN: 15306992. DOI: 10.1021/acs.nanolett.9b00357.

[67] Mehdi Abdi et al. "Color Centers in Hexagonal Boron Nitride Monolayers: A Group Theory and Ab Initio Analysis". In: *ACS Photonics* 5.5 (2018). ISSN: 23304022. DOI: 10.1021/acsphotonics.7b01442.

[68] Wenchao Tian et al. *A review on lattice defects in graphene: Types generation effects and regulation.* 2017. DOI: 10.3390/mi8050163.

[69] Jie Jiang et al. "Defect engineering of two-dimensional materials towards next-generation electronics and optoelectronics". In: *Nano Research* (Nov. 2022). ISSN: 1998-0124. DOI: 10.1007/s12274-022-5016-9. URL: https://link.springer.com/10.1007/s12274-022-5016-9.

[70] Clarisse Fournier et al. "Position-controlled quantum emitters with reproducible emission wavelength in hexagonal boron nitride". In: *Nature Communications* 12.1 (Dec. 2021). ISSN: 20411723. DOI: 10.1038/s41467-021-24019-6.

[71] Sumin Choi et al. "Engineering and Localization of Quantum Emitters in Large Hexagonal Boron Nitride Layers". In: *ACS Applied Materials and Interfaces* 8.43 (Nov. 2016), pp. 29642–29648. ISSN: 19448252. DOI: 10.1021/acsami.6b09875.

[72] Marika Schleberger and Jani Kotakoski. "2D material science: Defect engineering by particle irradiation". In: *Materials* 11.10 (Oct. 2018). ISSN: 19961944. DOI: 10.3390/ma11101885.

[73] Andres Vasquez et al. "Micro-structuring, ablation, and defect generation in graphene with femtosecond pulses". In: *OSA Continuum* 2.10 (Oct. 2019), p. 2925. ISSN: 25787519. DOI: 10.1364/osac.2.002925.

[74] Joel M. Solomon et al. "Ultrafast multi-shot ablation and defect generation in monolayer transition metal dichalcogenides". In: *AIP Advances* 12.1 (Jan. 2022). ISSN: 21583226. DOI: 10.1063/5.0078054.

[75] Akbar Basha Dhu al jalali wal ikram Shaik and Penchalaiah Palla. "Optical quantum technologies with hexagonal boron nitride single photon sources". In: *Scientific Reports* 11.1 (Dec. 2021). ISSN: 20452322. DOI: 10.1038/s41598-021-90804-4.

[76] Zai Quan Xu et al. "Single photon emission from plasma treated 2D hexagonal boron nitride". In: *Nanoscale* 10.17 (May 2018), pp. 7957–7965. ISSN: 20403372. DOI: 10.1039/c7nr08222c.

[77] Rachael Klaiss et al. "Uncovering the morphological effects of high-energy Ga+focused ion beam milling on hBN single-photon emitter fabrication". In: *Journal of Chemical Physics* 157.7 (Aug. 2022). ISSN: 10897690. DOI: 10.1063/5.0097581.

[78] Yougui Liao. *Advantages and disadvantages of FIB technology for EM sample preparations.* URL: https://www.globalsino.com/EM/page4503.html.

[79] Xiaohui Xu et al. *Creating Quantum Emitters in Hexagonal Boron Nitride Deterministically on Chip-Compatible Substrates*. Tech. rep. 2021, pp. 8182–8189.

[80] Noah Mendelson et al. “Strain-Induced Modification of the Optical Characteristics of Quantum Emitters in Hexagonal Boron Nitride”. In: *Advanced Materials* 32.21 (May 2020). ISSN: 15214095. DOI: 10.1002/adma.201908316.

[81] Pratibha Dev. “Fingerprinting quantum emitters in hexagonal boron nitride using strain”. In: *Physical Review Research* 2.2 (June 2020). ISSN: 26431564. DOI: 10.1103/PhysRevResearch.2.022050.

[82] Shengxue Yang, Yujia Chen, and Chengbao Jiang. “Strain engineering of two-dimensional materials: Methods, properties, and applications”. In: (2021). DOI: 10.1002/inf2.12177. URL: https://onlinelibrary.wiley.com/doi/10.1002/inf2.12177.

[83] Matthew R. Rosenberger et al. “Quantum Calligraphy: Writing Single-Photon Emitters in a Two-Dimensional Materials Platform”. In: *ACS Nano* 13.1 (Jan. 2019), pp. 904–912. ISSN: 1936086X. DOI: 10.1021/acsnano.8b08730.

[84] Chi Li et al. “Scalable and Deterministic Fabrication of Quantum Emitter Arrays from Hexagonal Boron Nitride”. In: *Nano Letters* 21.8 (2021). ISSN: 15306992. DOI: 10.1021/acs.nanolett.1c00685.

[85] Lintao Peng et al. “Creation of Single-Photon Emitters in WSe2Monolayers Using Nanometer-Sized Gold Tips”. In: *Nano Letters* 20.8 (Aug. 2020), pp. 5866–5872. ISSN: 15306992. DOI: 10.1021/acs.nanolett.0c01789.

[86] Nicholas V. Proscia et al. “Near-deterministic activation of room-temperature quantum emitters in hexagonal boron nitride”. In: *Optica* 5.9 (2018). ISSN: 23342536. DOI: 10.1364/optica.5.001128.

[87] Ben Tordoff et al. *The LaserFIB: new application opportunities combining a high-performance FIB-SEM with femtosecond laser processing in an integrated second chamber*. Dec. 2020. DOI: 10.1186/s42649-020-00044-5.

[88] Bijoy Bhattacharyya and Biswanath Doloi. “Machining processes utilizing mechanical energy”. In: *Modern Machining Technology*. Elsevier, 2020, pp. 21–160. DOI: 10.1016/b978-0-12-812894-7.00003-7.

[89] Péter Fürjes. “micromachines Controlled Focused Ion Beam Milling of Composite Solid State Nanopore Arrays for Molecule Sensing”. In: (2019). DOI: 10.3390/mi10110774. URL: www.mdpi.com/journal/micromachines.

[90] Mukesh Pandey et al. “Straining techniques for strain engineering of 2D materials towards flexible straintronic applications - ScienceDirect”. In: *Nano Energy* 109.108278 (2023). URL: https://www.sciencedirect.com/science/article/pii/S2211285523001143.

[91] Shikai Deng, Anirudha V. Sumant, and Vikas Berry. “Strain engineering in two-dimensional nanomaterials beyond graphene”. In: *Nano Today* 22 (Oct. 2018), pp. 14–35. ISSN: 1748-0132. DOI: 10.1016/J.NANTOD.2018.07.001.

[92] Zhiwei Li et al. “Efficient strain modulation of 2D materials via polymer encapsulation”. In: *Nature Communications 2020 11:1* 11.1 (Mar. 2020), pp. 1–8. ISSN: 2041-1723. DOI: 10.1038/s41467-020-15023-3. URL: https://www.nature.com/articles/s41467-020-15023-3.

[93] Toan Trong Tran et al. “Quantum emission from hexagonal boron nitride monolayers”. In: *Nature Nanotechnology* 11.1 (2016). ISSN: 17483395. DOI: 10.1038/nnano.2015.242.

[94] Weimiao Wang et al. “Interlayer and interfacial stress transfer in hBN nanosheets”. In: *2D Materials* 8 (Mar. 2021). DOI: 10.1088/2053-1583/ac0c2a. URL: https://doi.org/10.1088/2053-1583/ac0c2a.

[95] Xiangzhi Li et al. “Nonmagnetic Quantum Emitters in Boron Nitride with Ultranarrow and Sideband-Free Emission Spectra”. In: *ACS Nano* 11.7 (July 2017), pp. 6652–6660. ISSN: 1936086X. DOI: 10.1021/ACSNANO.7B00638. URL: https://pubs.acs.org/doi/full/10.1021/acsnano.7b00638.

[96] M. Koperski et al. “Towards practical applications of quantum emitters in boron nitride”. In: *Scientific Reports* 11.1 (Dec. 2021). ISSN: 20452322. DOI: 10.1038/s41598-021-93802-8.

[97] Sangyeon Cho et al. "Simple super-resolution live-cell imaging based on diffusion-assisted Förster resonance energy transfer". In: *Scientific Reports* 3.1 (Feb. 2013), p. 1208. ISSN: 2045-2322. DOI: `10.1038/srep01208`.

[98] Shambhulinga Aralekallu, Rajamouli Boddula, and Vijay Singh. "Development of glass-based microfluidic devices: A review on its fabrication and biologic applications". In: (2022). DOI: `10.1016/j.matdes.2022.111517`. URL: `https://doi.org/10.1016/j.matdes.2022.111517`.

[99] Koji Sugioka and Ya Cheng. *Femtosecond laser three-dimensional micro-and nanofabrication.* Dec. 2014. DOI: `10.1063/1.4904320`.

[100] Rafael R. Gattass and Eric Mazur. "Femtosecond laser micromachining in transparent materials". In: *Nature Publishing Group* 2 (2008), pp. 219–225.

[101] Min Wang et al. *Fabrication of high-Q microresonators in dielectric materials using a femtosecond laser: Principle and applications.* July 2017. DOI: `10.1016/j.optcom.2016.05.025`.

[102] Lukang Wang et al. "Design and fabrication of bulk micromachined 4h-sic piezoresistive pressure chips based on femtosecond laser technology". In: *Micromachines* 12.1 (2021). ISSN: 2072666X. DOI: `10.3390/mi12010056`.

[103] McGill University. *Compact Disc.* URL: `https://www.cs.mcgill.ca/~rwest/wikispeedia/wpcd/wp/c/Compact_Disc.htm`.

[104] Robert Sheldon and Brown Rodney. *What is optical storage and how does it work?* URL: `https://www.techtarget.com/searchstorage/definition/optical-storage`.

[105] Hongwei Liu et al. "Synthesis of hexagonal boron nitrides by chemical vapor deposition and their use as single photon emitters". In: *Nano Materials Science* 3.3 (Sept. 2021), pp. 291–312. ISSN: 25899651. DOI: `10.1016/j.nanoms.2021.03.002`.

[106] Fang Liu. "Mechanical exfoliation of large area 2D materials from vdW crystals". In: *Progress in Surface Science* 96.2 (May 2021). ISSN: 00796816. DOI: `10.1016/j.progsurf.2021.100626`.

[107] Zhengyang Cai et al. *Chemical Vapor Deposition Growth and Applications of Two-Dimensional Materials and Their Heterostructures.* July 2018. DOI: `10.1021/acs.chemrev.7b00536`.

[108] Augusto Di Gianfrancesco. "Technologies for chemical analyses, microstructural and inspection investigations". In: *Materials for Ultra-Supercritical and Advanced Ultra-Supercritical Power Plants.* Elsevier Inc., 2017, pp. 197–245. ISBN: 9780081005583. DOI: `10.1016/B978-0-08-100552-1.00008-7`.

[109] Gufeng Wang and Ning Fang. "Detecting and tracking nonfluorescent nanoparticle probes in live cells". In: *Methods in Enzymology.* Vol. 504. Academic Press Inc., 2012, pp. 83–108. DOI: `10.1016/B978-0-12-391857-4.00004-5`.

[110] Marleen Van Oosten et al. *Optical Imaging Applications in Cancer Research and Treatment.* Tech. rep. 2013. URL: `https://www.researchgate.net/publication/236595733`.

[111] Main Advisor prof henry markram and Edne Mentor. *in silico brain imaging physically-plausible methods for visualizaing neocortical microcircuitry marwan abdellah.* Tech. rep. 2017. URL: `www.marwan-abdellah.com`.

[112] Meisam Omidi et al. "Characterization of biomaterials". In: *Biomaterials for Oral and Dental Tissue Engineering.* Elsevier, Jan. 2017, pp. 97–115. ISBN: 9780081009611. DOI: `10.1016/B978-0-08-100961-1.00007-4`.

[113] G Binnig et al. *Atomic Force Microscope.* Tech. rep.

[114] Meisam Omidi et al. "Characterization of biomaterials". In: *Biomaterials for Oral and Dental Tissue Engineering* (Jan. 2017), pp. 97–115. DOI: `10.1016/B978-0-08-100961-1.00007-4`.

[115] Ilamaran Sivarajah. *Atomic Force Microscopy: General Principles and Applications.* URL: `https://www.azooptics.com/Article.aspx?ArticleID=2083`.

[116] University of Greifswald. *AFM (Atomic Force Microscope).* URL: `https://physik.uni-greifswald.de/en/research-groups/soft-matter-and-biophysics-prof-christiane-helm/methods/afm-atomic-force-microscope/`.

[117] T. S. Sampath Kumar. "Physical and Chemical Characterization of Biomaterials". In: *Characterization of Biomaterials* (Jan. 2013), pp. 11–47. DOI: `10.1016/B978-0-12-415800-9.00002-4`.

[118] Samir Kumar et al. "Surface-Enhanced Raman Scattering: Introduction and Applications". In: *Recent Advances in Nanophotonics - Fundamentals and Applications* (May 2020). DOI: 10.5772/INTECHOPEN.92614. URL: https://www.intechopen.com/chapters/72277%20undefined/chapters/72277.

[119] *4.3: Raman Spectroscopy - Chemistry LibreTexts*. URL: https://chem.libretexts.org/Bookshelves/Analytical_Chemistry/Physical_Methods_in_Chemistry_and_Nano_Science_(Barron)/04%3A_Chemical_Speciation/4.03%3A_Raman_Spectroscopy.

[120] Paola De Padova et al. "Low frequency Raman spectroscopy of few-atomic-layer thick hBN crystals". In: (2016). DOI: 10.1088/2053-1583/aa77d4. URL: https://doi.org/10.1088/2053-1583/aa77d4.

[121] Roman V. Gorbachev et al. "Hunting for Monolayer Boron Nitride: Optical and Raman Signatures". In: *Small* 7.4 (Feb. 2011), pp. 465–468. ISSN: 1613-6829. DOI: 10.1002/SMLL.201001628. URL: https://onlinelibrary.wiley.com/doi/full/10.1002/smll.201001628%20https://onlinelibrary.wiley.com/doi/abs/10.1002/smll.201001628%20https://onlinelibrary.wiley.com/doi/10.1002/smll.201001628.

[122] Lulu Ma, Wei Qiu, and Xuejun Fan. "Stress/strain characterization in electronic packaging by micro-Raman spectroscopy: A review". In: *Microelectronics Reliability* 118 (2021), p. 114045. DOI: 10.1016/j.microrel.2021.114045. URL: https://doi.org/10.1016/j.microrel.2021.114045.

[123] V Prabhakara et al. *Analysing the linearised radially polarised light source for improved precision in strain measurement using micro-Raman spectroscopy*. Tech. rep. 2020.

[124] Nanophoton. *Basic of Raman scattering*. URL: https://www.nanophoton.net/lecture-room/raman-spectroscopy/lesson-1-1.

[125] Elena Blundo et al. "Vibrational Properties in Highly Strained Hexagonal Boron Nitride Bubbles". In: *Nano Letters* 22.4 (Feb. 2022), pp. 1525–1533. ISSN: 15306992. DOI: 10.1021/ACS.NANOLETT.1C04197. URL: https://pubs.acs.org/doi/full/10.1021/acs.nanolett.1c04197.

[126] Marie Kremarová et al. "Extrinsic Effects on the Optical Properties of Surface Color Defects Generated in Hexagonal Boron Nitride Nanosheets". In: *ACS Applied Materials and Interfaces* 13.38 (Sept. 2021), pp. 46105–46116. ISSN: 19448252. DOI: 10.1021/ACSAMI.1C11060.

[127] Shengxue Yang, Yujia Chen, and Chengbao Jiang. "Strain engineering of two-dimensional materials: Methods, properties, and applications". In: *InfoMat* 3.4 (Apr. 2021), pp. 397–420. ISSN: 2567-3165. DOI: 10.1002/INF2.12177. URL: https://onlinelibrary.wiley.com/doi/full/10.1002/inf2.12177%20https://onlinelibrary.wiley.com/doi/abs/10.1002/inf2.12177%20https://onlinelibrary.wiley.com/doi/10.1002/inf2.12177.

[128] Lambert Instruments. *Fluorescence Lifetime Imaging Microscopy*. URL: https://www.lambertinstruments.com/technologies-1/2014/12/4/fluorescence-lifetime-imaging-microscopy.